Enhancing dust aerosols monitoring capabilities across North Africa and the Middle East using the A-Train satellite constellation

Anna Moustaka[1,2,3], Nikolaos Siomos[4], Stelios Kazadzis[2], Emmanouil Proestakis[3], Kalliopi Artemis Voudouri[3,1], Anton Lopatin[5~~4~~], Oleg Dubovik[6~~5~~], Kleareti Tourpali[1], Christos Zerefos[7~~6~~,8~~7~~,9~~8~~,10~~9~~], Vassilis Amiridis[3], and Antonis Gkikas[3,7,3~~6~~]

[1] Department of Physics, Aristotle University of Thessaloniki, 54124, Greece
[2] Physicalisch Meteorologisches Observatorium, World Radiation Center, Davos, 7260, Switzerland
[3] Institute for Astronomy, Astrophysics, Space Applications and Remote Sensing, National Observatory of Athens, Athens, 11810, Greece
[4] Meteorologisches Institut, Ludwig-Maximilians-Universität München, 80539, Germany
[5~~4~~] GRASP SAS, Lille, 59000, France
[6~~5~~] Laboratoire d'Optique Atmosphérique, CNRS/Université de Lille, Villeneuve-d'Ascq, 59650, France
[7~~6~~] Research Centre for Atmospheric Physics and Climatology, Academy of Athens, Athens, 11521, Greece
[8~~7~~] Biomedical Research Foundation, Academy of Athens, Athens, 11527, Greece
[9~~8~~] Navarino Environmental Observatory (N.E.O.), Messinia, 24001, Greece
[10~~9~~] Mariolopoulos-Kanaginis Foundation for the Environmental Sciences, Athens, 11251, Greece

Correspondence to: Anna Moustaka (anna.moustaka@pmodwrc.ch)

Abstract. North Africa and the Middle East encompass the most active dust sources on the planet. Due to the limited availability of ground-based aerosol observations across the deserts, spaceborne retrievals represent the most reliable source of information for monitoring dust particles over these vast areas. In the current study, we present a synergistic approach incorporating aerosol retrievals acquired by active (CALIOP) and passive (POLDER-3, MODIS) instruments mounted on satellites of the A-Train constellation. Our main objective is to dynamically (in terms of space and time) estimate the dust lidar ratio (LR) throughout a 12-year ~~CALIPSO~~ period (2006-2017) by collocating columnar aerosol optical depth observations (POLDER-3/GRASP, MIDAS) and vertically resolved dust aerosol profiles obtained by CALIPSO. According to our findings, the derived dust LRs reveal clear and physically meaningful spatial variability. The highest LRs are found over major Saharan source regions such as the Bodélé Depression and the Libyan Desert, while moderate to low values dominate the Arabian Peninsula. Enhanced values also appear across Central Asia, particularly over the Karakum and Kyzylkum deserts. The corresponding uncertainty fields demonstrate that LR estimates are most robust over regions with a larger number of dust cases, whereas higher uncertainties occur along transition zones—such as the Sahel and parts of Central Asia—where dust mixing or aerosol-type misclassification increases retrieval variability~~the agreement among the satellite-based retrievals improves,~~improves ~~when the default and constant CALIPSO dust LR (44 sr) is adjusted~~. ~~Specifically, increasing and decreasing dust LR tendencies are recorded in North Africa and in the Middle East, respectively, whereas a narrow transition zone of neutral declinations appears between the two regions. Furthermore, compared to the standard dust LR, higher values are recorded east of the Caspian Sea, while negative departures are found in Iran and southern Pakistan. The proposed dust LR~~

adjustments are maximized over/near dust sources and during the dry period of the year, indicating a dependence on dust activity. The evaluation against AERONET observations clearly demonstrates that the refined dust LRs improve CALIOP's performance when mineral particles are probed, but further justification is needed. The integration of the refined dust LRs significantly modifies the standard CALIPSO dust optical depth (DOD) climatological patterns, particularly in the Western Sahara, the Bodélé depression (northern Chad Basin), the Libyan Desert and Saudi Arabia. Positive and negative shifts in the regional DOD timeseries are found in North Africa and in the Middle East, respectively, with no notable modifications on the inter annual and intra annual trends in either region. A key objective of this work is to establish a robust methodology for deriving aerosol speciatedaerosol-speciated satellite based lidar ratios LRs using synergies between active and passive satellite observationsobservations. Although developedfocused here onfor dust over North Africa and the Middle East, the same framework can be readily applied to other CALIPSO aerosol subtypes—such as marine, polluted dust, or smoke—when implemented over regions where these aerosol types predominate.A key priority of the analysis carried out is to improve the efficiency of CALIPSO dust retrievals towards advancing their utility in a wide range of scientific applications. The advent of the EarthCARE satellite mission, along with the incorporation of new aerosol models into the forthcoming CALIPSO Version 5 aerosol retrieval algorithm, will serve as a reference for our calculations. In this context, our findings also highlight that a synergy of multisensor aerosol products with modelling tools can enhance the spatiotemporal representation of aerosol properties, such as the LR, further improving retrieval utility.

1 Introduction

Dust aerosols represent a significant component of the global aerosol burden, profoundly influencing climate and various environmental processes (Zender et al., 2004; Textor et al. 2006; Mahowald et al., 2014; Gkikas et al., 2021; 2022; Logothetis et al., 2021; Gkikas et al.; 2022; González-Romero et al., 2023; Castellanos et al., 2024). The most prominent dust sources are located in arid and semi-arid regions, where the prevailing meteorological conditions and the soil characteristics facilitate the mobilization of dust particles (Ginoux et al., 2012; Prospero et al., 2013; Huang et al., 2014; Chen et al., 2018). North Africa features some of the most active dust sources worldwide. The Bodélé Depression in the northern Chad Basin, is recognized as the most prolific single source of mineral dust globally (Warren et al., 2007; Ginoux et al. 2012; Kok et al., 2021), with substantial emissions also emanating from the western Sahara, the eastern Libyan Desert, and the Nubian Desert (Sudan and Egypt) (Engelstaedter et al. 20076). The spatial extent and intensity of these sources vary significantly depending on the prevailing winds and surface conditions (Mbourou et al., 1997; Schepanski, 2018; Tindan et al., 2023).

The Arabian Peninsula also serves as a major source region for mineral dust aerosols. The Rub' al Khali desert, one of the largest continuous sand seas in the world, contributes substantially to regional and global dust loading (Jish Prakash et al. 2015). Other significant sources include alluvial plains within the Tigris-Euphrates river system and sandy deserts across the region (Pease et al., 1998; Hamidi et al., 2013). Dust emissions across the Arabian Peninsula show strong seasonality, influenced by the prevailing winds and the availability of loose, erodible material on the surface (Yu et al., 2013; Yu et al.,

2015; ~~Abdul-Wahab et al. 2017;~~ Solmon et al. 2015). The transport of dust from this region significantly affects the atmospheric composition and radiative balance of the Middle East, ~~and~~ western parts of Asia and the Eastern Mediterranean (Jish Prakash et al., 2015). Desert regions in Central Asia contribute to global dust emissions, albeit typically at lower intensities than those in North Africa and the Arabian Peninsula (Xiong et al., 2020). Among these, the Karakum Desert (Turkmenistan) and the Kyzylkum Desert (spanning Uzbekistan and Kazakhstan) stand out as smaller yet significant sources of regional dust loading (Li and Sokolik, 2018). These deserts share similar arid characteristics, but their dust production and transport are influenced by unique geographical factors and meteorological conditions (Banks et al., 2022).

The complex nature of mineral dust aerosols, in terms of particle sizes, shapes, and compositions (Castellanos et al., 2024), leads to significant challenges for accurate remote sensing and modeling, necessitating the deployment of advanced observational techniques. Ground-based measurements employing passive and active remote sensing techniques have provided invaluable long-term data on aerosol intensive and extensive properties (Groß et al., 2011; 2015; Burton et al., 2012; Baars, et al., 2016; Benkhalifa et al., 2017; Haarig et al., 2017a; 2017b; 2022; Ningombam et al. 2019; ~~-~~Hofer et al., 2020; Raptis et al. 2020; Yu et al., 2022; ~~Zhang et al., 2022; Eom et al., 2022~~). Spaceborne observations from passive sensors, such as those from the Moderate Resolution Imaging Spectroradiometer (MODIS) onboard Terra and Aqua satellites, have delivered multi-year records of columnar aerosol optical depth (AOD) with near-global coverage since 2000 (Luo et al., 2014; Mao et al., 2014; Gupta et al., 2020; Gkikas et al., 2021; Kang et al., 2023). The recently developed MODIS Dust Aerosol (MIDAS) dataset (Gkikas et al., 2021; 2022) further refines dust-specific AOD by combining MODIS-Aqua quality-assured AOD retrievals with Modern-Era Retrospective analysis for Research and Applications version 2 (MERRA-2; Gelaro et al., 2017) reanalysis dust fraction ratios (in optical terms), offering a high-resolution record of daily dust optical depth (DOD) on a global scale, spanning from 2003 to 2017 (Gkikas et al., 2021). Additionally, the multi-angle, multi-spectral polarimetric (MAP) measurements have been providing comprehensive data on aerosol particle size, shape, and refractive index, enabling detailed characterization of aerosols' properties and interactions within the atmosphere since the mid-1990s (Hansen et al., 1995; Mishchenko and Travis~~et al.~~, 1997a; 1997~~,~~b). Polarimetric measurements from the Polarization and Directionality of the Earth's Reflectances (POLDER-3) on the PARASOL platform exemplify the contributions of MAP technology to aerosol science. When combined with the Generalized Retrieval of Atmosphere (GRASP), the linearly polarized and total radiances from POLDER-3 sensor enables the retrieval of detailed aerosol properties, such as particle size distribution, complex refractive indices, and sphericity. Furthermore, POLDER-3/GRASP achieves high-quality AOD ~~and absorption retrievals~~ (Dubovik et al., 2011; Li et al., 2019; Chen et al., 2020; Zhang et al., 2021), validated effectively against AERONET stations (Chen et al., 2020; Zhang et al., 2021).

Along with space-borne passive sensors measuring the reflectance at the top of the atmosphere (TOA), active remote sensing techniques, offer superior capabilities for resolving the vertical distribution of aerosols throughout the atmosphere. From June 2006 to August 2023, the Cloud-Aerosol Lidar with Orthogonal Polarization (CALIOP) instrument onboard the Cloud-Aerosol Lidar and Infrared Pathfinder Satellite Observation (CALIPSO) satellite provided vertically resolved aerosol retrievals, both day and night, at high spatial and temporal resolutions, regardless the underlying surface type (Winker et al., 2010). Among

the prediscussed limitations of the CALIOP's elastic lidar in a number of previous studies (Winker et al., 2009; Ma et al., 2013; Kim et al., 2018; Gui et al., 2022; Haarig et al., 2018; Li et al., 2022; Moustaka et al., 2024), the accuracy of CALIPSO's AOD retrievals is highly contingent on the predetermined extinction-to-backscatter ratio, a key parameter defined as lidar ratio (LR), which varies significantly depending on aerosol types. This dependency can lead to inaccuracies, especially if the LR assigned to an aerosol type does not adequately reflect its true microphysical characteristics. ~~Past studies~~Schuster et al. (2012) indicated that CALIPSO's AOD is often underestimated by approximately 13% when compared to AERONET. This underestimation is attributed to both aerosol misclassification and inaccuracies in the modeled microphysics for certain aerosol types, such as polluted dust or smoke. ~~(Schuster et al., 2012).~~ Additionally, CALIOP's ability to measure particle linear depolarization at 532 nm has provided great insights into identifying non-spherical mineral dust particles (Burton et al., 2013). Specifically, for the non-spherical dust particles, the study from Amiridis et al. (2013) has shown that the increase of dust LR over the Sahara leads to better accuracy of AOD ~~calculations~~ by reducing the observed discrepancies compared to MODIS and AERONET. According to a more recent study from Moustaka et al. (2024), the authors used the DeLiAn database (Depolarization ratio, Lidar ratio, and Ångström exponent database; Floutsi et al., 2023), a collection of state-of-the-art ground-based lidar observations acquired in areas characterized by different aerosol conditions, in order to estimate the effect of an updated aerosol-speciated LR on AOD and subsequently to the direct radiative effects (DREs) across the North Africa, Middle East and Europe domain (NAMEE). Using DeLiAn-derived LRs reduced differences between CALIPSO and AERONET observations in dust-dominated regions, leading to more reliable DRE estimates. Under moderate-to-high aerosol loads, this approach enhanced the calculated surface cooling and atmospheric warming by up to 35%. ~~The use of DeLiAn-derived LRs improved accuracy, particularly for dust-dominated regions, resulting in more reliable DRE calculations and specifically decreased discrepancies between CALIPSO and AERONET observations. This notably enhanced the surface cooling and atmospheric warming estimates by up to 35% under moderate-to-high aerosol loads.~~ These findings along with those of past relevant studies (Omar et al., 2013; Konsta et al., 2018) underscore the importance of accurately determining the dust LR, across major desert regions over the globe. The adaptation of a more 'realistic' dust LR can enhance the accuracy of elastic lidar-derived AOD estimates. ~~The adaptation of a more "realistic" dust LR, along with more reliable elastic lidar-derived AOD values, could contribute to a more robust aerosol typing. This can be achieved through synergistic approaches by also implementing measurements from the recently launched EarthCARE (Cloud, Aerosol, and Radiation Explorer) platform, which is a joint mission of the European Space Agency (ESA) and the Japan Aerospace Exploration Agency (JAXA) (Illingworth et al., 2015; Wandinger et al., 2023).~~ In addition to the LR, other properties of dust, including its emission ~~processes~~processes, mineralogical composition, and morphology, are crucial for assessing its climatic role, as they influence key optical characteristics like DOD, single scattering albedo (SSA), and refractive index, which are essential inputs for radiative transfer models (RTMs). A deeper understanding of these properties allows for a more accurate representation of dust~~'s~~ microphysical characteristics and radiative effects, ultimately improving climate predictions and reducing uncertainties in dust-related DREs (Kok et al., 2017; ~~Kok et al.,~~ 2023).

Our study focuses on improving dust aerosol monitoring across North Africa and the Middle East by refining dust LR estimates via a synergistic approach between active and passive sensors of the A-Train satellite constellation. Based on the CALIPSO aerosol classification scheme, which uses accurate depolarization measurements of the CALIOP lidar to detect non-spherical dust layers, we focus on dust cases. We aim to adjust the dust LR so that the CALIOP DOD at 532 nm matches the coincident columnar observations from the MIDAS (from 2007 to 2017) and POLDER-3/GRASP (from 2006 to 2009) datasets (Section 2). Section 3 provides the full methodological framework, including the definition of dust cases, the multisensor matchup strategy, the estimation and propagation of DOD uncertainties within the A-Train constellation, and the derivation of the dust LR together with its associated uncertainties. ~~the estimation of relative DOD uncertainties within the A-Train constellation, and the derivation of the dust lidar ratio.~~ ~~The identification of the dust cases, along with the methodology for the adjustment of dust LRs between the different sensors are provided in Section 3.~~ In Section 4, we present the geographical distribution of dust LR on an annual and seasonal basis, along with the associated uncertainties.~~.~~ ~~This analysis begins with the examination of the DOD retrievals used to adjust LR within the A-Train constellation. Additionally, to evaluate the effect of dust LR on CALIOP's columnar DOD retrievals an assessment analysis using AERONET ground-based observations has been performed.~~ ~~s~~ Finally, Section 5 summarizes the main findings and discusses future aspects of the work, including a summary ~~table~~table of regional dust LR estimates that can serve as a practical reference for subsequent studies.~~Following the evaluation analysis, we examine the impact of the updated LRs on dust climatological patterns and regional levels. As a concluding step in assessing the adjusted dust LRs, we present the inter-annual and intra-annual DOD time series for the 2007–2022 period, analyzed separately for North Africa and the Middle East. Finally, Section 5 summarizes the main findings and discusses future aspects.~~

2 Data sets

2.1 CALIOP-CALIPSO Spaceborne Retrievals

From April 2006 to August 2023, the Cloud-Aerosol Lidar with Orthogonal Polarization (CALIOP) on the Cloud-Aerosol Lidar and Infrared Pathfinder Satellite Observations (CALIPSO) satellite has significantly enhanced our understanding of aerosol and cloud interactions and their roles in the climate system (Winker et al., 2009). CALIOP operates as a dual-wavelength backscatter (532 and 1064 nm) and single-wavelength polarization (532 nm) lidar system. The horizontal averaging and the vertical resolution of the system varies depending on both the altitude and the wavelength.~~with horizontal averaging and vertical resolution variable based on both wavelength and altitude~~ (Winker et al., 2009). This system aids in distinguishing aerosols from clouds and differentiating between fine and coarse-mode aerosol layers, while its depolarization signal is essential for distinguishing between spherical particles (e.g., marine particles, liquid cloud droplets) and non-spherical particles (e.g., dust, ice cloud particles) within the atmosphere (McGill et al., 2007; Hu et al., 2009; Omar et al., 2009; Burton et al., 2012; ~~Burton et al.,~~ 2013; Kim et al., 2018).

The latest version 4.5 (V4.5) of the CALIOP level 2 (L2) aerosol classification product, besides the more comprehensive and accurate definitions of stratospheric particles (Tackett et al., 2023), preserves the same rationality with the previous V4 versions

for the tropospheric aerosol layers, using layer-integrated values of depolarization and attenuated backscatter from L1 data, along with geographical location, surface type, and layer altitude information, to assign distinct aerosol types (Kim et al., 2018). The CALIPSO algorithm classifies tropospheric aerosols into seven categories: "marine," "dust," "polluted continental/smoke," "clean continental," "polluted dust," "elevated smoke," and "dusty marine." Dust is one of the most well-characterized subtypes (Burton et al., 2013), thanks to CALIOP's accurate depolarization measurements, which enable the detection of non-spherical dust layers. Critical quality filters are applied during CALIOP-CALIPSO data processing to minimize errors in layer detection, classification, and extinction retrieval, as well as biases from negative signal anomalies. Cloud contamination is also mitigated using the cloud aerosol discrimination (CAD) algorithm and by applying misclassified cirrus fringe filters (Marinou et al., 2017; Proestakis et al., 2018; Tackett et al., 2018~~; Proestakis et al., 2018; Marinou et al., 2017~~).

In the present study, based on the CALIPSO aerosol subtype product, we identify dust scenes during daytime satellite orbits and we exploit quality-assured (QA) vertical profiles of the ~~backscatter~~ extinction coefficient at 532 nm, including the corresponding uncertainty estimates, sourced from the LIVAS (Lidar climatology of Vertical Aerosol Structure) database (Amiridis et al., 2015), for the computation of the columnar dust optical depth (DOD) and its relative uncertainty, over a 12-year period (June 2006 to December 2017). LIVAS is a comprehensive 3-D multi-wavelength database that provides global aerosol and cloud optical properties based on CALIPSO observations at 532 and 1064 nm with a resolution of 1º × ~~x~~1º. For the LIVAS development, the ESA-CALIPSO dataset (Wandinger et al., 2011), the EARLINET (The EARLINET publishing group 2000–2010) and AERONET products (Holben et al., 1998; 2001), along with aerosol models in the literature (Deshler et al., 1993; Wandinger et al., 1995; Omar et al., 2005; Sayer et al., 2012), were integrated. Since its inception, LIVAS has supported numerous studies related to dust climatology and retrieval optimization (Marinou et al., 2017; Proestakis et al., 2018; Moustaka et al., 2023; ~~Moustaka et al.~~ 2024), new dataset development (Fountoulakis et al., 2021; ~~Fountoulakis et al.,~~ 2022; Papachristopoulou et al., 2022), and the evaluation of aerosol effects on solar radiation models (Konsta et al., 2018; Moustaka et al., 2024). In addition to the aerosol products, the temperature and pressure profiles (included in CALIOP auxiliary datasets) originating from the NASA Global Modeling and Assimilation Office (GMAO) meteorological analyses (NASA Langley Research Center, 2007) were also employed for the estimation of the molecular backscatter profiles required in Eq. (9)#, as discussed in detail in Section 3#.3#.

2.2 ModIs Dust AeroSol (MIDAS) dataset

The ModIs Dust AeroSol (MIDAS) dataset (Gkikas et al., 2021) was developed to focus specifically on dust aerosols by estimating dust optical depth (DOD) at a global scale and fine spatial resolution (0.1° × ~~x~~ 0.1°). The MIDAS product spans a 15-year period (2003–2017) and integrates MODIS-Aqua AOD retrievals with the dust-specific information from the Modern-Era Retrospective analysis for Research and Applications version 2 (MERRA-2) reanalysis, which provides the dust fraction to the total aerosol load. The MIDAS development process includes multiple steps to ensure high-quality dust aerosol data, such as quality filtering, spatial and temporal colocation, and error estimation.

To generate the MIDAS DOD product, a synergy between MODIS-Aqua L2 AOD retrievals and MERRA-2 dust-to-total AOD ratios are employed. The integration of MODIS AOD with MERRA-2 dust fraction requires careful spatial and temporal colocation. Since MERRA-2 outputs are available at a coarser spatial resolution (0.5° × ~~x~~ 0.625°) compared to MODIS's fine-resolution grid (10 km × ~~x~~ 10 km), the nearest MERRA-2 grid points to the MODIS swath-level retrievals are selected. The time colocation also considers the nearest hourly MERRA-2 data corresponding to the MODIS overpass. The MIDAS product employs a series of filtering criteria to enhance the accuracy of its AOD retrievals from MODIS. First, only high-quality MODIS AOD data are used, based on quality assurance (QA) flags, where only retrievals with QA flags of "good" or "very good" are included. In addition, data points with cloud fractions greater than 0.8 or lacking adjacent retrievals are discarded to minimize cloud contamination, following the recommendations of earlier studies (Anderson et al., 2005; Zhang and Reid, 2006; Hyer et al., 2011; Shi et al., 2011) .

MIDAS has been validated against ground-based AERONET data, showing a strong correlation (R = 0.89) and only a slight positive bias of 2.7% on a global scale (Gkikas et al., 2021). This demonstrates that the MIDAS product accurately represents dust aerosols, especially over key dust regions like North Africa, the Middle East, and Asia. The MIDAS dataset also offers an improvement over existing datasets by providing finer spatial resolution and more accurate dust-specific retrievals, while from its establishment it has supported a lot of studies focusing on dust climatology (Gkikas et al., 2022) and trends (Logothetis et al., 2021), model simulations in respect to emission and transport of dust particles (Kiriakidis et al., 2023) and dust impact on solar energy production (Masoom et al., 2021; Papachristopoulou et al., 2022). We exploit the MIDAS columnar DOD product at 550 nm, while CALIPSO provides observations at 532 nm. Given that pure dust is characterized by Ångström exponent values close to zero, the difference between 550 nm and 532 nm is expected to be negligible. For this study, we analys~~z~~e the 550 nm DOD at a 1º × ~~x~~ 1º spatial resolution over the 10-year period (2007–2017), ensuring consistency with the CALIPSO mission, as MODIS-Aqua lowered its orbit relative to CALIPSO in early 2018, affecting their observational overlap.

2.3 POLDER-3 and GRASP/Components

The POLDER-3 (Polarization and Directionality of Earth's Reflectances) sensor, onboard the PARASOL (Polarisation and Anisotropy of Reflectances for Atmospheric Science coupled with Observations from a Lidar) satellite, was developed to improve the characterization of aerosol optical properties through multi-angle, multi-spectral, and polarimetric observations (Steinmetz et al., 2005; Chen et al., 2020; Dubovik et al., 2021; Zhang et al., 2021). POLDER-3 collected radiance measurements across six spectral channels (443, 490, 565, 670, 865 and 1020 nm) and polarization measurements at three channels (490, 670, and 865 nm), allowing it to provide unique insights into aerosol properties by capturing data from up to 16 viewing angles per pixel (Dubovik et al., 2011). This multi-angle capability facilitated global coverage every two days, offering valuable information about the size, shape, and composition of aerosol particles (Dubovik et al., 2011).

The Generalized Retrieval of Aerosol and Surface Properties (GRASP) algorithm, applied to POLDER-3 data, derives detailed aerosol and surface properties, with a component-based approach enhancing the characterization of aerosol properties (Dubovik et al., 2011). In this framework, aerosols are modeled as mixtures of various components—such as hydrated soluble,

black carbon, brown carbon, and iron oxides—representative of different aerosol species and characterized by specific chemical compositions and known refractive indices (Dubovik et al., 2006; Schuster et al., 2016). The GRASP/Component algorithm provides daily retrievals of aerosol optical properties like aerosol optical depth (AOD), Ångström exponent (AE), fine-mode AOD (AODF), coarse-mode AOD (AODC), single scattering albedo (SSA) and refractive indices as well as detailed information on aerosol composition and particle size distribution in 0.1° × ~~*~~0.1° or 1° × ~~*~~1° spatial resolution from 2005 to 2013 (Li et al., 2019; Dubovik et al., 2021).

In terms of validation, the GRASP/Component method has demonstrated strong agreement with AERONET stations, particularly for AOD, with negligible bias over both land and ocean (Li et al., 2019; Zhang et al., 2021). Fine-mode and coarse-mode AOD retrievals similarly align well with AERONET, and SSA and AE retrievals from GRASP exhibit high accuracy, enhancing the reliability of aerosol property assessments on a global scale (Li et al., 2019; Dubovik et al., 2021; Zhang et al., 2021). By utilizing advanced radiative transfer calculations without reliance on look-up tables, the GRASP/Component method has achieved high accuracy in aerosol property retrievals (Dubovik et al., 2021). In the present study, we exploit the L3 daily POLDER-3/GRASP-Component AOD retrievals at a 1° × ~~*~~1° spatial resolution for the period when the CALIPSO and PARASOL satellites were flying in tandem in the A-Train constellation (June 2006 – early December 2009). Since POLDER-3/GRASP-Component AOD is not provided exactly at 532 nm, the Ångström formula (Ångström, 1929) is applied on the ~~we interpolate between the~~ available POLDER-3/GRASP wavelengths (i.e., 440, 670) to derive AOD at 532 nm for consistency with CALIPSO observations. Specifically, the interpolation of AOD at 532 is articulated through the following equations:~~.~~

$$\dot{a} = -\frac{\ln\left(\frac{\mathrm{AOD}_{\lambda 0}}{\mathrm{AOD}_{\lambda 1}}\right)}{\ln\left(\frac{\lambda_0}{\lambda_1}\right)}, \quad (1)$$

$$\mathrm{AOD}_{\lambda} = \mathrm{AOD}_{\lambda 0} \cdot \left(\frac{\lambda_0}{\lambda}\right)^{\dot{a}}, \quad (2)$$

where λ refers to the 532 nm, λ_0 to the 440 nm, λ_1 to the 670 nm and å is the Ångström exponent across the 440-670 nm wavelength range.

~~2.4 AERONET~~

~~AERONET (AErosol RObotic NETwork) is a global network with over 1,000 automated sun photometers (Holben et al., 1998; 2001) that measure aerosol columnar optical and microphysical properties in different wavelengths. In this study, we utilize the sun-direct retrievals from AERONET in order to assess the impact of the CALIOP default versus the updated dust LR values on the columnar AODs (Dubovik et al., 2000; 2006). Specifically, we exploit the latest version (V3) of high-quality, Level 2.0 AERONET data, which includes observations at the highest available temporal resolution (i.e., all data points) (Giles~~

et al. 2019; Sinyuk et al., 2020). To align the spectral columnar AOD (440, 675, 870, 1020 nm) from the AERONET stations with the AOD at 532 nm from CALIOP-CALIOP, we apply the following Ångström formula (Wagner and Silva, 2007):

$$AOD_{\lambda} = AOD_{\lambda 0} \cdot \left(\frac{\lambda_0}{\lambda}\right)^{\mathring{a}\left(\frac{\lambda_0}{\lambda}\right)} \quad (1)$$

, where λ refers to the 532 nm, λ_0 to the 440 nm and å is the Ångström exponent across the 440-675 nm wavelength range.

3 Methodology

Our region of interest (ROI) encompasses the major and most active deserts of the planet situated in North Africa and in the broader region of the Middle East (Ginoux et al., 2012), as illustrated in Fig. 1. The selected desert regions, as defined in Ginoux et al. (2012), are presented in Fig. 1a as defined in Ginoux et al. (2012). ROI hosts major dust sources, primarily over North Africa (yellow-shaded area), including the Bodélé Depression in the northern Chad Basin, the eastern Libyan Desert, the Nubian Desert, and parts of western Africa. In the Middle East (purple-shaded area), significant sources include the Arabian Desert, with the Rub' al Khali and the Mesopotamian region between the Tigris and Euphrates rivers, as well as the deserts of western Central Asia, notably the Karakum and Kyzylkum (Ginoux et al., 2012; Hamidi et al., 2013; Gkikas et al., 2022). Within these broader desert domains, our analysis further focuses on a set of 10 sub-regions defined over the most active and representative dust-producing areas (Fig. 1). ROI hosts major dust sources, primarily over North Africa (yellow-shaded area), including the Bodélé Depression in the northern Chad Basin, the eastern Libyan Desert, the Nubian Desert, and some regions in western Africa. In the Middle East (purple-shaded area), significant sources include the Arabian Desert, with the Rub' al Khali and the Mesopotamian region between the Tigris and Euphrates, as well as deserts in the western parts of Central Asia, notably the Karakum and Kyzylkum (Ginoux et al., 2012; Hamidi et al., 2013; Gkikas et al., 2022). Subsequently, based on the CALIPSO aerosol subtype product, we focus on dust cases, and finally we adjust the dust LR such as the CALIOP DOD at 532 nm to match the columnar DODs from MIDAS and POLDER-3/GRASP. Dust is the most well-characterized subtype of the CALIPSO aerosol product (Burton et al., 2013), due to the accurate depolarization measurements of CALIOP, which enable the detection of non-spherical dust layers. The AOD products from MIDAS and POLDER-3/GRASP have also demonstrated a strong validation performance in evaluations assessment studies against AERONET observations (Dubovik et al., 2011; Li et al., 2019; Gkikas et al., 2021; Zhang et al., 2021). A synergistic use There are also very good validation metrics for the AOD products of MIDAS and POLDER-3/GRASP from evaluation studies against AERONET stations (Dubovik et al., 2011; Li et al., 2019; Gkikas et al., 2021; Zhang et al., 2021). The collaboration of these active and passive sensors of the A-Train constellation can lead to the derivation of noteworthy dust LR patterns over the most well-known dust regions around the globe.

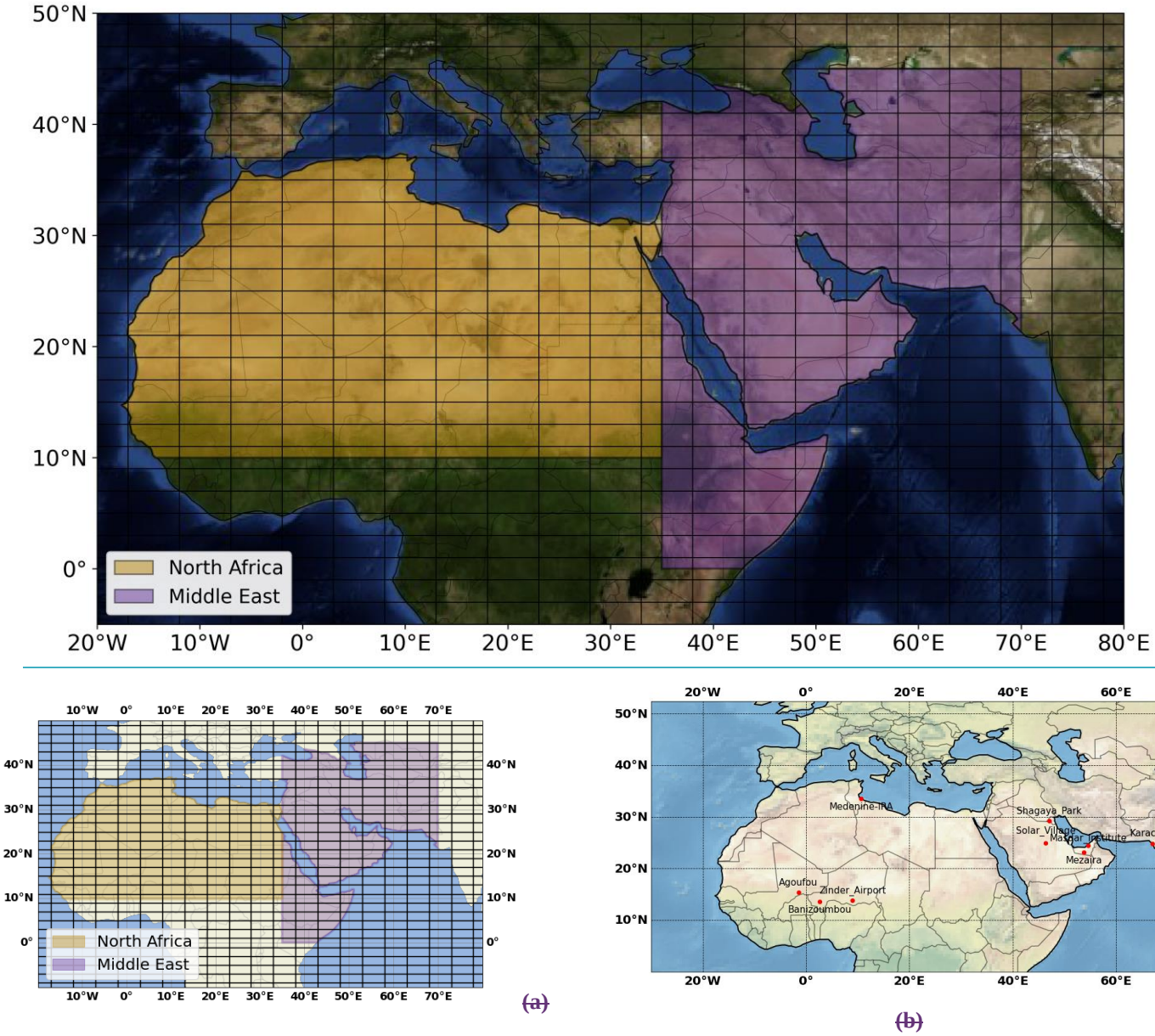

Figure 1: ~~(a)~~ **The North Africa (yellow-shaded area) and the Middle East (purple-shaded area) desert regions as defined based on Ginoux et al. (2012). The domain is divided into grids with 2° × ~~x~~5° spatial resolution grids based on Winker et al. (2013) in order to minimize the signal error in CALIPSO mean profiles.** ~~. The colored boxes denote the 10 sub-regions: Central Sahara (CS), Western Outflow Zone (WOZ), Northwestern Sahara (NWS), Northeastern Sahara (NES), Western Sahara (WS), Eastern Sahara (ES), Central Asia (CA), Northern Arabian Peninsula (NAP), Central Arabian Peninsula (CAP), and Southern Arabian Peninsula (SAP).~~ **Map source: NASA Earth Observatory.** ~~, and (b) the AERONET stations over North Africa and Middle East used for evaluating CALIOP DODs.~~

3.1 Definition of dust cases

Initially, the domain is divided into grids with 2º × ~~x~~5º spatial resolution, following the CALIPSO Level 3 (L3) official spatial resolution applied towards reducing the signal noise contamination in the mean vertical profiles (Winker et al., 2013; Tackett et al. 2018). The segments of the CALIPSO orbit traversing desert regions were identified. The corresponding Level-2 (L2) 5-km aerosol profiles were then grouped into predefined 2° × 5° grids based on their geospatial coordinates. ~~The part of CALIPSO orbit residing within the desert regions is identified (Fig. 2a) and accordingly the Level 2 (L2) 5 km aerosol profiles are in terms of their geospatial coordinates grouped in predefined 2ºx5º deg grids.~~ Considering the segment of the orbit residing within each grid cell, the following criteria must be fulfilled for an overpass to be classified as a dust case: ~~With respect to the part of the orbit falling inside each grid the following criteria need to be satisfied in order for an overpass to be classified as a dust case:~~

(i) dust classified atmospheric layers (based only on the aerosol subtype classification product of CALIPSO; Kim et al., 2018) should be at least the 95% of the total aerosol records,

(ii) there should be no disturbance in mean profiles due to filtering processes (i.e., uniform extinction profiles without any vertical cut-off due to filtering along the overpass),

(iii) there should be no clouds detected ("clear-sky" conditions), and

(iv) CALIOP beam should be penetrating throughout the atmosphere reaching the Earth's surface level.

~~Overall, on the basis of CALIOP observations in the period June 2006-August 2023 over the regions of interest, 6,915 dust cases were identified fulfilling the aforementioned criteria.~~

In Fig. 2, we present, as an indicative example, one ~~of 6,915 dust cases~~of the defined dust cases to illustrate the applied CALIOP-based processing for a specific grid cell over the Saharan Desert (center of the grid: lat 22.00, lon 15.5). For the part of the CALIPSO L2 5 km aerosol profiles residing within the grid area (confined between the magenta vertical dashed lines in Fig. 2b), the CALIOP-provided extinction coefficient profiles at 532 nm are spatially averaged ~~in order~~ to derive a mean extinction coefficient vertical profile (Fig. 2c). Due to the strict filtering criteria applied for the definition of dust cases, we assume the sole presence of dust in the selected cases. Accordingly, the mean extinction coefficient profile is computed exclusively from atmospheric layers classified as "dust" by the CALIOP aerosol subtype algorithm (Kim et al., 2018), while contributions from dust mixtures (i.e., polluted dust and dusty marine) are excluded. This approach, supported by consistently high particulate depolarization ratios (> 0.27; Fig. S1) observed in the selected cases, ensures that the retrieved extinction profiles are representative of pure dust aerosols. Within this framework, the mean extinction coefficient profile retrieved for the identified dust cases is hereafter referred to as dust extinction throughout the remainder of the study.

The dust extinction coefficient profiles (a^{d}_{CALIOP}) and their associated uncertainties ($\sigma^{\mathrm{d}}_{\alpha,\mathrm{CALIOP}}$) used in this study are provided within the LIVAS dataset. Once the mean dust extinction coefficient profile is obtained for the selected dust layers within the grid, it is vertically integrated to derive the corresponding dust DOD at 532 nm for each identified dust case. It should be noted that the vertical integration is performed only over the atmospheric layers identified as containing dust — potentially spanning

multiple non-contiguous layers — while dust-free regions in between, above, or below the dust layers do not contribute to the DOD.

CALIPSO orbit: 2008-04-17T12-02-27ZD

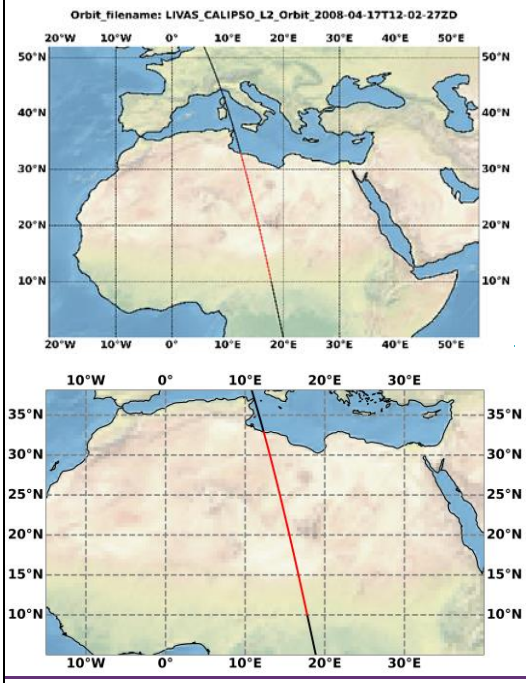

(a)

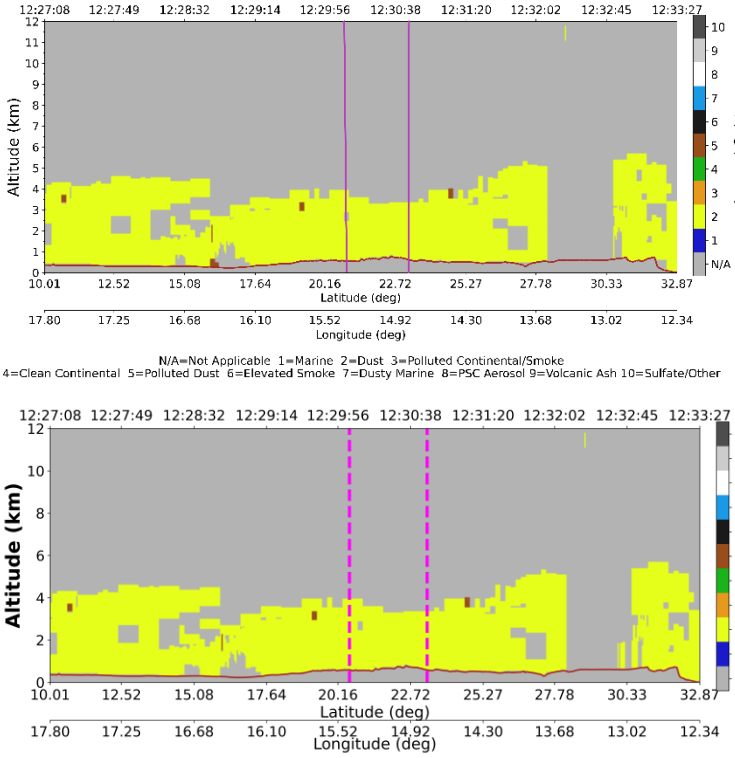

(b)

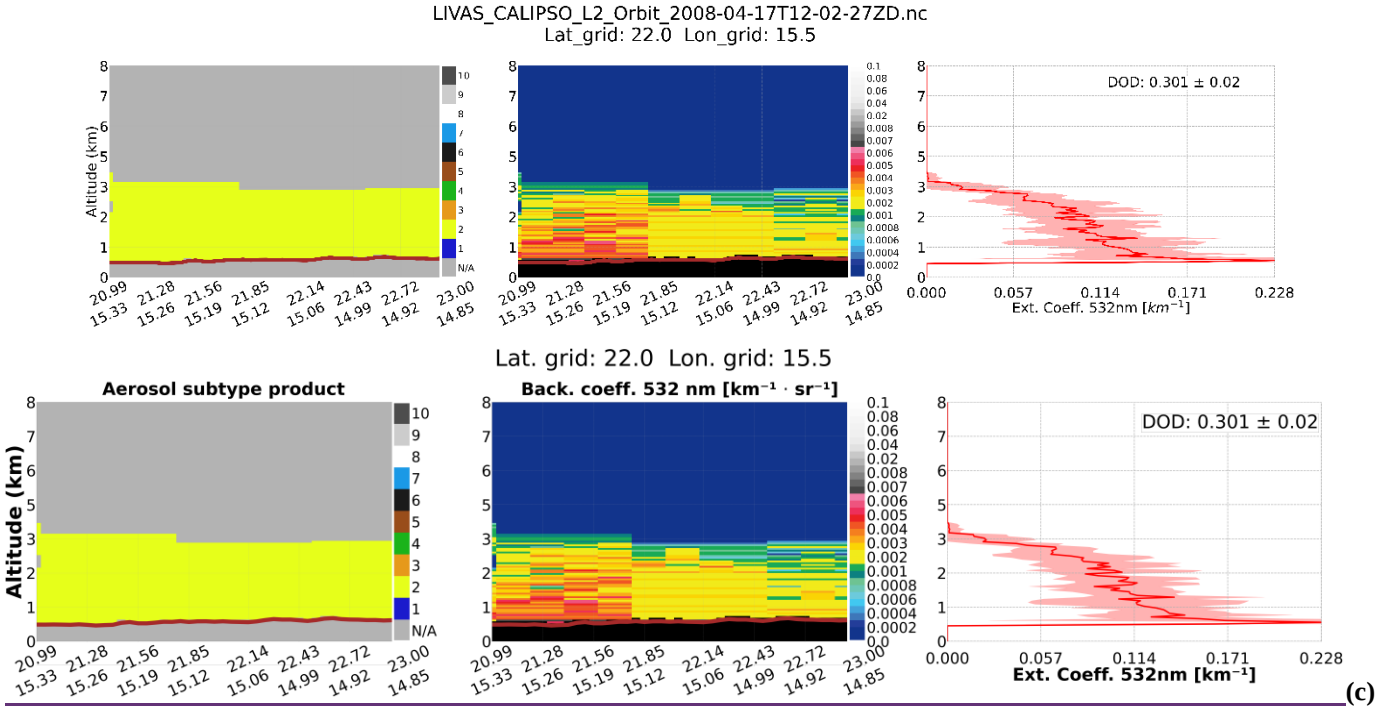

Figure 2: (a) A single CALIPSO orbit (2008-04-17T12-02-27ZD) over North Africa (the part of the orbit falling inside the desert region is colored red), (b) the respective aerosol subtype curtain plot for the red part of the orbit, and (c) the part of the orbit falling inside a specific grid (center of the grid→lat:22.00, lon:15.5), defined with the two magenta~~purple~~ vertical dashed lines in (b). The CALIPSO V4 aerosol subtype product (left panel) indicating the presence of pure dust (N/A: not an aerosol layer, 1: marine, 2: dust, 3: polluted continental/smoke, 4: clean continental, 5: polluted dust, 6: elevated smoke, 7: dusty marine, 8: PSC aerosol, 9: volcanic ash, 10: sulfate/other) and the backscatter coefficient 532 nm [$km^{-1} \cdot sr^{-1}$] (central panel). Vertical profile of the spatially averaged extinction coefficient 532 nm (right panel) along with its standard deviation (red-shaded area) for the respective orbit, along with the corresponding columnar DOD based on CALIPSO dust LR (44 sr).

3.2 Match-Up Methodology and Relative DOD Uncertainty Estimation ~~within the A-Train Constellation~~ ~~Match-up methodology between A-Train constellation~~

After the identification of the dust cases based on CALIPSO, we identify the coincident 1° × ~~*~~1° products from MIDAS (DOD) and POLDER-3/GRASP (AOD) datasets. For MIDAS, we check the 10-year period spanning from 2007 to 2017, while for the POLDER-3/GRASP, the collocated period starts in June 2006 and ends in December 2009, as this marks the point when the PARASOL satellite's orbit was lowered to under the A-Train constellation. Additional to MIDAS and CALIPSO DOD, as long as we focus on the solely presence of dust ~~cases~~ particles based on CALIOP aerosol subtype algorithm, and we search for coincident POLDER-3/GRASP products, we can refer to DOD instead of the term of AOD for its retrievals.

The match-up procedure is thoroughly presented in Fig. 3, while the filters that are applied on the 1° × ~~*~~1° MIDAS and POLDER-3/GRASP grids for quality assurance control and for the extraction of coastal pixels are outlined in Table 1. A random 2° × ~~*~~5° predefined grid is presented (purple square), divided into 10 subgrids with 1° × ~~*~~1° spatial resolution (green~~red~~ squares), which is the resolution of MIDAS and POLDER-3/GRASP products utilized in the current study. For a specific CALIPSO orbit (~~purple~~ cyan points), the grey shaded 1° × ~~*~~1° grids are ~~th~~those from passive sensors (MIDAS, POLDER-

3/GRASP)e ones coincident with the CALIPSO overpass. For these grids to be included in the mean columnar DOD computation from MIDAS and POLDER-3/GRASP products, they must meet the criteria outlined in Table 1. The "LandPercentage" and "Land_sea_Flag" filters are applied to POLDER-3/GRASP and MIDAS products respectively, to exclude coastal pixels. Additionally, a threshold of 0.05 for "ResidualRelative" (the mean root square of relative error from fitting POLDER-3 non-polarised radiance measurements by the GRASP algorithm) is applied as recommended in several studies (Dubovik et al., 2011; Chen et al., 2020; Zhang et al., 2021) to ensure more reliable aerosol retrievals. For MIDAS product, no additional criteria need to be employed in the filtering process, as long as during its development only high-quality data were used (Gkikas et al., 2021). If there is at least a single 1°x1° grid fulfilling the aforementioned criteriacriteria, we process to the computation of the mean columnar DOD from MIDAS and POLDER-3/GRASP products and these values are assigned to the 2° × 5° predefined grid.

Table 1: Filters applied on POLDER-3/GRASP and MIDAS products to select quality-assured data while ensuring the elimination of coastal regions.

POLDER-3/GRASP	**"ResidualRelative" < 0.05** **"LandPercentage" = 100**
MIDAS	**"Land_sea_Flag" = 1**

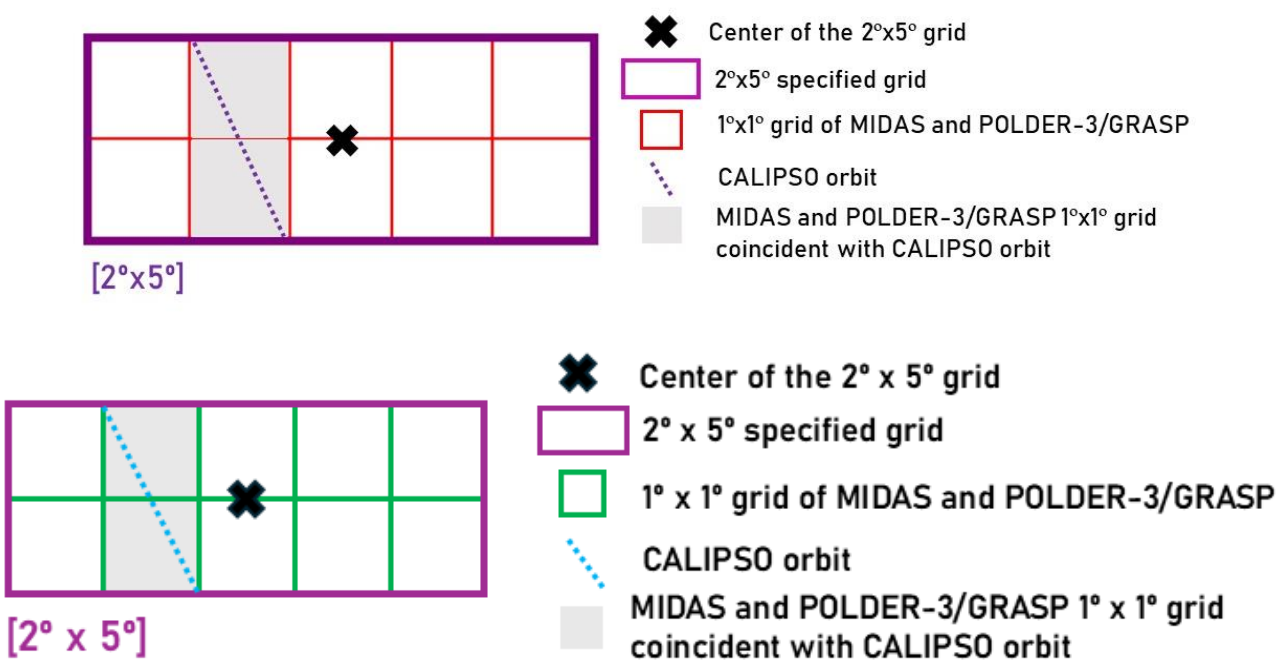

Figure 3: Schematic representation of the spatial match-up methodology used to compare CALIPSO-derived aerosol properties, provided on a predefined 2° × 5° grid (outlined in purple), with the higher-resolution 1° × 1° grids of the MIDAS and POLDER-3/GRASP products (outlined in green). The black cross marks the center of the selected CALIPSO 2° × 5° grid cell. The blue dashed

line represents the CALIPSO satellite orbit. MIDAS and POLDER-3/GRASP 1~~1~~° × ~~*~~1° grid cells that intersect the CALIPSO orbit are highlighted in light grea~~a~~y. Only the coincident 1° × ~~*~~1° grid cells within the selected 2° × ~~*~~5° region are considered for the match-up.

~~Schematic representation of match-up methodology between 2°x5° predefined CALIPSO grids and the 1°x1° resolution of MIDAS and POLDER-3/GRASP products.~~

~~Following the match-up methodology described above, 5,591 and 1,817 collocated pairs were obtained for the CALIOP-MIDAS and CALIOP-POLDER-3/GRASP synergies, respectively.~~ In this subsection, we describe the methodology followed to estimate the absolute and relative uncertainties of the DOD products used in this study, namely those derived from CALIOP, POLDER-3/GRASP, and MIDAS, for each of the collocated dust cases. These uncertainties are used as a quantitative criterion to retain only "reliable" retrievals in the subsequent comparisons, as well as a direct input to the Monte Carlo framework employed for the estimation of the uncertainties of the random uncertainty of LR retrieval~~the LR~~, as described in Section 3.3.2. ~~the following section.~~ A consistent uncertainty characterization is therefore essential for both the quality control of the datasets and the robustness of the LR uncertainty assessment.

For CALIOP, the absolute uncertainty of DOD is estimated by propagating the extinction uncertainties provided by the LIVAS dataset through the numerical vertical integration scheme. Assuming uncorrelated errors between the vertical levels, the propagated absolute uncertainty is given by:

$$\sigma_{\mathrm{CALIOP}}^{\mathrm{DOD}}\sigma = \Delta z \cdot \sqrt{\sum_{i=1}^{N} \sigma_{\alpha_{i_t}}^2 - \frac{\sigma_{\alpha_{1_t}}^2 + \sigma_{\alpha_N}^2}{2}}, \quad (3)$$

where σ_{α_i} denotes the uncertainty of the dust extinction coefficient at altitudinal level i and Δz is the vertical resolution of the CALIOP profile. The DOD relative uncertainty is then defined as:

$$\sigma_{\mathrm{CALIOP}}^{\mathrm{rel}} = \frac{\sigma_{\mathrm{CALIOP}}^{\mathrm{DOD}}}{\sqrt{N} \cdot \mathrm{DOD}_{\mathrm{CALIOP}}}, \quad (4)$$

$$\sigma_{\mathrm{caliop}}^{\mathrm{rel}} = \frac{\sigma}{\sqrt{N} \cdot \mathrm{DOD}}, \quad (4)$$

where N is the number of CALIOP profiles overpassing each 2° × ~~*~~5° predefined grid.

For MIDAS, the DOD uncertainty is estimated following the uncertainty parameterizations adopted for the MODIS Dark Target (DT) and Deep Blue (DB) aerosol products, assuming constant coefficients representative of barren soils and a fixed geometric factor (AMF) equal to 2.8 (Sayer et al., 2013~~; Gkikas et al., 2021~~). The absolute uncertainty of the DT component is expressed as:

$$\sigma_{\mathrm{DT}} = 0.15 \cdot \mathrm{DOD}_{\mathrm{MIDAS}}\mathrm{DOD} + 0.05, \quad (5)$$

w~~W~~hile the corresponding DB uncertainty is given by:

$$\sigma_{DB} = \frac{a + b \cdot DOD_{MIDAS}}{AMF}, \quad (6)$$

where a and b are empirical coefficients that depend on the surface type and AMF is the geometric airmass factor. In this study, since our analysis is performed over the major deserts of the planet (see Fig. 1), constant values representative of barren soils are adopted for a and b, equal to 0.12 and 0.61, respectively, following Gkikas et al. (2021).

For the merged MIDAS product, the total absolute uncertainty is obtained from the quadrature sum of the DT and DB components:

$$\sigma^{DOD}_{MIDAS} = \frac{1}{2}\sqrt{\sigma^2_{DT} + \sigma^2_{DB}}. \quad (7)$$

Finally, the relative MIDAS DOD uncertainty is computed as:

$$\sigma^{rel}_{MIDAS} = \frac{\sigma^{DOD}_{MIDAS}}{\sqrt{N} \cdot DOD_{MIDAS}}, \quad (8)$$

where N is the number of 1º × ~~x~~1º MIDAS grids within each 2º × ~~x~~5º predefined grid, fulfilling the criteria discussed ~~in~~at the ~~previous~~beginning of this section.

For POLDER-3/GRASP, the relative DOD uncertainty is estimated following the same general framework adopted for MIDAS (Gkikas et al., 2021). Different empirical coefficients are employed, following Zhang et al. (2021), with a =0.008 and b =0.892, to account for the specific characteristics of the POLDER-3/GRASP product. In addition, a constant AMF equal to 2.92 is adopted, based on an independent analysis of POLDER viewing geometries derived from a one-year dataset over 19 AERONET stations (Fig. S2).

As an example, the relative DOD uncertainties for the CALIOP–MIDAS synergy are presented in Fig. 4. The red dashed vertical line indicates the relative uncertainty threshold value of 0.5 used for the selection of reliable DOD retrievals. This threshold was selected ~~in order~~ to retain a statistically significant number of cases for the derivation of the dust LRs using the methodology presented in the following section. Additionally, the relative uncertainties for the CALIOP-POLDER-3/GRASP synergy are presented in Fig. S3.

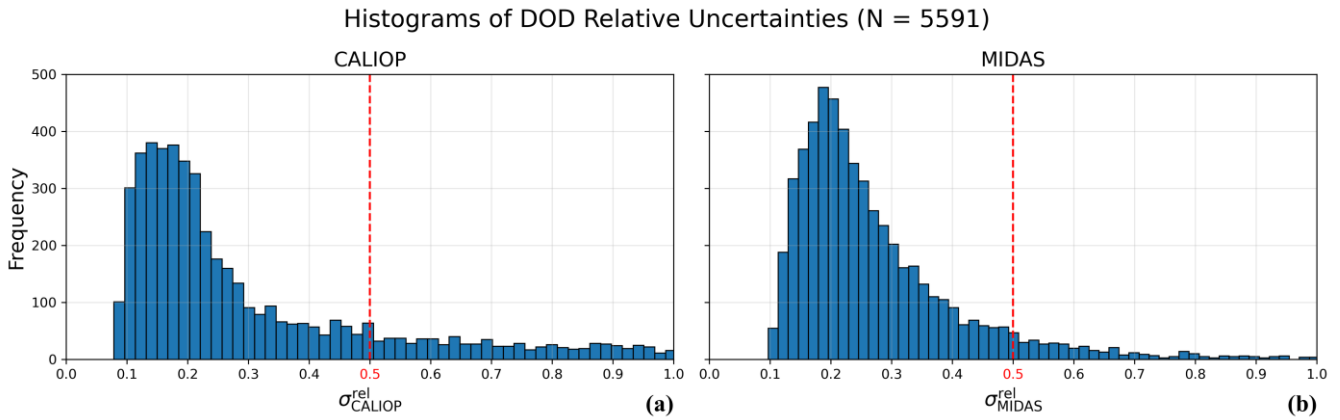

Figure 4: Histograms of the relative dust optical depth (DOD) uncertainties for (a) CALIOP (σ^{rel}_{CALIOP}) and (b) MIDAS (σ^{rel}_{MIDAS}) for the total 5,591 dust cases identified over North Africa and the Middle East. The red vertical dashed line indicates the relative uncertainty threshold value of 0.5 used for the selection of reliable DOD retrievals.

3.3 Dust lidar ratio retrieval method

The calculation of dust LR is based on minimizing the Y function of Eq. (S2.14) of the Supplement, also introduced here as Eq. (9). We note that the parameters in Eq. (9) differ from those in the Supplement because in our study the formulation is specialized to dust-only cases and to the CALIOP-MIDAS and CALIOP-POLDER-3/GRASP synergies. The general formulation presented in the Supplement, however, remains applicable to other aerosol species and datasets. The Eq. (9) is modified as follows:

$$Y=\left|\mathrm{DOD_{CALIOP}}-\mathrm{LR^{d}_{CALIOP}}\int_{z_o}^{z_G}\left\{\frac{\left(\frac{\alpha_d}{\mathrm{LR^{d}_{eff}}}+\beta_m\right)\exp\left[-2\int_{z_o}^{z}\left(\alpha_d+\mathrm{LR^{d}_{CALIOP}}\beta_m\right)d\zeta\right]}{1-2\mathrm{LR^{d}_{CALIOP}}\int_{z_o}^{z}\left(\frac{\alpha_p}{\mathrm{LR^{d}_{eff}}}+\beta_m\right)\exp\left[-2\int_{z_o}^{\zeta}\left(\alpha_d+\mathrm{LR^{d}_{CALIOP}}\right)d\zeta'\right]d\zeta}-\beta_m\right\}dz\right| \quad (9)$$

Here, the parameter z is the range from the spaceborne lidar, ζ and ζ' are both surrogate variables representing different instances of range in the nested integrals, z_o is the reference (aerosol free) range, z_G is the ground range, β_m is the vertically resolved molecular backscatter coefficient, a_d is the particle extinction coefficient, LR^{d}_{CALIOP} is the constant dust LR (i.e., 44 sr - Kim et al., 2018), LR^{d}_{eff} is the effective columnar dust LR, and DOD_{CALIOP} is the CALIOP DOD. The z reference system is discussed in the Supplement.

To minimize the function Y we try different LR^{d}_{eff} values and select the one that results to the Y value closest to zero. As discussed in Section 2.1, the pressure and temperature profiles within CALIPSO dataset are used for the calculation of β_m. The dust extinction coefficient (a_d) is not available from MIDAS or POLDER-3/GRASP; however, the CALIOP extinction profile (a^{d}_{CALIOP}) can be scaled using the reference DOD_i (where i denotes either MIDAS or POLDER-3/GRASP) and used as a priori extinction information. The errors introduced by this assumption are discussed in Section 3.3.1. The following physical constraints have been applied for the inversion:

(i) The values of LR^{d}_{eff} are restricted to the range of 20-68 sr. This range represents ±24 sr around the constant dust LR of 44 sr used within CALIPSO algorithm (Kim et al., 2018). Moreover, this range encompasses dust LRs reported in in previous studies, including 53.1 ± 7.9 sr for Saharan dust and 37.4 ± 5.3 sr for Middle Eastern dust, as summarized in Floutsi et al. (2023),

(ii) the LR^{d}_{eff} values which cause the denominator of Eq. (9) to become lower than 0.01 are automatically rejected. Such LR^{d}_{eff} values would lead to parts of the a^{d}_{CALIOP} and $\beta^{d}_{\mathrm{CALIOP}}$ profiles approaching infinity or becoming negative, which were never observed in our CALIPSO dataset, and

(iii) the Y minimum must be smaller than 0.01 to guarantee that it is sufficiently close to zero.

The second and third constraint become more important when random uncertainty of the retrieval is considered (see Section 3.3.2).

3.3.1 Systematic uncertainty of the lidar ratio retrieval

The systematic uncertainty introduced from the retrieval of LR^{d}_{eff} has been evaluated using synthetic β_{d} and α_{d} profiles whose dust lidar ratio LR_{d} was assumed to be constant with height. The LR_{d} and DOD_{i} were assumed to range between 20 and 68 sr and between 0.1 and 1, respectively. We did not consider testing the function outside the 20–68 sr range, as such values deviate substantially from the reference LR^{d}_{CALIOP} of 44 sr commonly used in the Klett retrieval (Kim et al., 2018) and from dust LR values reported in the literature (Floutsi et al., 2023).We also did not consider DOD values higher than 1 because they rarely appear in our datasets. For the simulation of the molecular backscatter β_{m}, pressure and temperature profiles generated by the U.S. Standard Atmosphere (1976) were applied. Those α_{d} and β_{m} profiles were used to simulate the range-corrected lidar signal that a satellite lidar would measure and to simulate the corresponding $\beta^{d}_{\mathrm{CALIOP}}$ and DOD_{CALIOP} when the forward Klett inversion is applied. Then, considering α_{d} and β_{m} to be known, Eq. (9) was used to retrieve the effective columnar dust lidar ratio $LR_{\mathrm{d,eff}}$. The systematic bias is calculated from the difference between LR_{d} and LR^{d}_{eff}. It was found that if α_{d} and β_{m} are accurately known, the retrieval uncertainty of LR^{d}_{eff} is also very accurate, with a systematic bias less than 0.1 sr. This check was done to ensure the overall validity of Eq (9).

Our application, however, is not so simple as only the biased Klett extinction coefficient profile a^{d}_{CALIOP} is available in the CALIPSO dataset. We have examined how accurately can LR^{d}_{eff} be retrieved when applying a^{d}_{CALIOP} scaled with DOD_{i} instead of α_{d} as a priori extinction profile to function Y. We have seen that this is a much better approximation than using no a priori information on the aerosol vertical distribution at all, leading to a systematic bias less than 1 sr for any LR_{d} within 20-68 sr and for any DOD_{i} within 0.1 and 1, which is sufficient for the purposes of this study.

3.3.2 Random uncertainty of the lidar ratio retrieval

The random uncertainty is calculated with a Monte Carlo approach. The input data used for the calculation of LR^{d}_{eff} include: the -a^{d}_{CALIOP}, DOD_{i} (from either MIDAS or POLDER-3/GRASP), and the pressure and temperature profiles provided in the

CALIPSO dataset (as discussed in Section 2.1). The absolute uncertainty of a^{d}_{CALIOP} ($\sigma^{\mathrm{d}}_{\alpha,\mathrm{CALIOP}}$) for each dust case is provided within the LIVAS dataset, while the uncertainty of DOD_{CALIOP} is estimated through Eq. (3); both representing absolute random uncertainties. To assess the random uncertainty $\sigma^{\mathrm{d,eff}}_{\mathrm{LR}}$ of LR^{d}_{eff} we perform 100 Monte Carlo permutations (indicated by index j) assuming that the error distributions of a^{d}_{CALIOP} and DOD_{i} are Gaussian and that $\sigma^{\mathrm{d}}_{a,\mathrm{CALIOP}}$ and σ_i^{DOD} correspond to one standard deviation. The $LR^{d}_{\mathrm{eff,j}}$ that minimizes Y_{j} is calculated for each permutation j. Then, $\sigma^{\mathrm{d,eff}}_{\mathrm{LR}}$ is estimated as the standard deviation of the LR_{eff} error distribution. The physical constraints mentioned early in section 3.3 become important when estimating the random uncertainty because they ensure that no $LR^{d}_{\mathrm{eff,j}}$ without physical meaning participate in the error distribution.

3.3.3 Propagation of grid-cell-level uncertainties

To quantify the uncertainty of the spatiotemporally averaged dust LR, we propagate the grid-cell-level uncertainties through the temporal and spatial averaging steps. Each grid cell may be sampled multiple times by different number of dust cases (selected based on the criteria discussed in Section 3.1), and the uncertainty of the mean dust LR therefore depends both on the uncertainties of the individual cases and on the sampling variability within the grid cell.

Following Gkikas et al. (2022), the uncertainty of the temporally averaged dust LR in grid cell i is computed as:

$$\sigma'_{\mathrm{i}} = \frac{\sqrt{\sum_{\mathrm{k=1}}^{\mathrm{N_i}} \left(\sigma^{\mathrm{d,eff}}_{\mathrm{LR,i,k}}\right)^2}}{\mathrm{N_i}}. \quad (10)$$

In addition, we account for sampling uncertainty using the standard error of the mean (SE):

$$\mathrm{SE_i} = \frac{\mathrm{SD}}{\sqrt{\mathrm{N_i}}}, \quad (11)$$

where SD_i is the standard deviation of the dust LR values from all the dust cases within grid cell i.

The total uncertainty (σ) of gird cell i is then given by:

$$\sigma_{\mathrm{i}} = \sqrt{(\sigma'_{\mathrm{i}})^2 + (\mathrm{SE_i})^2}. \quad (12)$$

Finally, when computing spatial averages at regional scales, we assume that the grid-cell uncertainties are correlated across space. Under this assumption, the uncertainty of a spatially averaged dust LR is obtained by taking the area-weighted mean of the individual grid-cell uncertainties. For a spatial domain j containing N_j grid cells, the corresponding uncertainty is:

$$\sigma_{\mathrm{j}} = \sum_{\mathrm{i=1}}^{\mathrm{N_j}} \mathrm{w_i} \cdot \sigma_{\mathrm{i}}\,, \quad (13)$$

where w_i represents the weight of grid cell i, defined as the fraction of dust observations in grid cell i relative to the total number of dust cases within the region.

3.3 Derivation of dust lidar ratio

The match-up methodology described in the previous paragraph led to 5,591 and 1,817 collocated pairs between CALIOP-MIDAS and CALIOP-POLDER-3/GRASP, respectively. As a first step for the derivation of LR, the DOD differences are computed based on the equation:

$$DOD_{diff,i} = DOD_i - DOD_{CALIPSO} \quad (2)$$

, where *i* refers to MIDAS or to POLDER-3/GRASP, respectively. For the adjustment of LR, the North Africa and Middle East $DOD_{diff,i}$ distributions are filtered separately using the Interquartile Range (IQR) method. This method can be applied to various distributions, from symmetric ones (e.g., normal distribution) to skewed ones, as it focuses on the central 50% of the data and is less influenced by extreme values. The following equation is used for its calculation (Wackerly et al., 2008):

$$IQR = Q3 - Q1 \quad (3)$$

, where the Q1 is the first quartile (25^{th}) and the Q3 is the third quartile (75^{th}). In order to define the outliers, the following equations are used for the lower and upper threshold:

$$\text{lower threshold: } Q1 - 1.5 \cdot IQR \quad (4)$$

$$\text{upper threshold: } Q3 + 1.5 \cdot IQR \quad (5)$$

The IQR method, commonly applied in satellite data processing for robust filtering (Zhang et al., 2019; Bhattarai et al., 2024), is implemented on the DOD_{diff} restricting the adjusted LR values in "reasonable" ranges (53.1 ± 7.9 sr for Saharan dust and 37.4 ± 5.3 for Middle Eastern dust – values summarized in Floutsi et al., 2023), as long as too high or low values of AOD_{diff} could lead to unrealistic LR retrievals. The IQR method yielded a final collection of 5,203 and 1,773 cases over both North Africa and Middle East for the synergy of CALIOP-MIDAS and CALIOP-POLDER-3/GRASP, respectively.

After the filtering of the DOD_{diff}, in order to estimate the dust LR per 2ºx5º grid we want for each of the collocated pairs to adjust the LR in order for the DOD_{CALIOP} to be equal either to DOD_{MIDAS} or to $DOD_{POLDER\text{-}3/GRASP}$, following the equation:

$$LR_{updated,i} = LR_{CALIPSO} \cdot \left(DOD_{diff,i} - 1\right) \quad (6)$$

, where *i* refers either to MIDAS to POLDER-3/GRASP products. The $LR_{CALIPSO}$ represents the default LR value used for dust layers within the CALIPSO algorithm and it is equal to 44 sr (Kim et al., 2018). Higher values than 44 sr are assigned to the dust $LR_{updated}$ if $DOD_{CALIOP} < DOD_{MIDAS\ or\ POLDER\text{-}3/GRASP}$ and lower ones in the opposite case. Finally, for each 2ºx5º grid a mean value for dust LR is computed, along with its standard deviation, while the counts (number of dust cases) used for each grid towards the adjustment of LR are also calculated.

3.4 Evaluation against AERONET

To evaluate the impact of dust LR on CALIOP's columnar DOD retrievals, we first aim to identify dust cases near AERONET stations during the CALIPSO mission, which spans the period from 2006 to 2023. Following Moustaka et al. (2024), we begin by identifying CALIPSO orbits that pass within a 100 km radius of AERONET stations located in the desert domains outlined in Fig. 1a. These stations must have available measurements within a ±30 min window centered on the satellite's overpass

~~time. Along each CALIPSO overpass, we ensure that all the criteria mentioned in Section 3.1 are met. Based on Amiridis et al. (2015), we also require: (i) the difference between the AERONET station elevation and CALIPSO's mean track elevation to be less than 100 m, and (ii) a relatively flat ground (slope less than 400 m) along the satellite overpass. By applying these additional criteria, we minimize DOD biases caused by the different conditions that could be sampled by the ground and satellite based instruments. For the part of the CALIPSO orbits falling inside the 100 km radius around the AERONET station, the respective dust LR values of the 2ºx5º grids around the ground site are applied on the backscatter coefficient retrievals at 532 nm in order to derive the columnar DOD at 532 nm. Under the previous constraints, a total number of 135 dust cases were identified in 9 AERONET stations, most of them over Middle East and the region of Sahel, as presented in Fig. 1b.~~

4 Results

4.1 Examination of DOD retrievals among the A-Train constellation

T~~T~~~~Firstly, we emphasize on the DOD comparison between CALIPSO versus POLDER-3/GRASP and MIDAS after filtering the outliers in the DOD_{diff} distributions and prior the computation of the "updated" dust LRs.~~ he methodology described in Section 3 yielded a ~~collection~~ sample of 2,943 and 1,116 collocated pairs between CALIOP-MIDAS and CALIOP-POLDER-3/GRASP, respectively. In Figure 5~~4~~, we present the box-whisker plots of the DOD_{diff} ~~(~~(defined as DOD_i-DOD_{CALIOP}, where i refers to either MIDAS or POLDER-3/GRASP) (y axis) between the two synergies of CALIOP-POLDER-3/GRASP (Fig. 5~~4~~a) and CALIOP-MIDAS (Fig. 5~~4~~b) divided into 10 equal-sized bins by CALIOP DODs (x axis). The obtained statistics ~~of the linear regression~~ are provided separately for North Africa (yellow color) and Middle East (purple color), including the slope of the linear regression, the Mean Bias Error (MBE), the correlation coefficient (R) and the Root Mean Square Error (RMSE), along with the number of collocated samples per region (counts). Based on the statistics, there is a pronounced underestimation ~~and overestimation~~ of CALIOP DODs over North Africa (MBE equal to 0.07~~286~~ and 0.06~~875~~ for CALIOP-POLDER-3/GRASP and CALIOP-MIDAS synergy, respectively) indicating that higher dust LRs over the region could improve the CALIOP DOD retrievals. Over the~~and~~ Middle East, CALIOP DODs are also underestimated by both synergies; however, the biases are significantly smaller in respect to North Africa (MBE equal to +~~-~~0.007~~21~~ and +0.011~~-0.022~~ for CALIOP-POLDER-3/GRASP and CALIOP-MIDAS synergy, respectively)~~, respectively, indicating that higher dust LRs over North Africa and lower over Middle East could improve the DOD CALIOP retrievals.~~. While the outcome over North Africa is in good agreement with previous studies based on ground-based lidar observations, a contrasting pattern is observed over the Middle East. Earlier studies have demonstrated that dust lidar ratios are systematically different between these two major desert regions due to variations in dust particle mineralogical composition (Müller et al., 2007; Groß et al., 2011; Preißler et al., 2011; Tesche et al., 2009~~a~~, 2011; Kanitz et al., 2013; Baars et al., 2016; Rittmeister et al., 2017; Kaduk, 2017; Haarig et al., 2017a; Urbanneck, 2018; Bohlmann et al., 2018; Filioglou et al., 2020; Szczepanik et al., 2021; Haarig et al., 2022). Based on these studies, lower dust LRs ~~lidar ratios~~ (<44 sr) have generally been proposed over the Middle East, while higher values (>44 sr) have been reported over North Africa. It should be noted, however, that these observations were mostly conducted far

from major dust source regions and for individual dust cases originating from specific source areas. In contrast, our analysis spans a much broader spatial domain, encompassing most of North Africa and the Middle East, and therefore reflects regionally integrated dust conditions rather than isolated source-specific events.

~~While the outcome over North Africa is in agreement with previous studies, relying on ground-based lidar observations, the outcome over the Middle East differ, while they reported that dust LRs between these two major desert regions are different due to the dust particles mineralogy (Müller et al., 2007; Groß et al., 2011; Preißler et al., 2011; Tesche et al., 2009a; 2011; Kanitz et al., 2013; Baars et al., 2016; Rittmeister et al., 2017; Kaduk, 2017; Haarig et al., 2017a; Urbanneck, 2018; Bohlmann et al., 2018; Filioglou et al., 2020; Szczepanik et al., 2021; Haarig et al., 2022). In both synergies, the underestimation over the Middle East becomes more pronounced for higher CALIOP DODs (over Arabian Peninsula), while there is also the need for DOD increment for some smaller to moderate DODs, possibly due to the inclusion of some central Asian deserts (eastern of Caspian Sea) into the domain (Fig. 1a), as noted also by Kim et al. (2020) and discussed in detail in Section 4.2. In contrast, over North Africa, most of the discrepancies on CALIOP DODs are recorded for the smaller to moderate dust loads, while for the CALIOP MIDAS synergy, a slight overestimation is observed for the high DODs, which can be attributed to some sub-Sahel regions (Section 4.2).~~

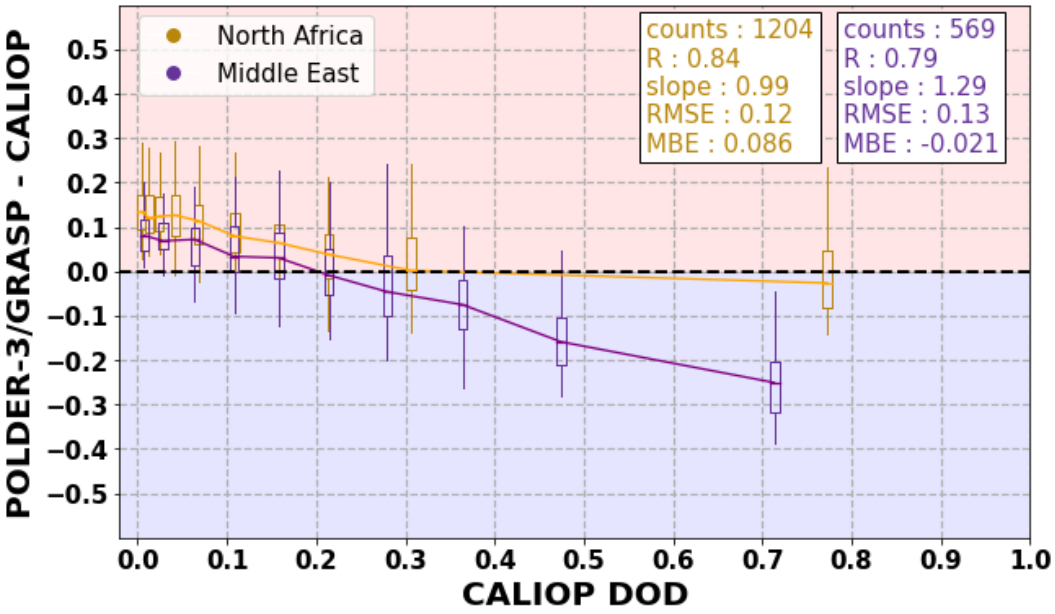
North Africa
Middle East
counts : 1204
R : 0.84
slope : 0.99
RMSE : 0.12
MBE : 0.086
counts : 569
R : 0.79
slope : 1.29
RMSE : 0.13
MBE : -0.021
POLDER-3/GRASP - CALIOP
CALIOP DOD

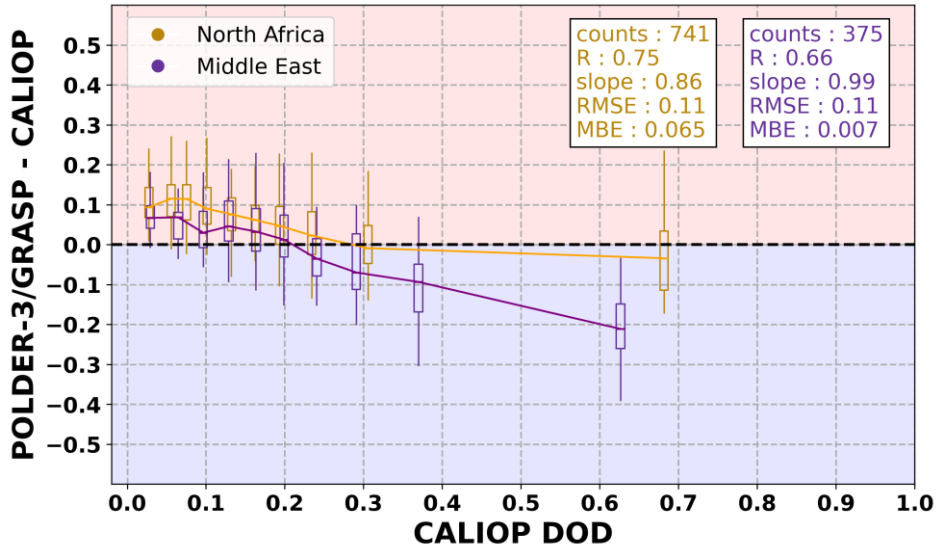
North Africa
Middle East
counts : 741
R : 0.75
slope : 0.86
RMSE : 0.11
MBE : 0.065
counts : 375
R : 0.66
slope : 0.99
RMSE : 0.11
MBE : 0.007
POLDER-3/GRASP - CALIOP
CALIOP DOD

(a)

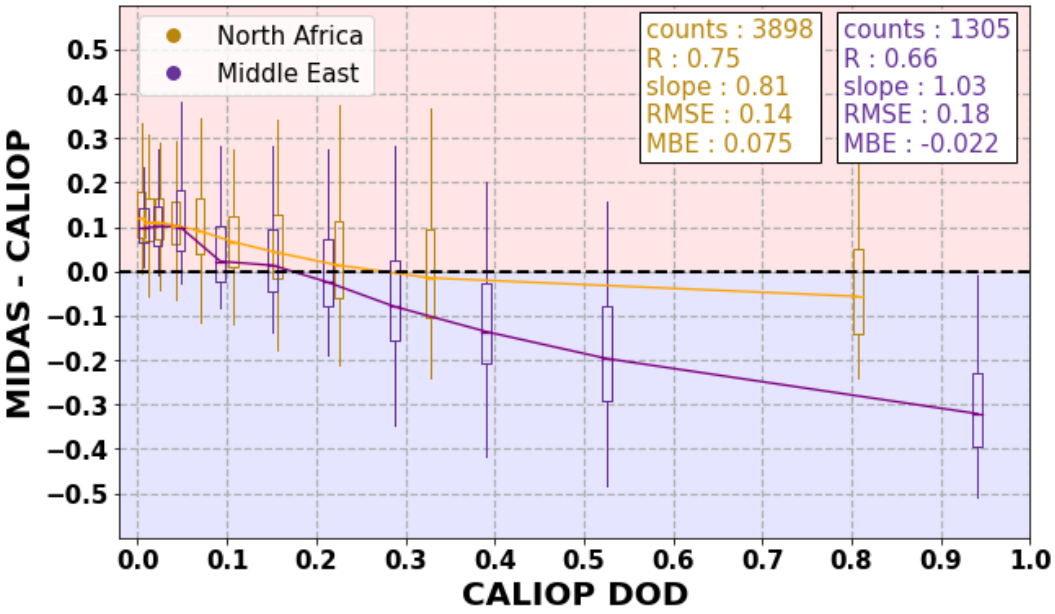

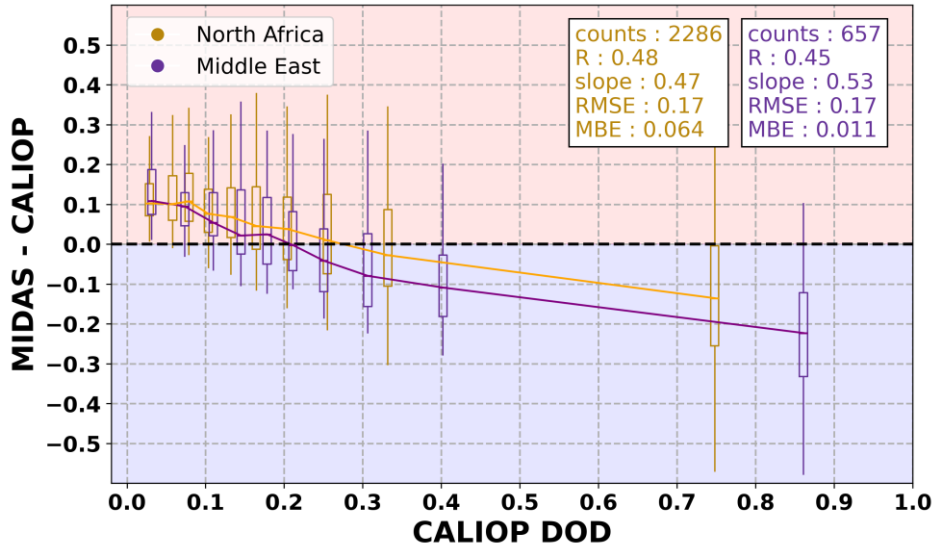

(b)

Figure 54: Box-whisker plots for the dDust oOptical dDepth differences (DOD_{diff}) (y-axis) (displaying the 75/25 percentiles at the boxes, and the median in the center line, while the whiskers are displaying the ±1.5 IQR from the 25/75 percentiles, respectively) between (a) CALIOP – POLDER-3/GRASP and (b) CALIOP-MIDAS, along the CALIOP DODs (x-axis). The yellow boxes are assigned for North Africa, while the purple ones for Middle East. The background color denotes the over-/underestimation (red/blue color). The number of collocated measurements, the correlation coefficient (R), the slope of the linear regression, the Mean Bias Error (MBE), and the Root Mean Square Error (RMSE) scores are provided in the legends separately for North Africa and the Middle East.

4.2 Geographical distribution of the dust lidar ratio

~~The DOD_{diff} in Fig. 4 were used for the adjustment of dust LR following Eq. (6).~~ Following Eq. (9#), a mean dust LR value was computed f~~F~~or each 2º × ~~x~~5º grid over North Africa and Middle East domains (Fig. 1~~a~~) ~~a mean dust LR value was computed~~, along with its ~~standard deviation~~corresponding uncertainty metrics, and the number of the available dust cases~~contributing to the dust LR estimation~~~~used for the LR adjustment~~. The LR geographical distribution of the differences between the upgraded dust LR (obtained via the CALIOP-POLDER-3/GRASP and CALIOP-MIDAS synergies, respectively) and the default value (44 sr) assigned to dust aerosols in the CALIPSO retrieval algorithm were also estimated. For the 10-year period of the CALIOP-MIDAS synergy, both annual and seasonal LR maps were produced.~~-~~ The corresponding dust LR maps and their uncertainties derived from the CALIOP–POLDER-3/GRASP synergy are also provided in the Supplement (Figs. S4–S5). However, due to the much shorter period of CALIPSO-PARASOL satellites coincidence (2006–2009) and the substantially smaller number of available dust cases (1,116 instead of 2,943 for CALIOP–MIDAS), these maps are not analysed in detail here. Their use is limited to the regional LR assessment in Sect. ~~4.~~35, where the number of coincident retrievals within each predefined region remains relatively sufficient to derive meaningful statistics.~~In contrast, for the CALIOP-POLDER-3/GRASP synergy, only annual LR maps could be generated due to the significantly shorter period of coincident retrievals between the PARASOL and CALIPSO satellites (1,773 instead of 5,203).~~

In Fig.~~.~~ ~~6~~5~~a~~, the mean dust LR map from the CALIOP-MIDAS synergy is illustrated. Dust LRs are maximized (up to ~56 sr) over or near the strongest dust source globally (Washington et al., 2009; Ginoux et al., 2012), namely the Bodélé Depression in the northern Chad basin. Other North African desert regions yielding high dust LRs include the Grand Elg of Bilma and the basin of the Aïr (both over Niger), the Libyan desert, and regions in Sudan. On the western side of North Africa, notable areas are the Erg El Djouf (over Mali and Mauritania) and the Grand Erg Occidental (over Algeria), all characterized by LR values mostly in the range of 47–52 sr. Even in the absence of ground-based dust LR measurements over the central Sahara and the major Saharan source regions (e.g., Bodélé), campaign-based studies, such as SAMUM-1/2 (Ansmann et al., 2011) and SALTRACE (Weinzierl et al., 2017), investigating the optical and microphysical properties of North African dust after short- and long-range transport~~, such as SAMUM-1/2 (Ansmann et al., 2011) and SALTRACE (Weinzierl et al., 2017),~~ reported LR values of 53.1 ± 7.9 sr, which fall well within the range of our CALIOP–MIDAS dust LR estimates. Across the Arabian Peninsula, the retrieved dust LR values exhibit pronounced spatial variability, with lower values (~38–45 sr) mainly in the central and southern parts, and locally higher values (~46–54 sr) toward the northern Arabian Peninsula and Mesopotamia. Overall, these values show regional agreement with ground-based lidar observations over the Arabian Peninsula, which reported dust LR values of 37.4 ± 5.3 sr (Müller et al., 2007; Kaduk, 2017; Urbanneck, 2018; Filioglou et al., 2020; Floutsi et al., 2023); however, not all retrieved dust LRs fall strictly within this literature-based range, particularly over the northern part of the region. Over the Central Asian deserts (Karakum and Kyzylkum), LR values typically range between ~47 and 56 sr. This region is considered relatively understudied in terms of dust LR, with the only available ground-based constraints provided by Hofer et al. (2020), who reported values in the range of ~35–40 sr over Dushanbe (Tajikistan) in the framework

of the CADEX (Central Asian Dust Experiment) campaign (Althausen et al., 2019). Notably, one of our closest retrieved CALIOP–MIDAS dust LR values over this region is ~36 sr, which agrees remarkably well with these ground-based observations. At the same time, our analysis also reveals locally higher LR values across parts of Central Asia, which is consistent with the findings of Kim et al. (2020), who retrieved dust lidar ratios over the region using a synergistic CALIPSO–MODIS approach over a 5-year period.

The robustness of LR spatial patterns is supported by the number of collocated CALIOP–MIDAS dust cases per grid (Fig. 6~~5~~b), which shows that most of North Africa and large parts of the Middle East are characterized by moderate to high sampling densities, frequently exceeding 20–40 cases per grid and locally reaching even higher values over the major dust sources of North Africa. This confirms that the derived dust LR values are not driven by isolated events but reflect climatologically persistent dust conditions (a conclusion further supported by the uncertainty analysis discussed below- see Fig. 7). In contrast, marginal sampling is mainly confined to peripheral regions, such as the Horn of Africa and parts of South and Central Asia, where the number of available dust cases is limited.

The spatial distribution of the LR deviations relative to the CALIOP default dust lidar ratio of 44 sr (ΔLR; Fig. 6~~5~~c) provides direct insight into the regional adequacy of the fixed-LR assumption. Over most of North Africa, ΔLR is systematically positive, frequently exceeding +5 to +6 sr and locally over +10–12 sr over the Bodélé Depression and parts of the Libyan desert. This demonstrates that the default CALIOP dust LR of 44 sr systematically underestimates the effective dust LR over the major Saharan dust sources. This finding is fully consistent with the positive CALIOP DOD biases identified earlier (Fig. 5~~4~~b) and supports the use of higher LR values over North Africa. In contrast, over large parts of the Arabian Desert, ΔLR is negative, with typical values ranging between ~~-~~2 and ~~-~~6 sr over the Arabian Peninsula and locally reaching ~~-~~8 to ~~-~~10 sr over parts of Iran and Afghanistan. Significant local reversals of this pattern are, however, observed over Mesopotamia and the Central Asian deserts, where positive ΔLR values reach up to approximately +16 sr.

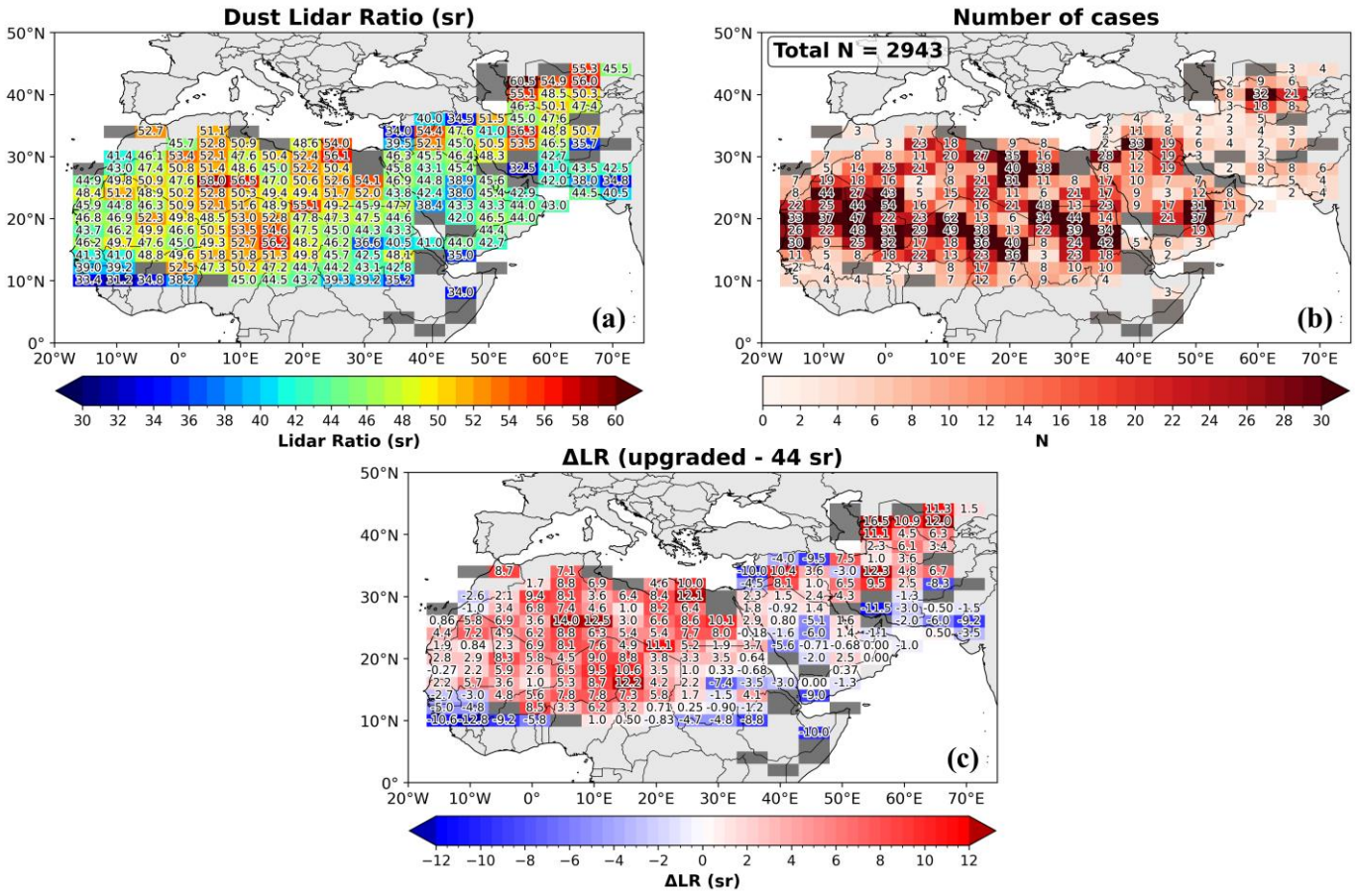
CALIOP-MIDAS — [2007-2017]
Dust Lidar Ratio (sr), Number of cases, ΔLR (upgraded - 44 sr)
Dust Lidar Ratio (sr)
Number of cases
Total N = 2943
ΔLR (upgraded - 44 sr)
(a)
(b)
(c)
Lidar Ratio (sr)
N
ΔLR (sr)

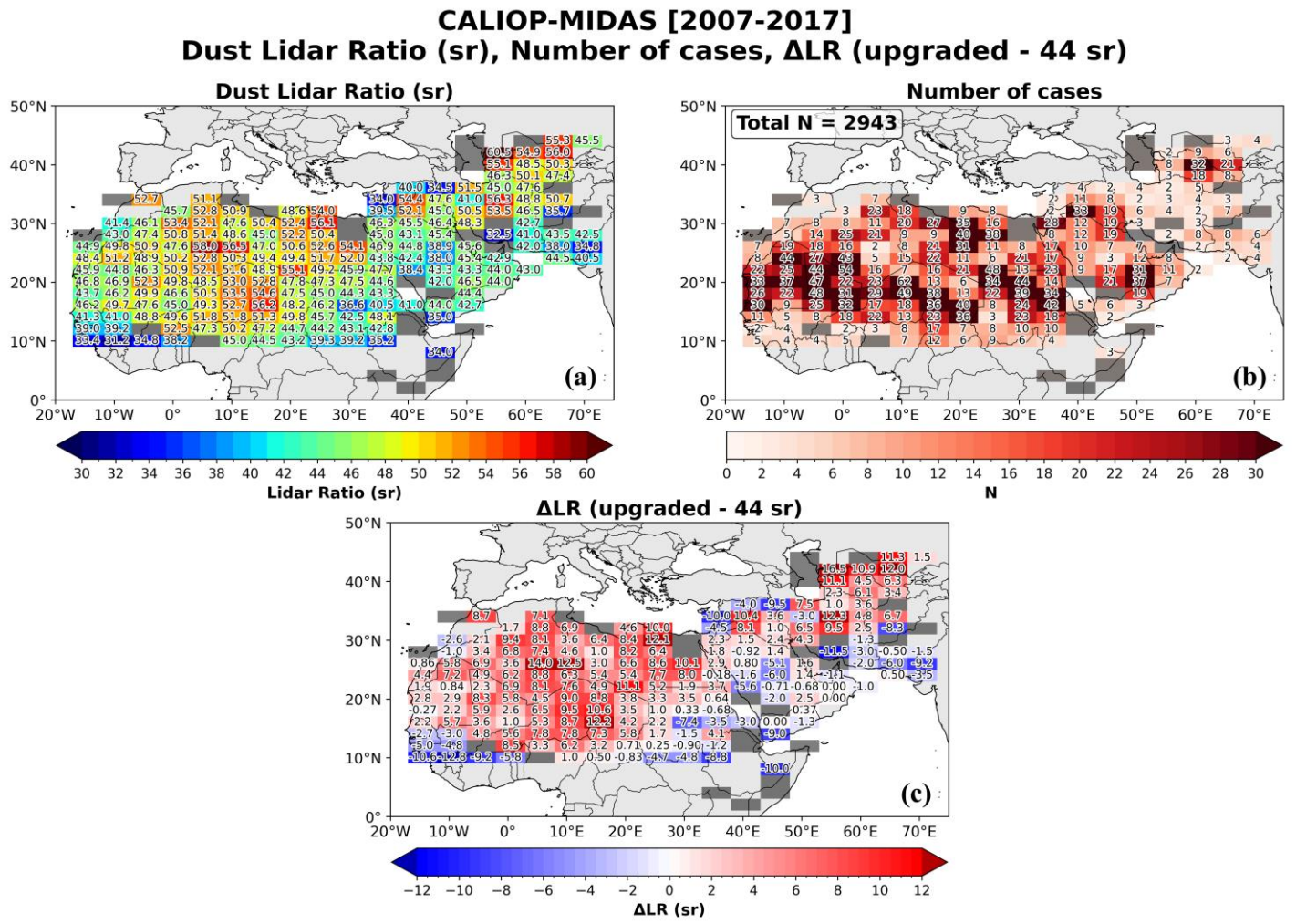

Figure 6~~5~~: Geographical distribution of (a) the mean dust Lidar Ratio (LR), (b) the number of dust cases (N), and (c) the departures of the updated dust LR from the default value of 44 sr used in the CALIPSO retrieval algorithm, all derived from the CALIOP–MIDAS synergy for the period 2007–2017. The values are computed at each 2° × ~~x~~5° predefined grid. Grey-shaded grid cells indicate regions with only one available dust case, for which no robust LR estimate is provided.

~~Figure 5: Geographical distribution of (a) the mean dust Lidar Ratio (LR), (b) the number of dust cases (N), and (c) the departures of the updated dust LR from the default value of 44 sr used in the CALIPSO retrieval algorithm, all derived from the CALIOP–MIDAS synergy for the period 2007–2017. The values are computed at each 2°x5° predefined grid. Grey-shaded grid cells indicate regions with only one available dust case, for which no robust LR estimate can be provided.~~ The spatial distribution of the dust LR uncertainties (Fig. 7~~6~~) reveals that the LR retrieval uncertainty σ′ (Fig. 7~~6~~a) is the dominant contributor to the total uncertainty across most regions. Over the Central Sahara and Central Asian domains, σ′ generally ranges between ~2 and 5 sr, leading to similarly low total uncertainties in Fig. 7~~6~~c. In these regions, the standard error (SE; Fig. 7~~6~~b) remains comparatively small, reflecting both limited ~~day-to-day~~case-by-case variability and the sufficient ~~ly large~~

number of dust cases (Fig. 65b) used to derive the mean LR values. In contrast, the highest total uncertainties, locally reaching ~8–11 sr (Fig. 76c), are observed over parts of the Central Asia (e.g., Iran). In these regions, the elevated total uncertainty primarily originates from the increased σ′ values (Fig. 76a), indicating substantial retrieval uncertainty in the individual LR estimates. The SE component (Fig. 76b) also becomes significant in areas where only a few dust cases are available (e.g., 2–3 cases over parts of Iran), which inflates the sampling-related uncertainty and contributes to the elevated total uncertainty. The enhanced uncertainties over distinct parts of the Middle East may reflect the convergence of dust plumes from Saharan and Central Asian source regions (Rezazadeh et al., 2013; Al-Hemoud et al., 2022; Gkikas et al., 2022), which promotes mixing between mineralogically distinct dust types with different intrinsic lidar ratios (Caquineau et al., 2002; Scheuvens et al., 2013; Ahmady-Birgani et al., 2019). Additionally, potential aerosol-type misclassification in the CALIPSO retrievals may contribute to the observed spread in LR, while over the Sahel some misclassified smoke layers transported from Central African biomass-burning regions (Groß et al., 2011) may further enhance variability.

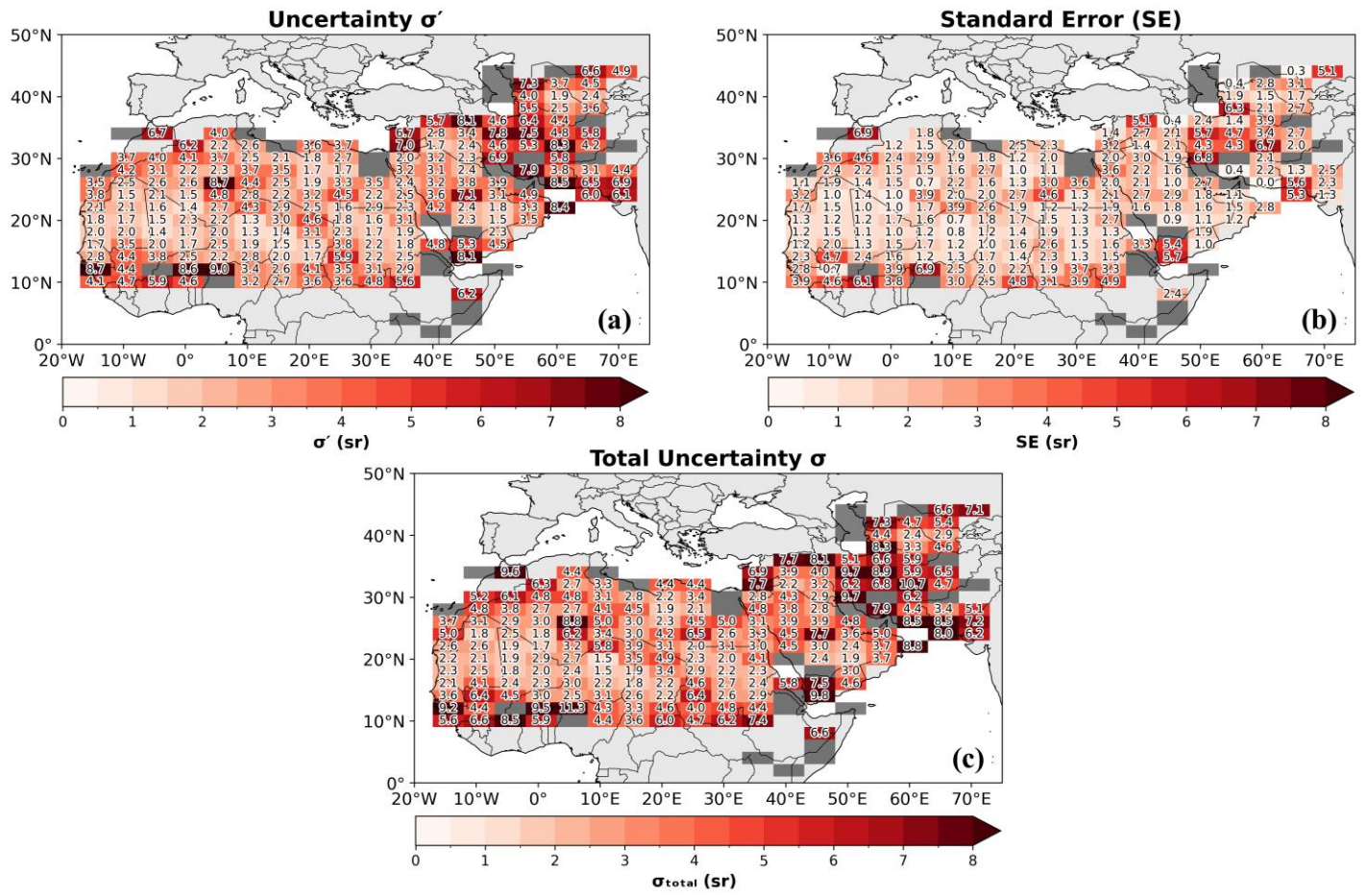
CALIOP-MIDAS [2007-2017]
Dust Lidar Ratio Uncertainties: σ′, SE, and σtotal
Uncertainty σ′
Standard Error (SE)
Total Uncertainty σ
(a)
(b)
(c)
σ′ (sr)
SE (sr)
σtotal (sr)

665

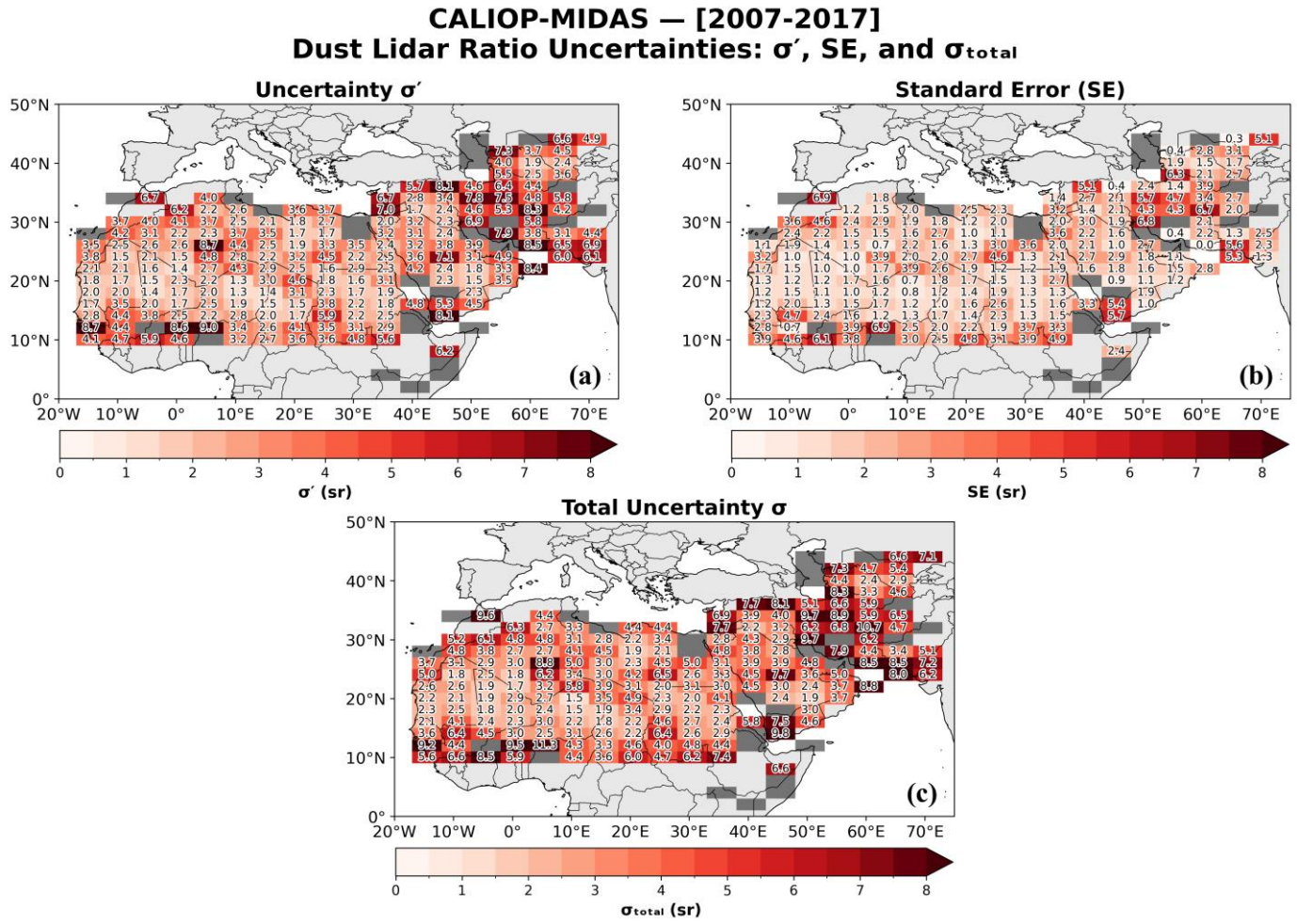

Figure 7~~6~~: Geographical distribution of (a) the LR retrieval uncertainty σ′, (b) the standard error (SE) associated with the case-to-case variability of LR, and (c) the total LR uncertainty σ_{total}, all derived from the CALIOP–MIDAS synergy for the period 2007–2017. The values are computed at each 2° × 5° predefined grid. Grey-shaded grid cells indicate regions with only one available dust case, for which no robust LR estimate is provided.

~~In Fig. 5, the mean dust LR map from the CALIOP-POLDER-3/GRASP synergy is illustrated. Dust LRs are maximized (up to ~53 sr) over or near the strongest dust source globally (Washington et al., 2009; Ginoux et al., 2012), namely the Bodélé Depression in the northern Chad basin. Other North African desert regions yielding high dust LRs include the Grand Erg of Bilma and the basin of the Aïr (both over Niger), the Libyan desert, and regions in Sudan. On the western side of North Africa, notable areas are the Erg El Djouf (over Mali and Mauritania) and the Grand Erg Occidental (over Algeria), all characterized by LR values mostly in the range of 47–52 sr. Over the Arabian Peninsula, our results agree well with the dust LR range (37.4 ± 5.3 sr) obtained from ground-based lidar measurements (Müller et al., 2007; Kaduk, 2017; Urbanneck, 2018; Filioglou et al., 2020; Floutsi et al., 2023). Even in the absence of dust LR values from ground-based measurements in the literature reported for the central Sahara, and over the major dust sources (e.g. Bodélé), the values reported in the literature (53.1 ± 7.9 sr) from~~

~~campaigns (SAMUM 1,2 – Ansmann et al. (2011); SALTRACE – Weinzierl et al. (2017)) studying the optical and microphysical properties of dust particles originating from North Africa after short- and long-range transport are within the range of our CALIOP-POLDER-3/GRASP dust LRs. The regions over the Karakum and Kyzyllkum deserts (central Asia) can be considered as a "blind" spot for dust LR, while the only study in the literature from Hofer et al. (2020) reported values in the range of 35-40 sr over Dushande (Tajikistan) in the framework of the CADEX (Central Asian Dust EXperiment) campaign (Althausen et al., 2019). Additionally, according to the Fig. S1 and S2, most of the dust LR values are characterized by low standard deviation values (mainly less than 5 sr) and a sufficient number of cases, while over the Arabian Peninsula, the standard deviations are higher comparable to the ones over the North Africa (principally in the range of 5-7 sr) even for a significant number of dust cases. This is possibly attributed to either the transport of dust burdens from the Saharan and Central Asian regions (Rezazadeh et al., 2013; Al-Hemoud et al., 2022; Gkikas et al., 2022), leading to a mixing of dust particles with higher and lower LR values (different mineralogy – Caquineau et al., 2002; Scheuvens et al., 2013; Ahmady-Birgani et al., 2019) or to misclassification issues in CALIPSO aerosol subtype product with some aerosol layers erroneously classified as dust. In the same manner, regions over the Sahel, could include some misclassified smoke layers from fires over Central African, with the plumes generally moving towards northern African regions (i.e. the Sahel, sub-Sahel and the Guinea Gulf) (Groβ et al., 2011).~~

~~In Fig. 6, the mean dust LR map from the synergy CALIOP-MIDAS is presented. Similar to the CALIOP-POLDER-3/GRASP synergy, higher values are observed over North Africa, while the incorporation of MIDAS yields higher values of LR in the desert regions over the central part of Asia (around Karakum Desert of Turkmenistan and the Kyzyllkum Desert of Uzbekistan and Kazakhstan in the range of 47-55 sr). Except this evident difference between the two synergies, the LR pattern remains almost the same over the North Africa and in the Arabian Peninsula. The Bodélé Depression and the Grand Erg of Bilma once again are characterized by the highest dust LR values (up to 53.4 sr), followed by the Libyan Desert and certain regions in the western part of the Sahara, with values ranging from 48 to 52 sr. Even if the number of cases for the adjustment of dust LR are significantly increased (Fig. S5) for the CALIOP-MIDAS synergy, due to the 10-year period of collocated measurements, the standard deviations (Fig. S4) are of the same magnitude with the CALIOP and POLDER-3 synergy, with lower values over North Africa and central parts of Asia and higher values over the Arabian Peninsula~~

The seasonal dust LR maps derived from the CALIOP–MIDAS synergy (Fig. ~~8~~7) exhibit a broadly consistent spatial pattern throughout the year, with limited seasonal variability over most desert regions. In all seasons, the highest LR values (~52–60 sr) occur primarily over the Bodélé Depression and the Libyan Desert, two of the most intense and persistent dust sources of North Africa (Ginoux et al., 2012). Moderate LR values (~44–50 sr) dominate the remaining Saharan belt, the Central Asia and distinct regions of Arabian Peninsula, while the lowest values (~38–44 sr) appear over central parts of Arabian Peninsula and Sahel.

Despite the overall spatial stability, subtle seasonal differences are detected. During JJA, slightly enhanced LR values appear over parts of North Africa, consistent with the stronger dust mobilisation and long-range transport that characterise the summer period. Under the prevalence of strong surface winds and low-level jet streams, dust production and export from major source

regions intensify (Al-Hemoud et al., 2022; Gkikas et al., 2022). Conversely, during DJF, dust production diminishes, with the dust LR hotspots restricted mainly over the major dust sources. During MAM and SON, the LR distribution shows a transitional pattern between the more active (JJA) and the less active seasons (DJF) for dust emission and transport. Moreover, the seasonal spatial patterns of dust LR deviations from the CALIOP default dust value of 44 sr (ΔLR; Fig. S6~~6~~) offer direct insight into the regional validity of the fixed-LR assumption. The corresponding distributions of the seasonal uncertainties and the number of dust cases over each predefined grid (Figs. S7~~7~~—S11~~8~~) indicate that the magnitude of the seasonal LR uncertainties is largely controlled by the number of available CALIOP–MIDAS samples. Larger uncertainties appear in regions where only a few dust cases are available, while areas with more frequent dust detection—especially over the central Sahara—display lower uncertainties.

Overall, the combined analysis of the annual and seasonal dust LR maps, together with the corresponding number of cases, uncertainty estimates, and deviations from the default CALIOP dust LR (44 sr), shows that the regional variability of the dust LR is both statistically robust and physically consistent. The spatial patterns identified across North Africa, the Arabian Peninsula, and Central Asia highlight that dust optical properties differ substantially between major source regions and transport pathways. These synergistic satellite-based findings, together with ground-based lidar observations showing similar regional variability in dust lidar ratio (Müller et al., 2007; Groß et al., 2011; Preißler et al., 2011; Tesche et al., 2009, 2011; Kanitz et al., 2013; Baars et al., 2016; Rittmeister et al., 2017; Kaduk, 2017; Haarig et al., 2017a; Urbanneck, 2018; Bohlmann et al., 2018; Filioglou et al., 2020; Szczepanik et al., 2021; Haarig et al., 2022), provide strong support that the assumption of a globally constant dust LR of 44 sr is inadequate for representing the true spatial variability of dust optical properties. Instead, a regionally varying dust LR is required to achieve more accurate CALIOP-based dust retrievals.

~~For the synergy of CALIOP-MIDAS, the seasonal dust LR maps, their standard deviations, along with the number of cases per 2°x5° predefined grid are also presented in Fig. 7 and Fig. S7-8. During JJA, the LR distribution is characterized by the most fragmented pattern, with the highest dust LR values scattered across the desert belt extending from the western part of North Africa and the Arabian Peninsula to Central Asia. Under the prevalence of strong surface winds and low-level jet streams, dust production and transport from the most well-known dust sources is intensified (Al-Hemoud et al., 2022; Gkikas et al., 2022). Conversely, during DJF, dust production diminishes, with the dust LR hotspots restricted mainly over the major dust sources. During MAM and SON, the LR distribution hasshows a transitional pattern between the more active (JJA) and the less active seasons (DJF) for dust emission and transport. According to the seasonal standard deviation of dust LR (Fig. S7), the higher values are confined to the Middle East. These elevated values can be partly attributed to misclassification issues in the CALIPSO aerosol classification scheme. This is because the region is significantly contaminated with aerosol types originating primarily from anthropogenic sources over the Arabian Peninsula. The CALIOP algorithm has difficulty distinguishing pure dust from mixtures of dust with smoke or pollution, particularly when the mixture's higher depolarizing nature is predominantly driven by dust particles. However, the significantly lower variability of dust LR over the Middle East during the DJF underscores the importance of dust transport from adjacent sources, particularly from Sudan, during the summer~~

~~months. This transport is influenced by prevailing wind patterns, such as northeasterlies and northwesterlies, which carry a substantial load of dust layers into the Middle East (Rezazadeh et al., 2013).~~

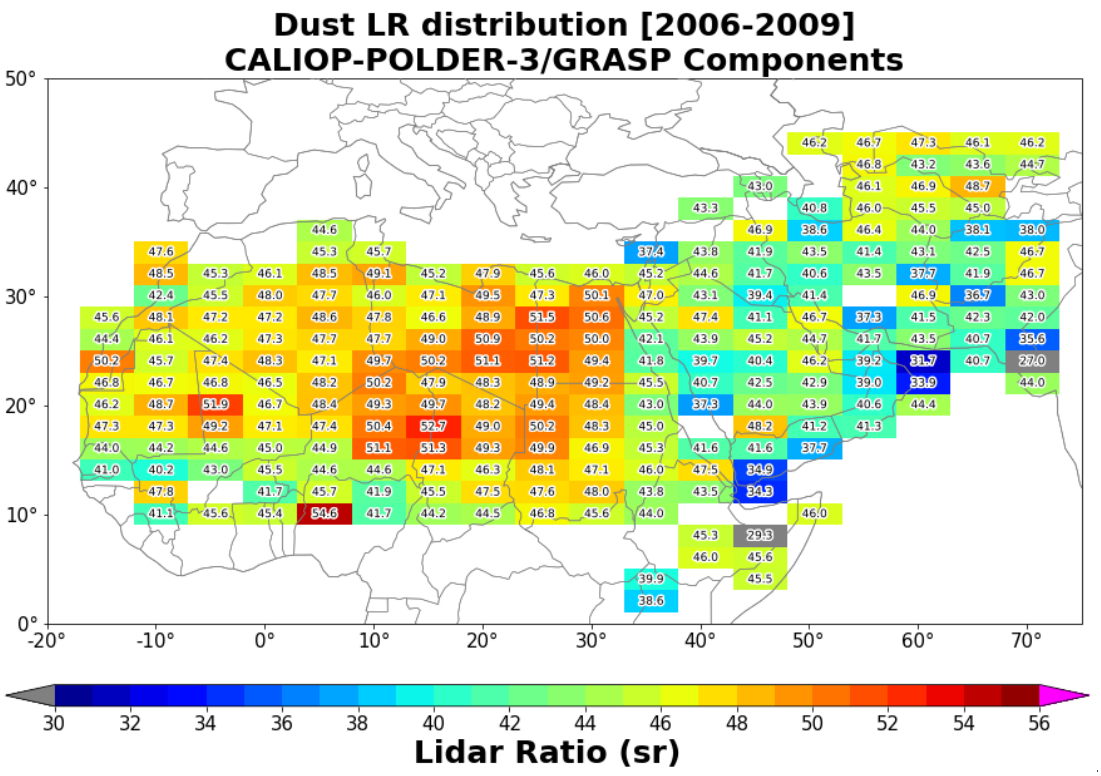
Dust LR distribution [2006-2009]
CALIOP-POLDER-3/GRASP Components
50°
40°
30°
20°
10°
0°
-20°
-10°
0°
10°
20°
30°
40°
50°
60°
70°
30
32
34
36
38
40
42
44
46
48
50
52
54
56
Lidar Ratio (sr)

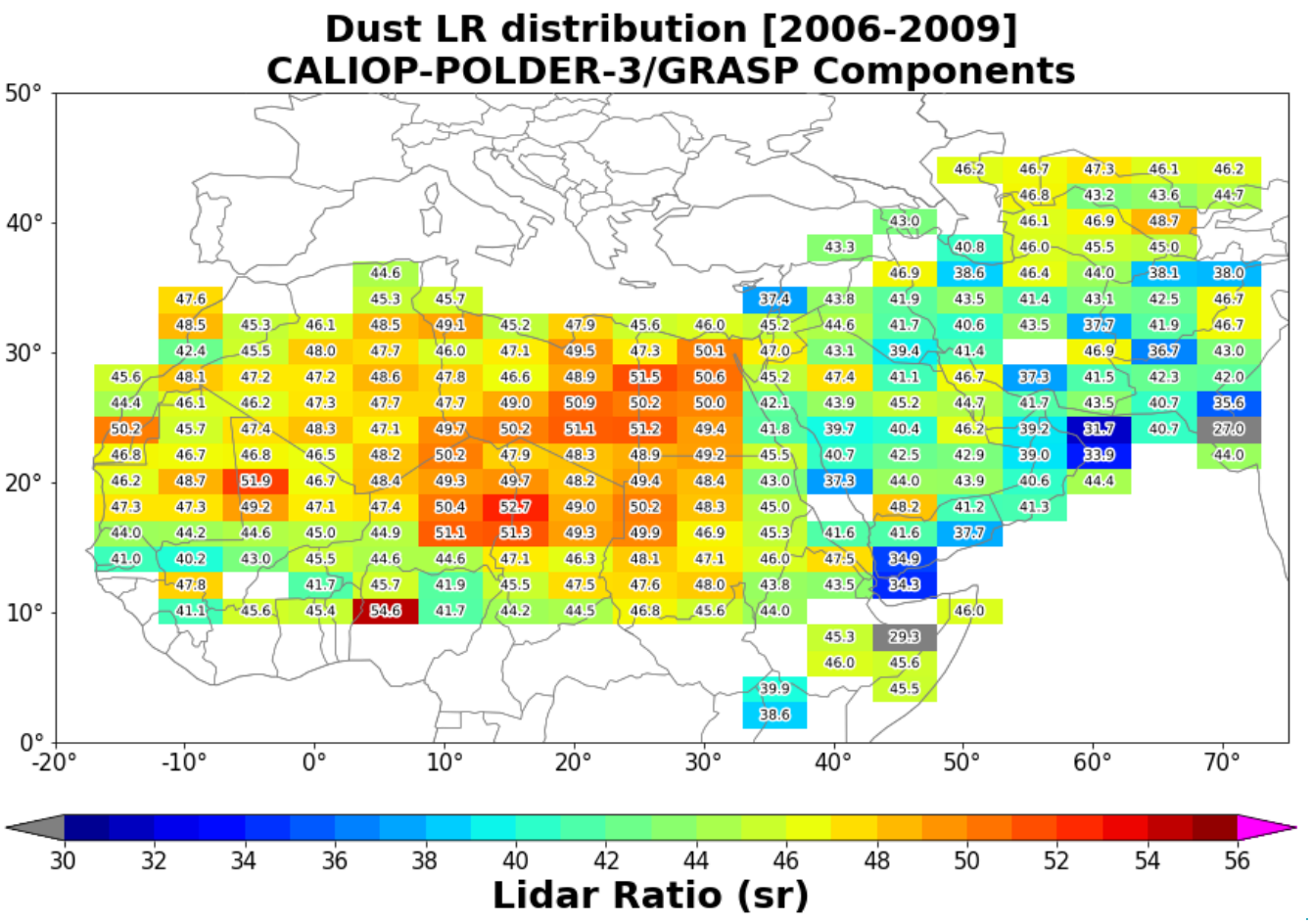
Dust LR distribution [2006-2009]
CALIOP-POLDER-3/GRASP Components
50°
40°
30°
20°
10°
0°
-20°
-10°
0°
10°
20°
30°
40°
50°
60°
70°
30
32
34
36
38
40
42
44
46
48
50
52
54
56
Lidar Ratio (sr)

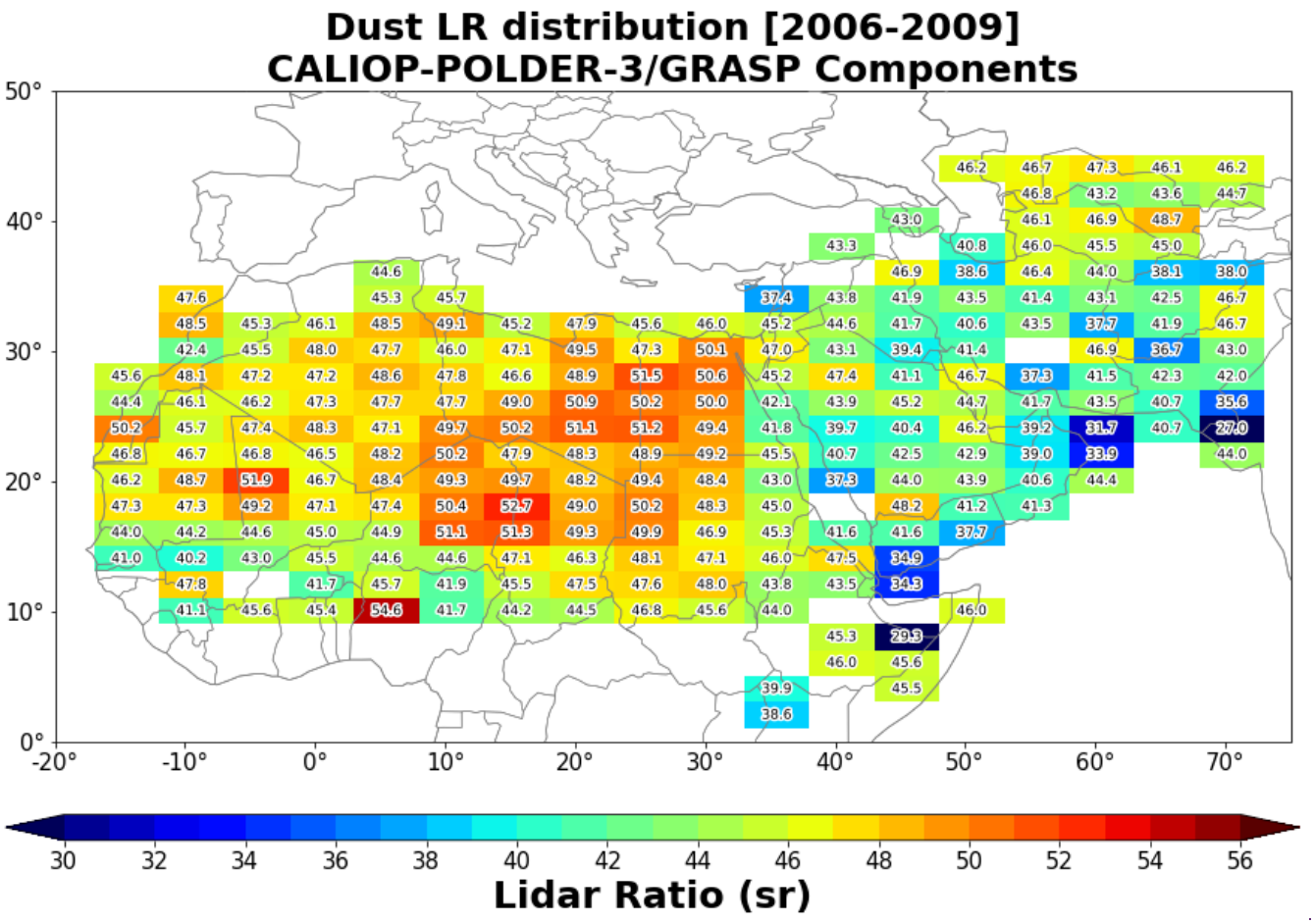

~~**Figure 5: The spatial variability of dust Lidar Ratio (LR) based on the synergy of CALIOP and POLDER-3/GRASP. The values represent the mean LR per 2°x5° predefined grid.**~~

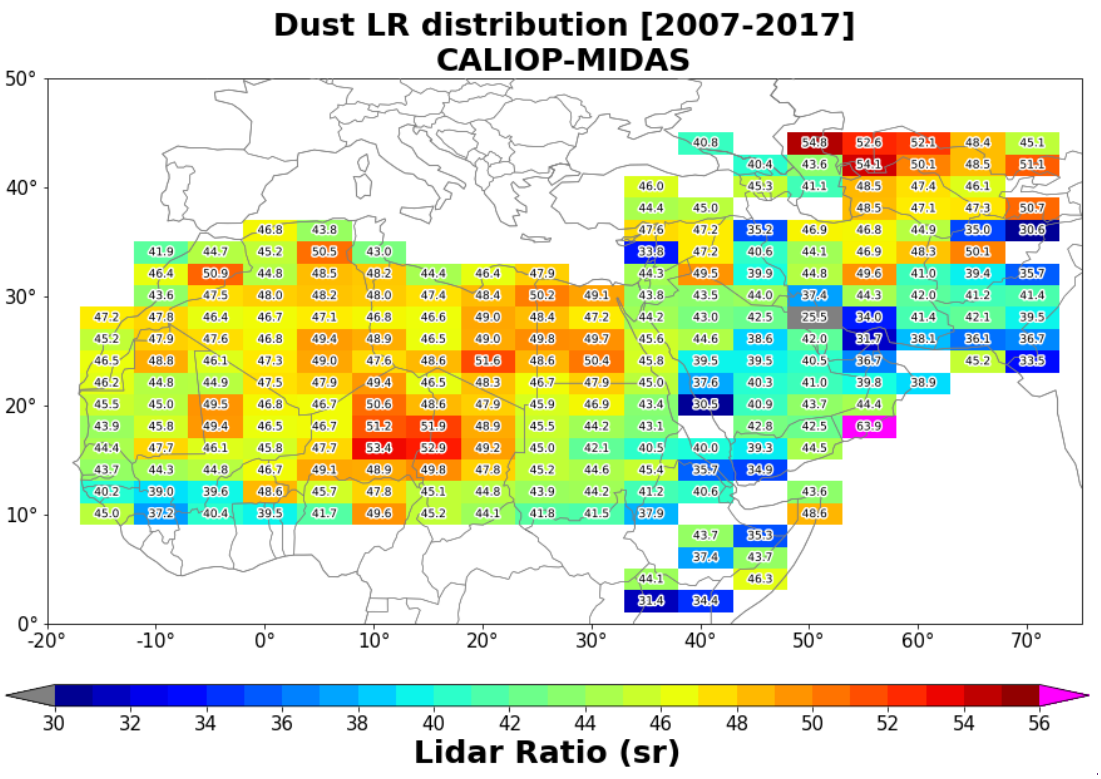
Dust LR distribution [2007-2017]
CALIOP-MIDAS
50°
40°
30°
20°
10°
0°
-20°
-10°
0°
10°
20°
30°
40°
50°
60°
70°
30
32
34
36
38
40
42
44
46
48
50
52
54
56
Lidar Ratio (sr)

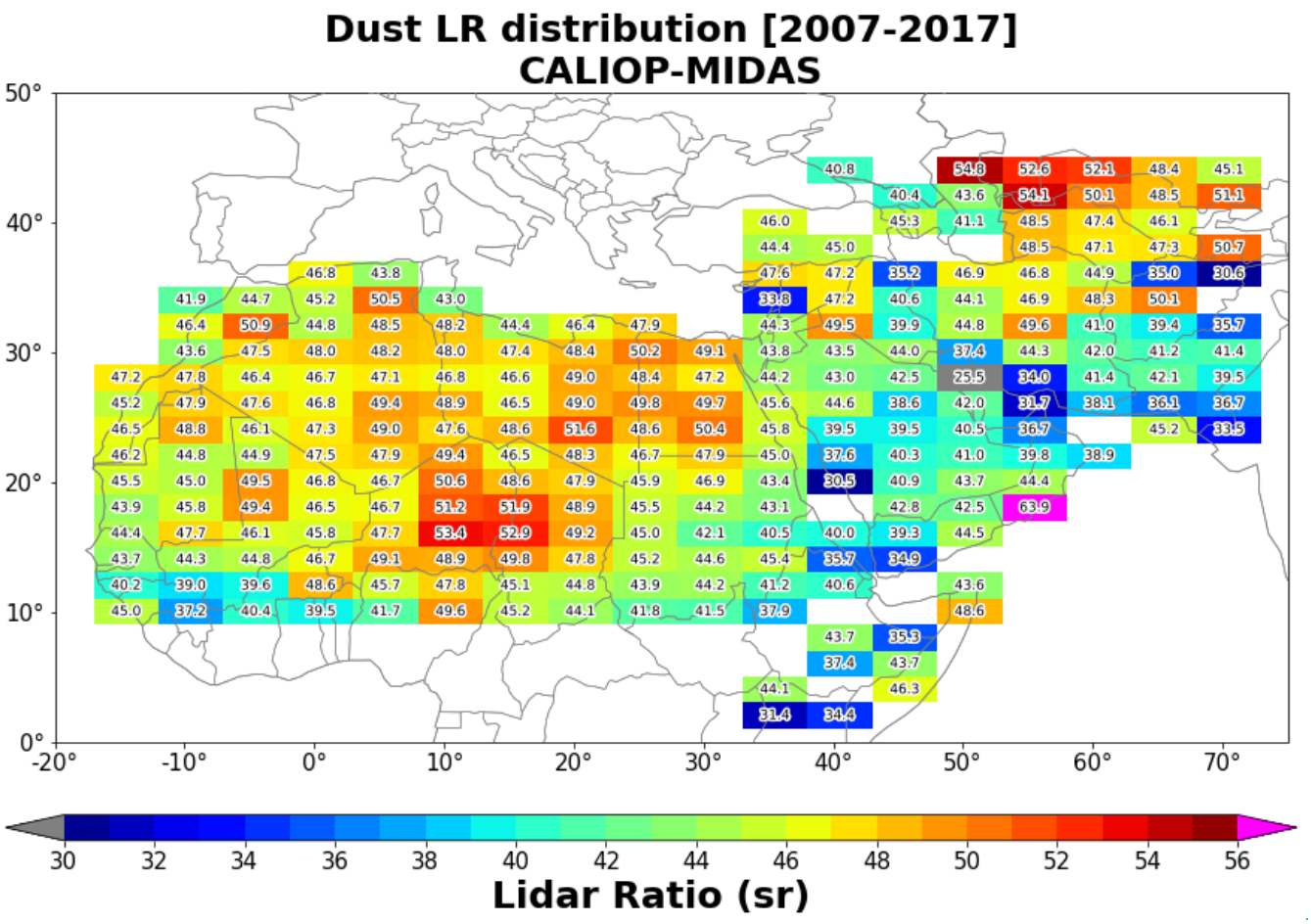
Dust LR distribution [2007-2017]
CALIOP-MIDAS
50°
40°
30°
20°
10°
0°
-20°
-10°
0°
10°
20°
30°
40°
50°
60°
70°
30
32
34
36
38
40
42
44
46
48
50
52
54
56
Lidar Ratio (sr)

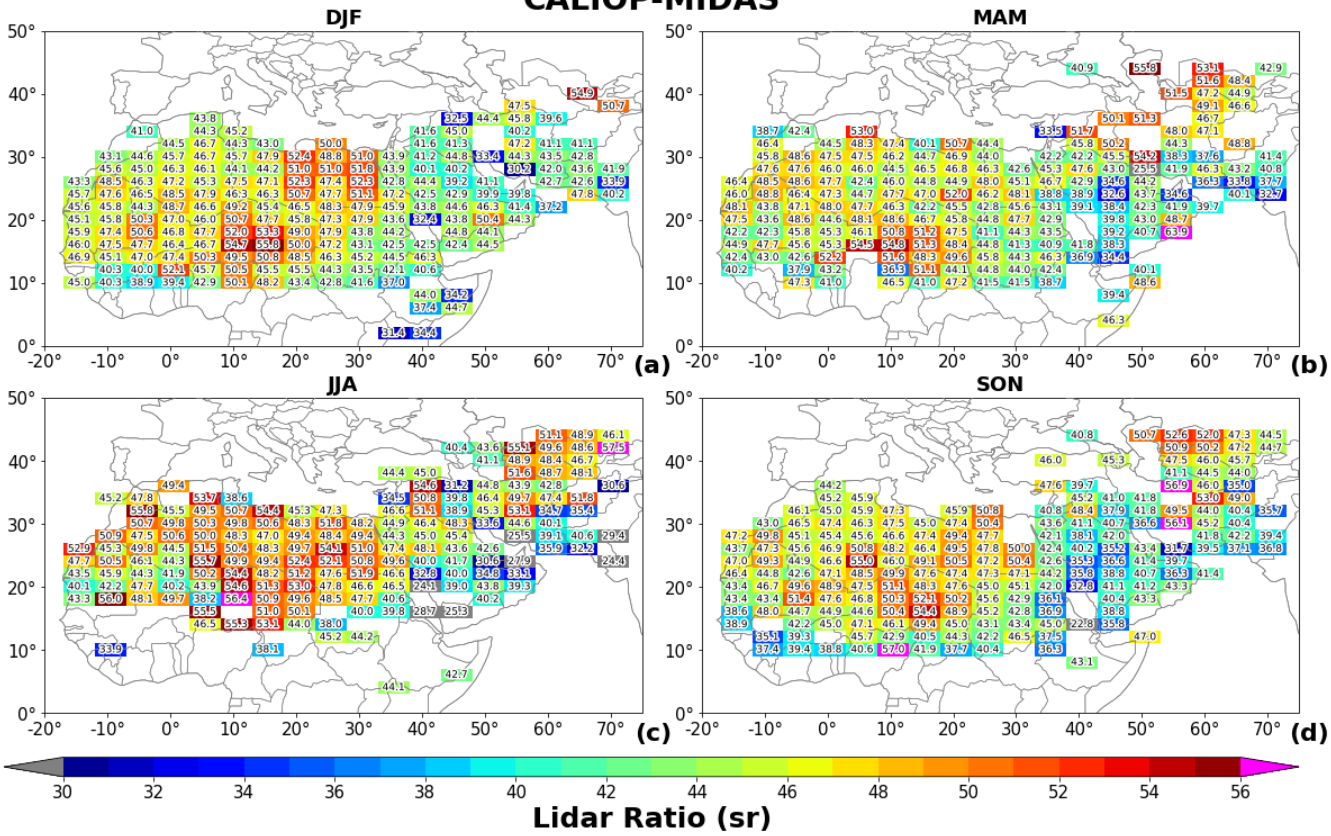
Seasonal Dust LR distribution [2007-2017]
CALIOP-MIDAS
DJF
MAM
JJA
SON
(a)
(b)
(c)
(d)
30
32
34
36
38
40
42
44
46
48
50
52
54
56
Lidar Ratio (sr)

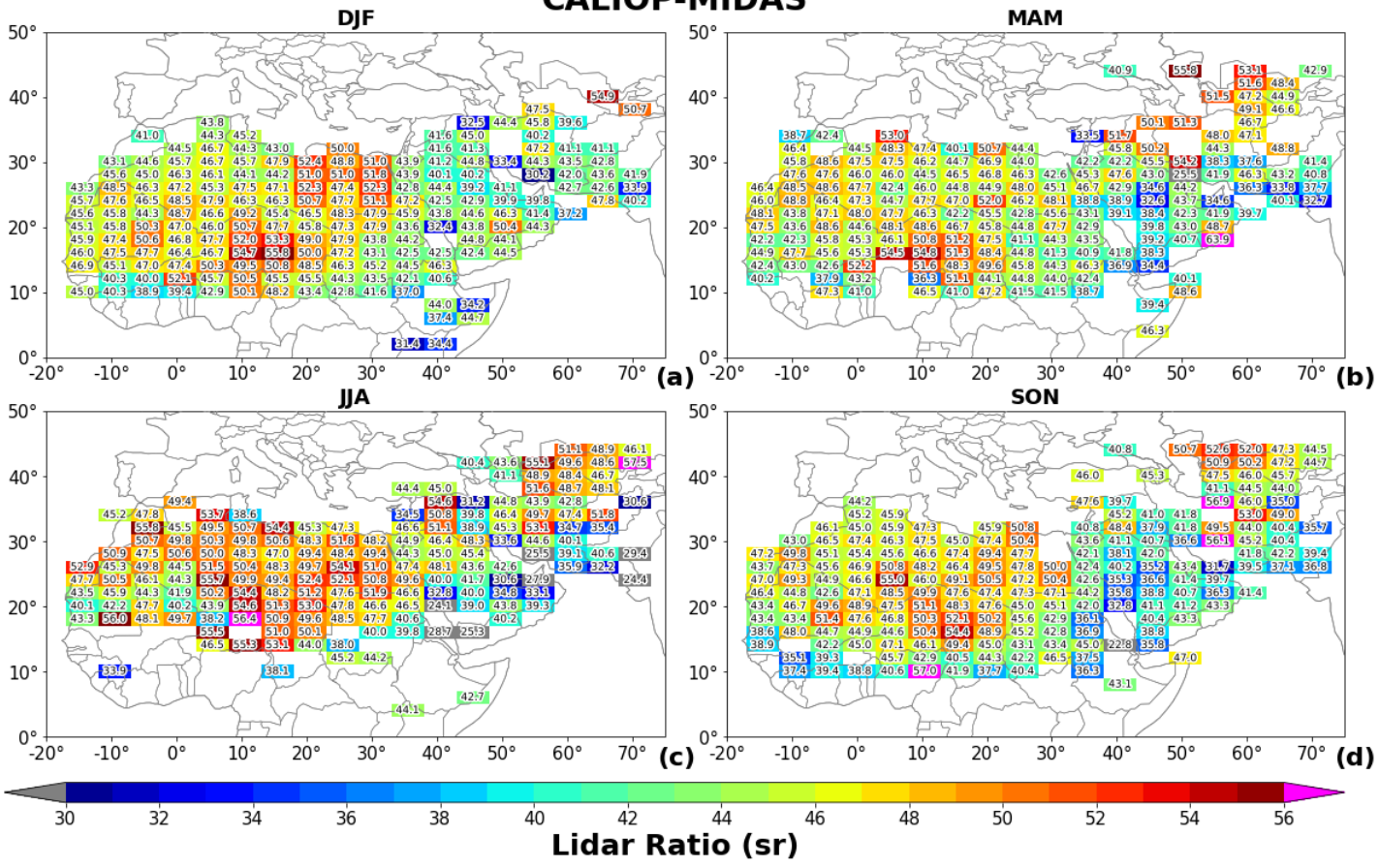
Seasonal Dust LR distribution [2007-2017]
CALIOP-MIDAS
DJF
MAM
JJA
SON
(a)
(b)
(c)
(d)
30
32
34
36
38
40
42
44
46
48
50
52
54
56
Lidar Ratio (sr)

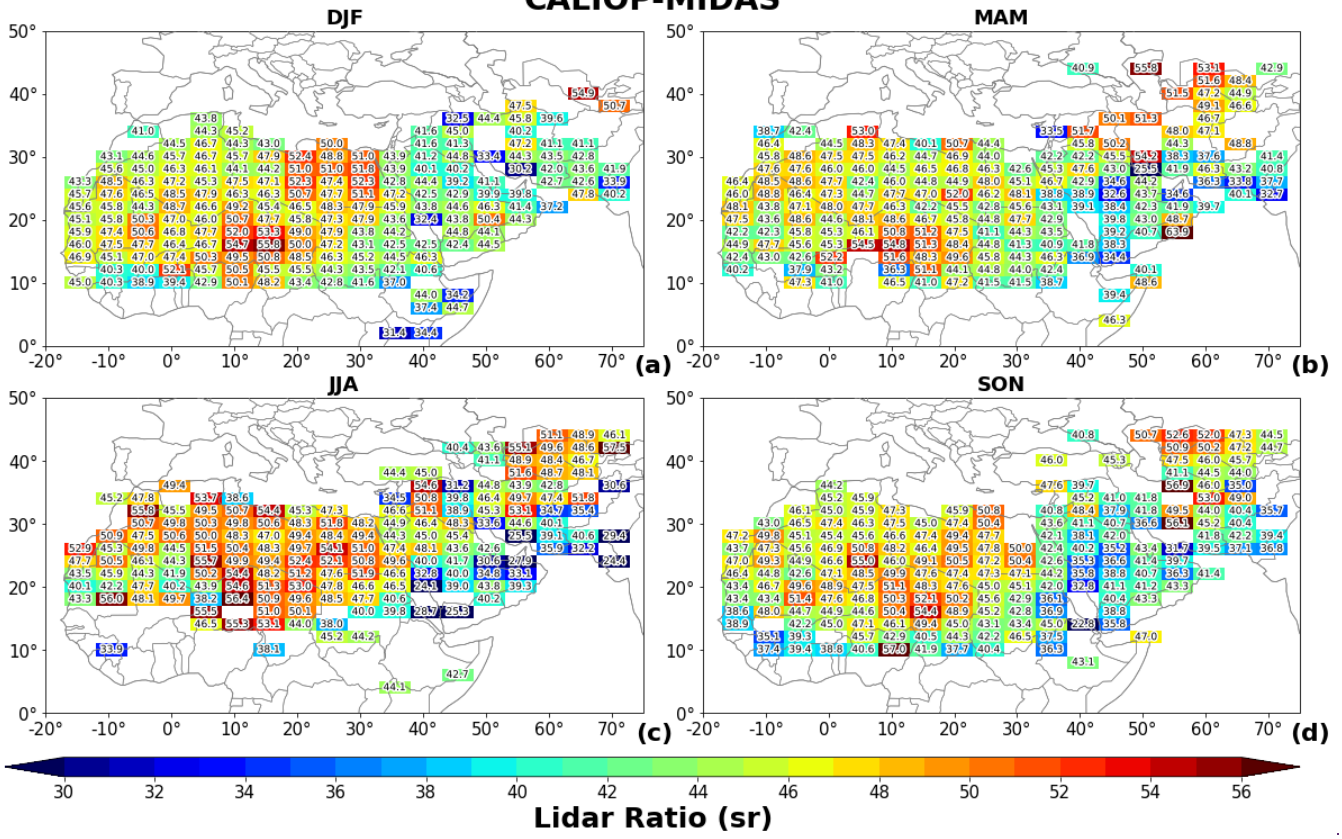
Seasonal Dust LR distribution [2007-2017]
CALIOP-MIDAS
DJF
MAM
JJA
SON
(a)
(b)
(c)
(d)
30
32
34
36
38
40
42
44
46
48
50
52
54
56
Lidar Ratio (sr)

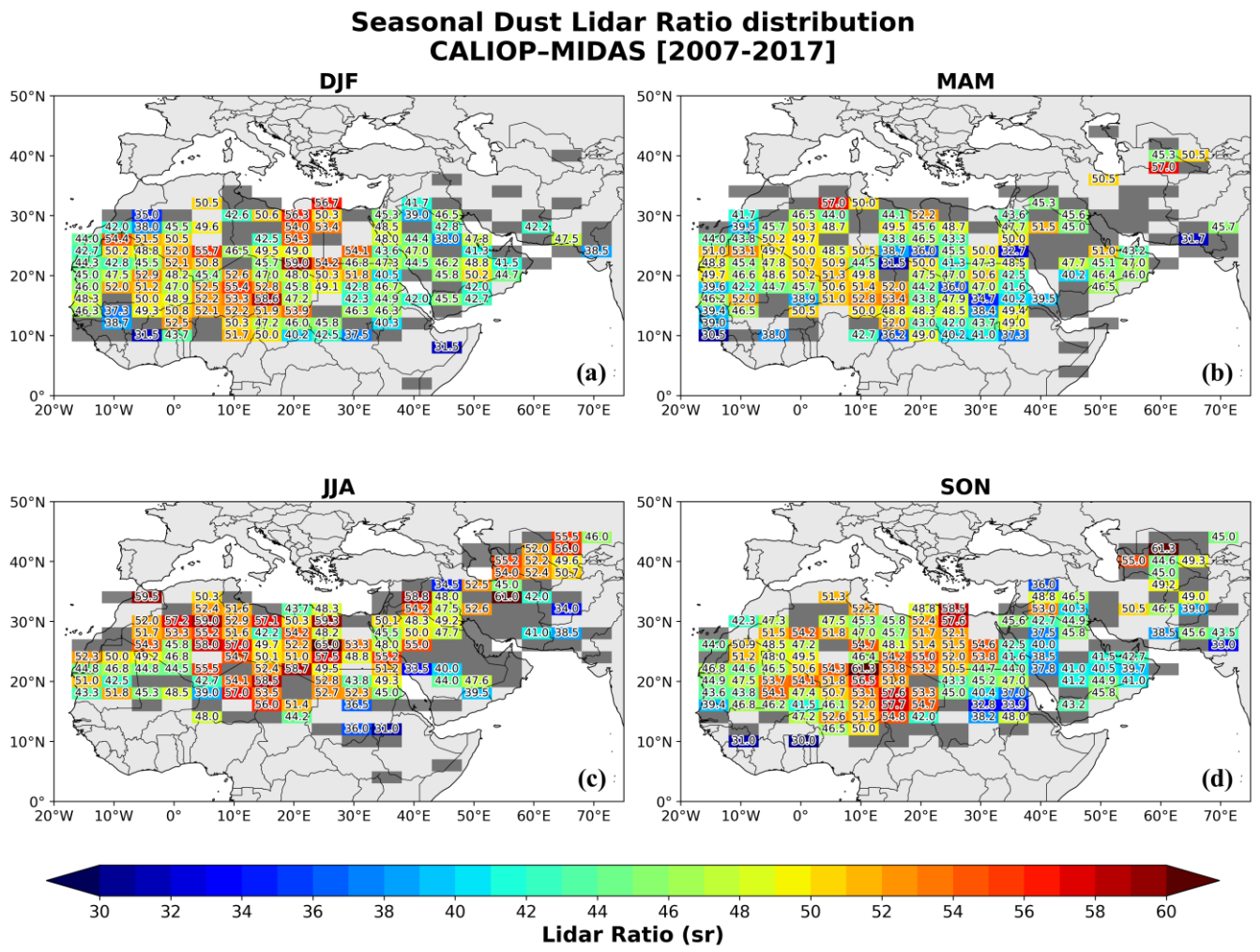

Figure 8~~7~~: ~~The seasonal distribution~~Seasonal geographical distributions of dust Lidar Ratio (LR) for (a) DJF, (b) MAM, (c) JJA and (d) SON ~~based on~~ resulted via the synergy ~~of~~ CALIOP ~~and~~ MIDAS. The values represent the mean LR ~~per~~ at each 2º × ~~x~~5º predefined grid. Grey-shaded grid cells indicate regions with only one available dust case, for which no robust LR estimate is provided.

~~number of matchups between spaceborne and ground-based retrievals (top x-axis). Note that for the seasonal CALIPSO-MIDAS synergy the stations Banizoumbou, Medenine IRA and Karachi are excluded since the seasonal collocation against AERONET didn't yield any significant number for cases, due to missing values of LR over a number of 2ºx5º predefined grids. Specifically, for the seasonal collocation against AERONET, based on the seasonal LR maps (Fig. 7) different LR values are applied in respect to the season (e.g. when a specific CALIPSO orbit passes over an AERONET station in June, the LR from Fig. 7c is applied to the satellite's retrieval for the derivation of the columnar DOD). Our findings indicate that across all stations and for the CALIOP-POLDER and CALIOP-MIDAS synergies during their overlapping periods, it is evident that the upgraded LRs lead to lower MBEs, with respect to those found when the default dust LRs is considered, thus indicating a~~

~~better agreement between CALIPSO and AERONET (Fig. 8a). This "improvement" coincides with a reduction of the RMSEs in 7 out of 9 AERONET sites. In most of the selected sites, the CALIPSO-AERONET agreement improves when the MIDAS DOD is considered for the calculation of the upgraded LR (blue bars) instead of the POLDER-3/GRASP AOD (green bars). However, it is noteworthy that both CALIPSO-MIDAS and POLDER-3-CALIPSO combinations indicate similar LR tendencies almost in all sites, which are necessary for minimizing CALIPSO-AERONET departures under dust scenes. It is reminded that negative LR differences indicate that the reduction of the default value (mainly required at sites in the Middle East) can improve the agreement between CALIPSO and AERONET. A reverse condition is valid for the AERONET sites situated in North Africa (i.e., an increase in dust LR is required). As expected, the modifications of both MBE and RMSE are highly dependent on the magnitude of the dust LR departures. This is attributed to the fact that the default/upgraded dust LRs are applied on the dust backscatter retrievals for the derivation of the dust extinction coefficient and finally of the dust optical depth (via the integration of the vertical dust extinction coefficient profile). Both MBEs and RMSEs exhibit a further decrease in Agoufou, Mezaira and Solar Village when the dust LRs are computed on a seasonal basis via CALIPSO-MIDAS synergy (indicated by the brown cyanbar). Overall, the proposed adjustments of the dust LR lead to better evaluation scores. However, persistent discrepancies between CALIPSO and AERONET remain, as previously documented in the literature (Amiridis et al., 2013; Kim et al., 2018; Moustaka et al., 2024). These deficits are primarily attributed to the inability of the CALIOP sensor in detecting tenuous layers, particularly during daytime due to the strong solar background illumination, as well as to misclassification issues in the CALIPSO aerosol classification scheme (Winker et al., 2009; Burton et al., 2012; Ma et al., 2013; Li et al., 2021).~~

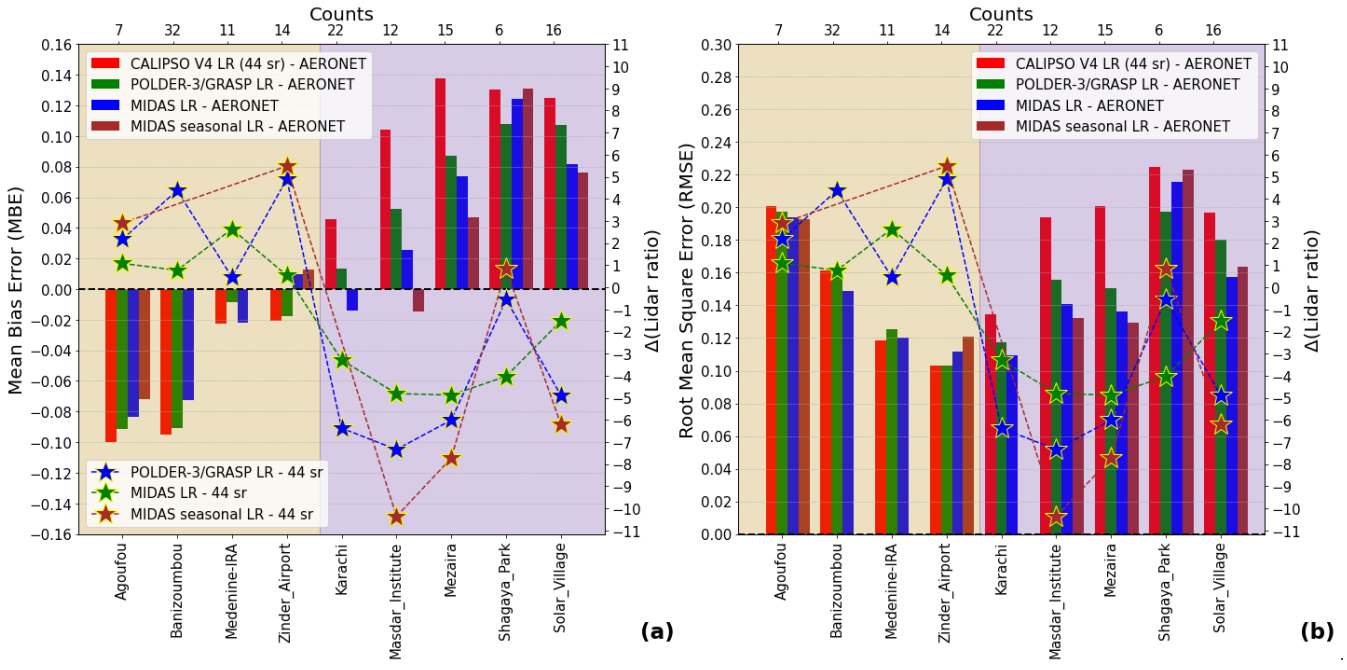

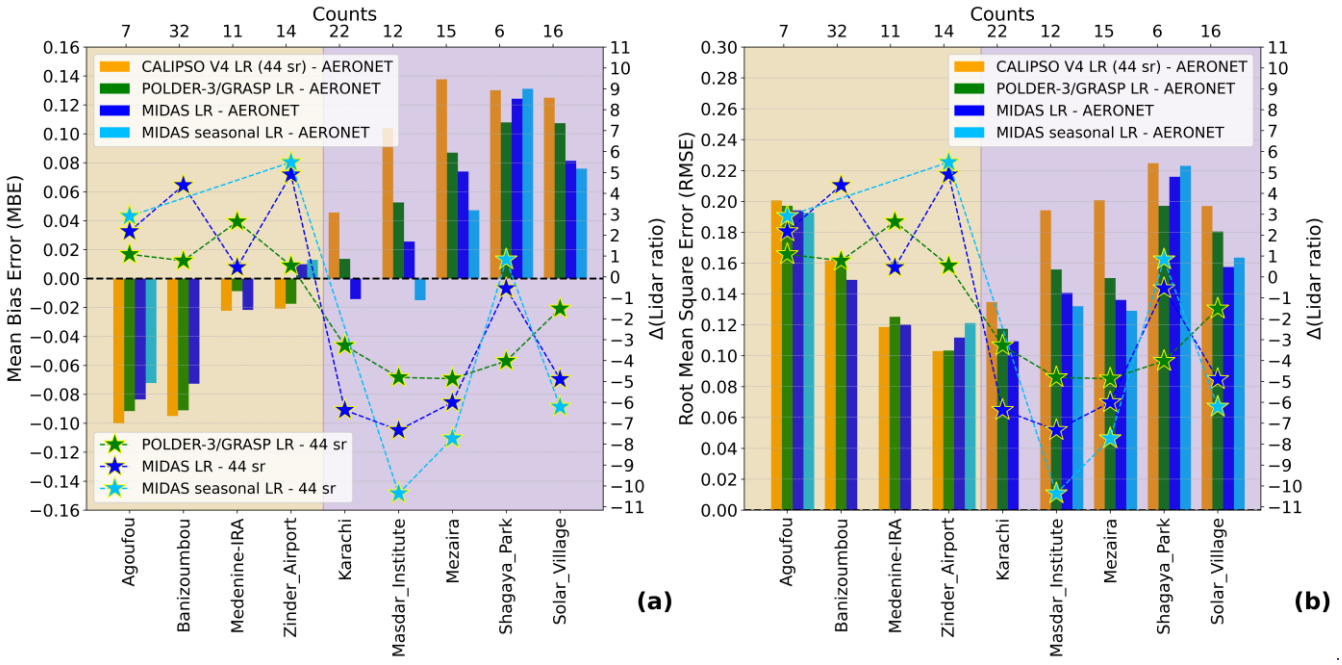

Figure 8: Bar plots of (a) Mean Bias Error (MBE) and (b) Root Mean Square Error (RMSE), from comparisons between AERONET and CALIOP DOD by applying the default CALIPSO dust LR of 44 sr (orangered bars), the updated LR from the synergy between CALIOP-POLDER-3/GRASP synergy (green bars), and the updated LR from the annual and seasonal synergy between CALIOP-MIDAS synergy (blue bars and brown cyanbars, respectively) on CALIOP's backscatter retrievals. On the bottom x-axis the AERONET stations used in the evaluation are presented, while in the top x-axis are the counts of the dust cases used for the derivation of the metrics per station. The second y-axis represents the LR_{diff} between the CALIOP default dust LR (44 sr) versus the dust LR from the synergies of CALIOP-POLDER-3/GRASP (green stars) and CALIOP-MIDAS (blue stars for annual; brown cyanstars for seasonal), respectively.

4.45 DOD climatology

In this section, we evaluate the impact of the revised dust LRs on dust climatology across a range of spatiotemporal scales. For the DOD analysis covering the period from 2007 to 2022, we apply on CALIOP's dust backscatter retrievals, gridded at 1° x 1° spatial resolution, the default dust LR as well as those resulting from the synergies of CALIOP-POLDER-3/GRASP (annual basis) and CALIOP-MIDAS (both on an annual and seasonal basis). The vertical profiles of the dust backscatter coefficient have been derived via a well-established discrimination technique (Tesche et al., 2009b), which effectively separates dust from non-dust components in dusty mixtures (polluted dust and dusty marine - Kim et al. 2018). The validity of the discrimination technique has been justified in numerous past works (Amiridis et al., 2013; Freudenthaler et al., 2009; Amiridis et al., 2013; Nisantzi et al., 2014; Mamouri and Ansmann, 2014; 2017; Hu et al., 2020; Wang et al., 2022; Xiao et al., 2023; Panahifar et al., 2023). In our study, we also apply certain modifications to the depolarization ratio thresholds, as detailed in the recent work by Moustaka et al. (2024). These thresholds are derived from the DeLiAn database (Floutsi et al., 2023) and are set at 0.28 for dust and 0.03 for polluted continental/smoke aerosols. For marine layers, the thresholds vary depending on humidity

conditions (Haarig et al., 2017b), with values of 0.01 for wet and 0.15 for dry environments. It is important to be clarified that all CALIPSO orbits intersecting the two ROIs are processed without employing the criteria outlined in Section 3.1. Moreover, we are excluding from our analysis all grids in which the upgraded dust LRs have been computed based solely on a single collocated dust case (see supplementary Figs. S2, S5 and S8) between the different sensors (CALIOP, POLDER-3, MODIS).

5.4.1 Annual and Sseasonal DOD geographical patterns

In Fig. 9, we present the spatial distribution of CALIPSO DOD at 532 nm, representative over a 15-year period (2007-2022), computed based on its default algorithm (a-i), in which a constant value of 44 sr is applied on the backscatter retrievals for the derivation of the columnar DOD. Concurrently, we have reproduced the temporal averaged maps utilizing the revised dust LRs (a-ii to a-iv), derived from the CALIOP-POLDER-3/GRASP and CALIOP-MIDAS synergies. The DOD differences between the DODs computed with the updated LRs versus the CALIPSO default DODs are also presented on the right column of Fig. 9. Furthermore, in Fig. 10 we display the corresponding seasonal DOD patterns during (a) DJF, (b) MAM, (c) JJA, and, (d) SON. The first two columns correspond to the DOD retrievals with (i) the CALIPSO default dust LR and (ii) with the seasonal LRs obtained from the CALIOP-MIDAS synergy, while in the last column we present the DOD departures, driven by the LR adjustments for each synergistic approach, as presented in Figs. S3, S6 and S9.

Based on the default CALIPSO retrieval algorithm, the most intense dust loads (DODs up to 0.5) are recorded in the western Sahara, in Saudi Arabia, along the coastal regions of Iran as well as in the southern part of Pakistan. In other areas, DODs do not exceed 0.3, except in Iraq, where DODs can reach up to 0.4 (Fig. 9 a-i). Through the implementation of the upgraded dust LRs, the spatial patterns of DOD are modified remarkably. In North Africa, a zone of high DODs (up to 0.6) stretching from Mauritania to Chad and it is bounded between 10° N and 25° N is visible in all possible synergies between the active (CALIPSO) and passive (POLDER-3/MODIS) spaceborne instruments. Within this zone, two "spots" of maximum DODs in Mali-Mauritania and in Niger-Chad are recorded. An interesting finding is the almost two-fold increase of DOD in the Bodélé Depression, the most active dust source ofon the planet (Washington et al., 2009), when the adjusted dust LRs are considered. Due to the increase of dust LR, the updated CALIOP DODs are less underestimated than those (0.8-1.2) given in Gkikas et al. (2022). Similarly, the upgraded DODs (0.6-0.7) in the El-Djouf Desert (Mauritania-Mali) match better with those found in Gkikas et al. (2022). Across Algeria, Libya and Egypt, as well as in Soudan, slightly higher DODs are derived through the CALIOP-POLDER-3/GRASP synergy (Fig. 9 a-ii) compared to those calculated by combining CALIOP and MIDAS on an annual basis (Fig. 9 a-iii). Within the zone of high DODs, the two peaks are more distinguishable when the new LRs have been calculated from the collocated CALIOP-MIDAS sample on a seasonal basis. Moreover, areas yielding moderate DODs (0.3-0.4) are recorded in Libya and in Egypt. The increase of DODs in North Africa, after the implementation of the upgraded dust LRs, is evident throughout the year, as illustrated in Fig. 10. The most evident differences between the default and the upgraded DOD spatial distributions are encountered in Niger-Chad becoming maximum in JJA. During summer, the activation of dust sources (Ginoux et al., 2012; Hu et al., 2019) in the western Sahara Desert is depicted both when the default (Fig. 10 c-i) and the adjusted (Fig. 10 c-ii) LRs are considered. Notably, during the boreal summer (Fig. 10 c-ii), a large part of the western Sahara experiences significant dust loadings (DOD > 0.5) in agreement with other studies in the literature (Pu and Ginoux,

2018; Song et al., 2021; Gkikas et al., 2022; Tindan et al., 2023). In addition, the updated DODs are higher and align closely with those (0.7–0.8) reported by Gkikas et al. (2022) and Song et al. (2021), respectively.

Over the Arabian Peninsula, the spatial extension of moderate DODs (0.3–0.4), observed in the default CALIPSO patterns (Fig. 9 a-i), is shrank on the corresponding maps generated with the adjusted dust LRs (Figs. 9 a-ii, 9 a-iii, 9 a-iv). Among the three synergies, similar DOD fields are drawn between the CALIOP-POLDER-3/GRASP (Fig. 9 a-ii) and CALIOP-MIDAS (Figure 9 a-iv; seasonal) combinations. In both patterns, the highest DODs (up to 0.5) are recorded in the Rub' al Khali Desert (southern sector of S. Arabia) in agreement with Gkikas et al. (2022) and Tindan et al. (2023). In addition, the lowest DODs across the Arabian Peninsula are obtained from the CALIOP-MIDAS synergy (Fig. 9 b-ii). As can be seen in Figs. 9 a-ii to iv, the annual DOD patterns over the Arabian Peninsula are highly variable in spatial terms (i.e., Mesopotamia) due to the pronounced LR diversity over the region, as discussed in Section 4.2. On a seasonal basis (Fig. 10), the spatial variability of the dust burden in the Arabian Peninsula is commonly reproduced, when the default (first column) and the revised (second column) dust LRs are applied, in contrast to what has been found over North Africa. However, it is evident that there are discrepancies between the seasonal maps produced with the default and the adjusted dust LRs. These discrepancies are recorded on the DOD magnitude, which is higher based on the default CALIPSO lidar ratio with respect to those derived from the revised values (i.e. CALIPSO-MIDAS synergy). Similar to North Africa, DODs also peak over the Arabian Peninsula during the JJA, with values predominantly above 0.4, consistent with findings from other studies in the literature (Pu and Ginoux, 2018; Song et al., 2021).

Based on the default CALIPSO dust LR, dust loads over the Karakum (Turkmenistan), the Kyzylkum (Uzbekistan) Deserts, in the Ustyurt Plateau (Li and Sokolik, 2018) and in the Garabogazköl Basin (Shen et al., 2016) yield low optical depths (< 0.15) (Fig. 9 a-i). Their intensity increases after the implementation of the revised LRs with positive departures ranging from 0.05 to 0.1 (CALIOP-POLDER-3/GRASP; Fig. 9 b-i) and from 0.05 to 0.25 (CALIOP-MIDAS; Figs. 9 b-ii and 9 b-iii). These DOD increments are mainly observed during summer when the dust activity maximizes over the area (Elguindi et al., 2016; Shen et al., 2016; Li and Sokolik, 2018; Song et al., 2021; Gkikas et al., 2022) in agreement with other studies in the literature (Pu and Ginoux, 2018; Gkikas et al., 2022; Tindan et al., 2023). Declining DOD tendencies are recorded along the eastern coasts and the southern sector (Dasht-e-Margo Desert) of Iran, in Afghanistan and in the southern parts of Pakistan.

The regional maps of the DOD departures (i.e., the right column in Fig. 9 and the third column in Fig. 10) can effectively demonstrate the effect of the adjusted dust lidar ratios on the CALIPSO dust optical depth levels. The analysis reveals a discernible pattern in the DOD departures, underscoring the necessity for adjustments to the CALIPSO dust lidar ratio to enhance the congruence between CALIOP and either POLDER-3/GRASP or MIDAS. Across North Africa, positive departures predominate attaining maximum magnitude primarily in proximity to dust sources. A transition zone is evident between the Sahara and the Arabian Peninsula, characterized by almost neutral DOD biases, as evidenced by the CALIOP-MIDAS synergy. In most parts of the Arabian Peninsula, the predominance of relatively low negative DOD biases indicates that the default dust LR (44 sr) should be slightly lower. In contrast to the CALIOP-MIDAS combinations, the signal of the DOD biases derived via the CALIOP-POLDER synergy itsynergy is not uniform.

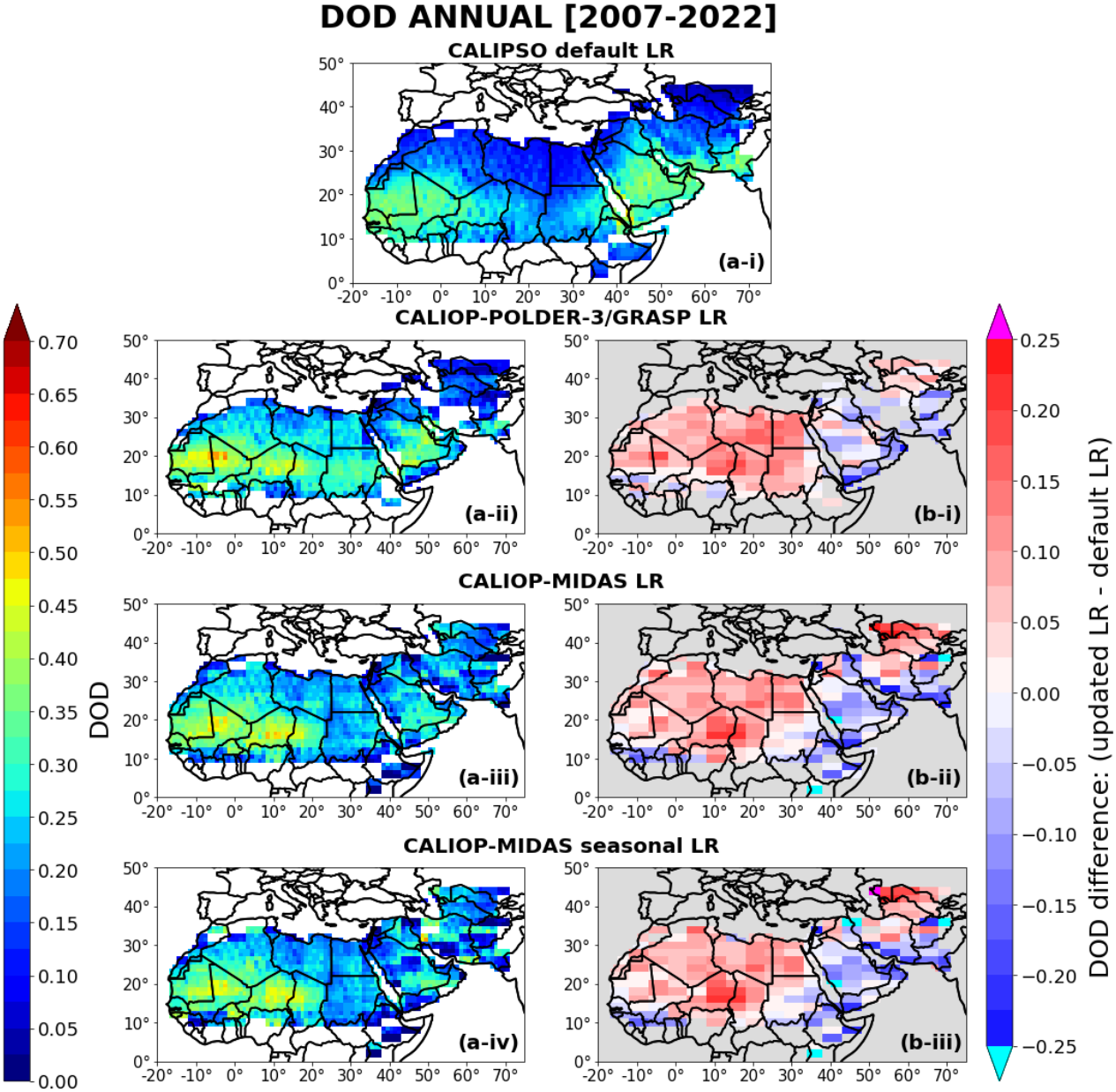
DOD ANNUAL [2007-2022]
CALIPSO default LR
(a-i)
CALIOP-POLDER-3/GRASP LR
(a-ii)
(b-i)
CALIOP-MIDAS LR
(a-iii)
(b-ii)
CALIOP-MIDAS seasonal LR
(a-iv)
(b-iii)
DOD
0.70
0.65
0.60
0.55
0.50
0.45
0.40
0.35
0.30
0.25
0.20
0.15
0.10
0.05
0.00
DOD difference: (updated LR - default LR)
0.25
0.20
0.15
0.10
0.05
0.00
−0.05
−0.10
−0.15
−0.20
−0.25

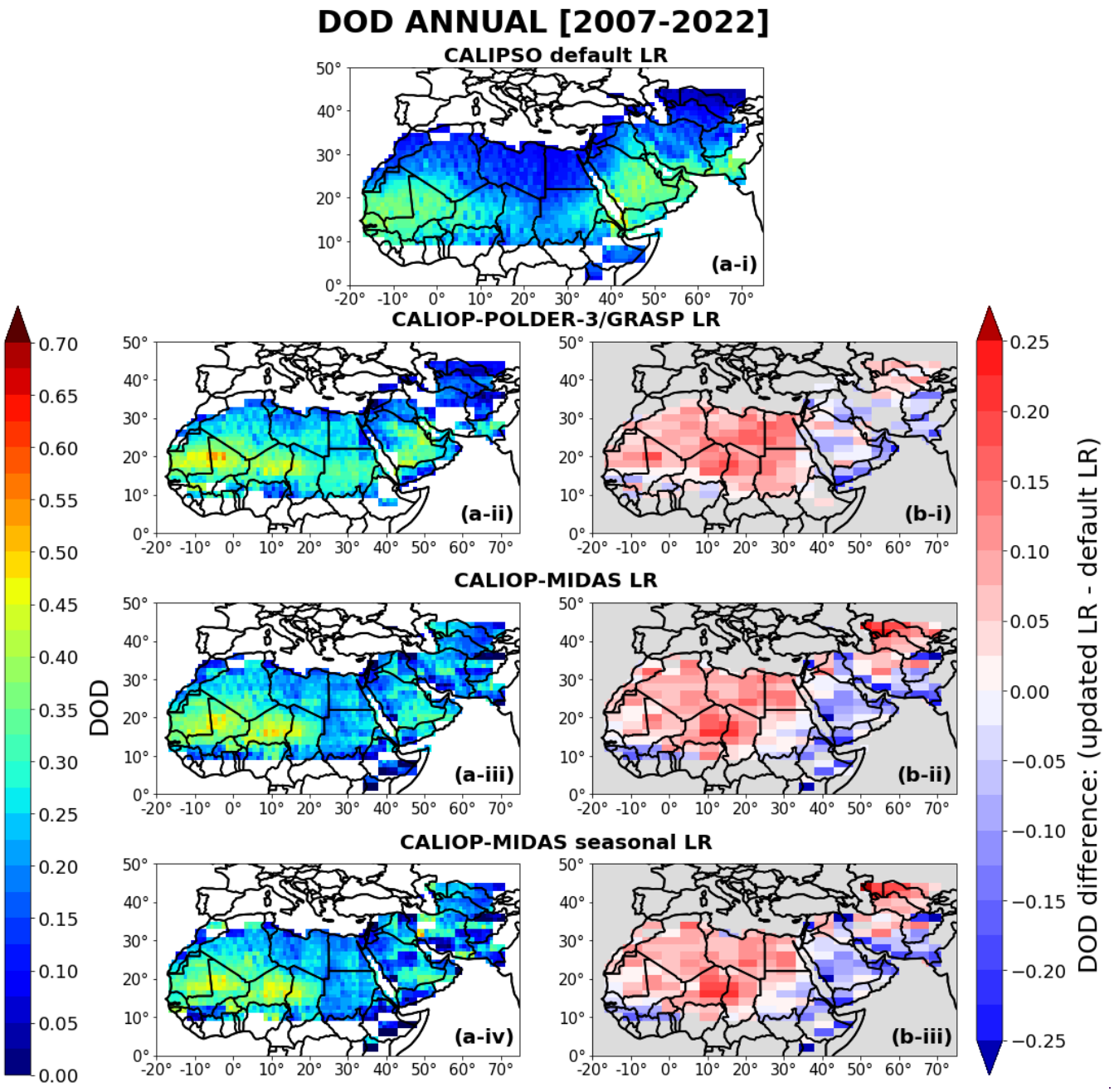

~~Figure 9: Geographical distribution of the annual Dust Optical Depth (DOD) at 532 nm based on (a-i) the CALIPSO default LR, (a-ii) the LR from the synergy of CALIOP-POLDER-3/GRASP and (a-iii, a-iv) the annual and seasonal LR from the CALIOP-MIDAS synergy. The DOD differences between the CALIPSO default product and the DODs derived from the synergies of (b-i) CALIOP-POLDER-3 and (b-ii, b-iii) CALIOP-MIDAS are also presented in the right column.~~

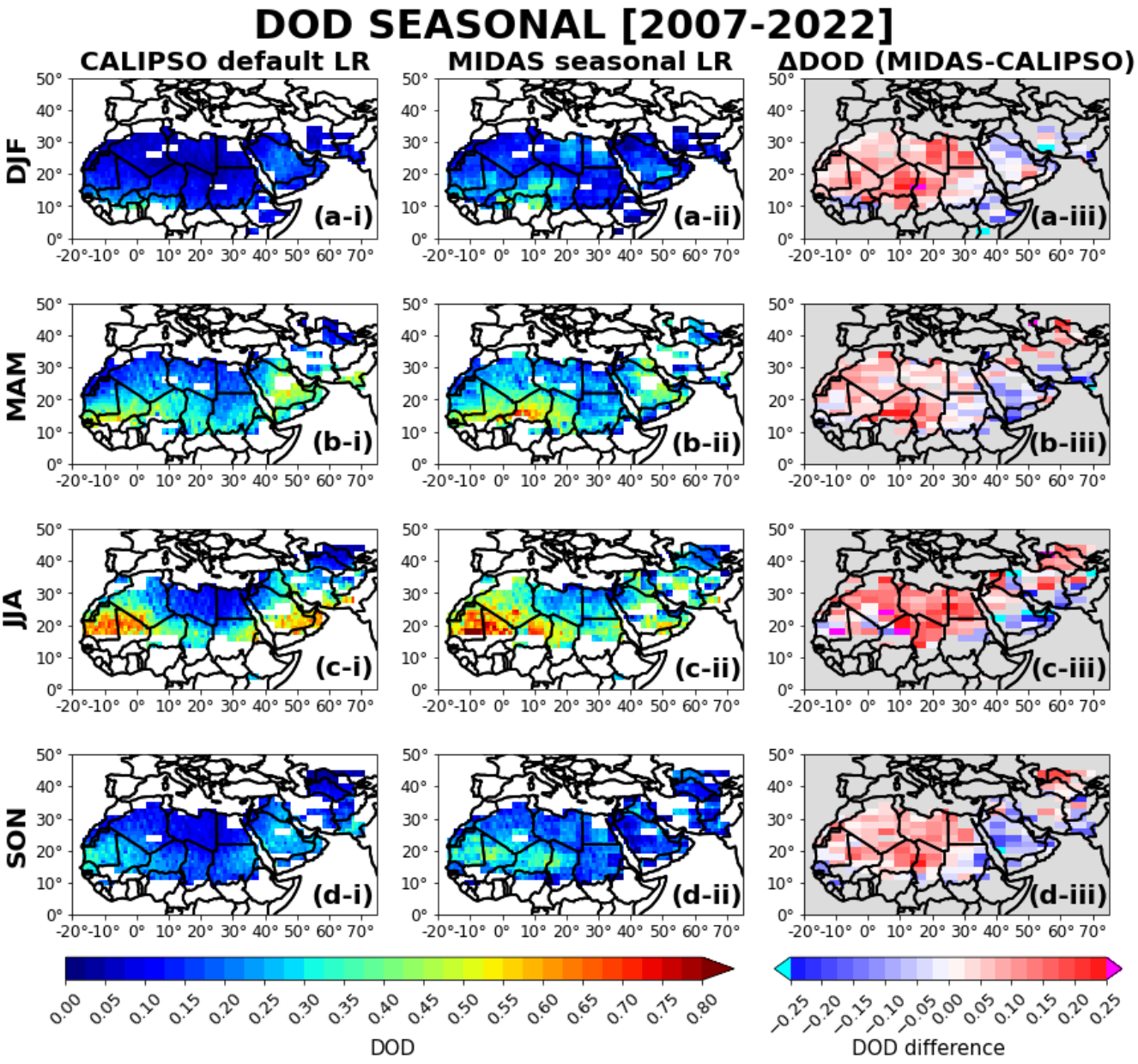
DOD SEASONAL [2007-2022]
CALIPSO default LR
MIDAS seasonal LR
ΔDOD (MIDAS-CALIPSO)
DJF
MAM
JJA
SON
(a-i)
(a-ii)
(a-iii)
(b-i)
(b-ii)
(b-iii)
(c-i)
(c-ii)
(c-iii)
(d-i)
(d-ii)
(d-iii)
0.00 0.05 0.10 0.15 0.20 0.25 0.30 0.35 0.40 0.45 0.50 0.55 0.60 0.65 0.70 0.75 0.80
DOD
−0.25 −0.20 −0.15 −0.10 −0.05 0.00 0.05 0.10 0.15 0.20 0.25
DOD difference

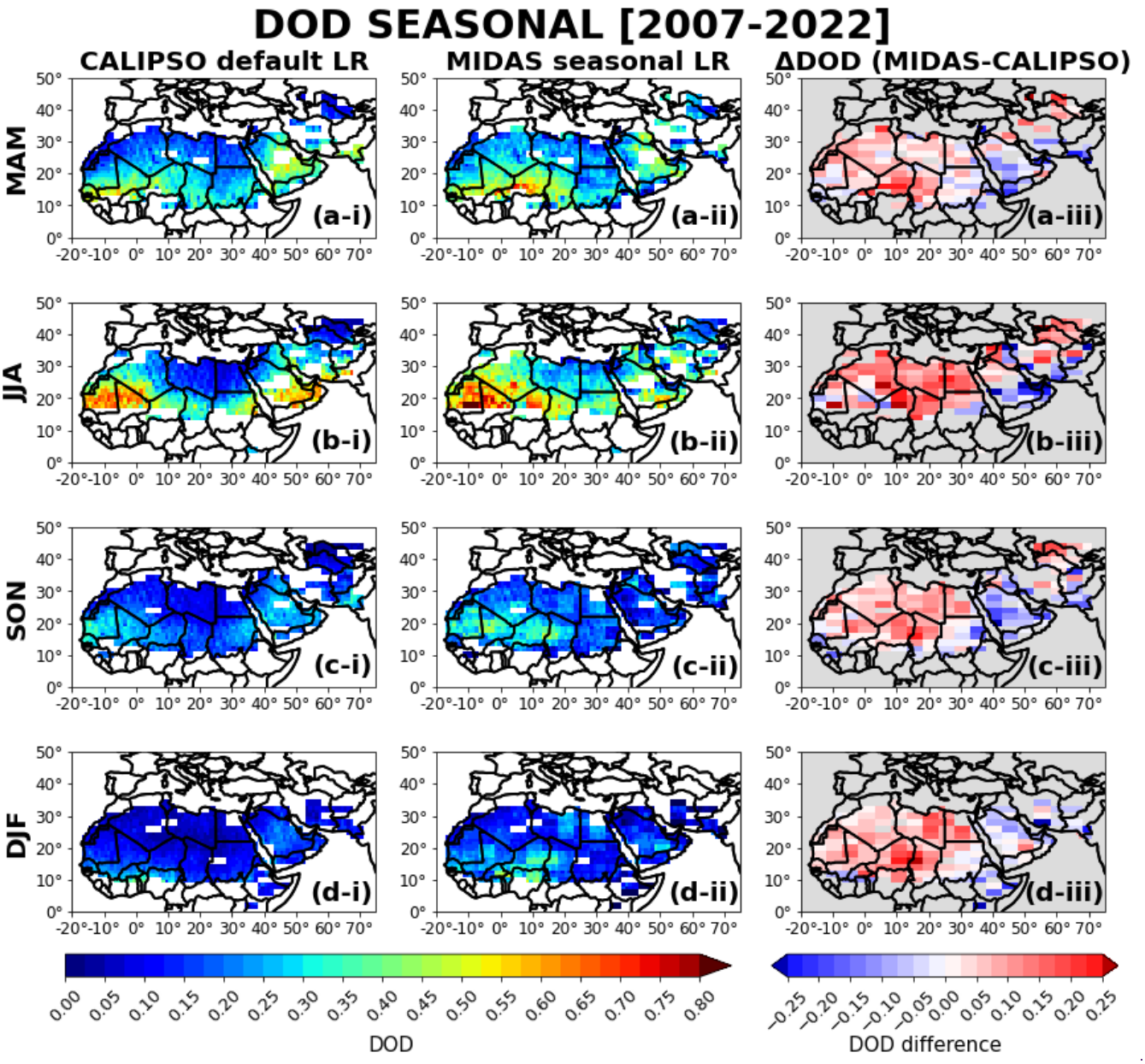

~~Figure 10: Geographical distribution of the seasonal Dust Optical Depth (DOD) at 532 nm during (a) DJF, (b) MAM, (c) JJA and (d) SON, based on (i) the CALIPSO default LR and (ii) the seasonal LR from the synergy of CALIOP-MIDAS, while in the 3rd column (iii) the DOD differences between the two DOD retrievals are also presented separately for each of the 4 seasons.~~

5~~4~~.4.2 DOD inter-annual and intra-annual variability

An assessment of the adjusted dust LRs on the CALIOP DODs at a regional scale was also performed. Figure 11 illustrates the inter-annual (i) and the intra-annual (ii) DOD timeseries, representative for the 2007-2022 period, separately for North Africa (a; yellow shaded areas in Fig. 1a) and the Middle East (b; purple shaded areas in Fig. 1a). The regional DODs have been reproduced based on the standard dust LRs (orangered line) as well as with the corresponding values derived by the CALIOP-POLDER synergy (green line), the CALIOP-MIDAS synergy (blue line) and the CALIOP-MIDAS synergy applied on a seasonal basis (brown cyanline). As expected, there is positive shift for DODs (ranging from 0.05 to 0.15) over North Africa (Fig. 11 a i) when the adjusted dust LRs are implemented, due to the positive DOD departures dominating across the Sahara Desert (Figs. 9 and 10). The seasonal DOD cycle is almost commonly reproduced among all approaches with minima and maxima DODs during winter and in June, respectively (Fig. 11 a ii). However, there are differences in the regional DODs. Specifically, the lowest levels are obtained when the default dust LR (orangered line) is used, with DODs ranging from 0.1 to 0.34. The implementation of the dust LRs provided by the CALIOP-MIDAS synergy on an annual basis (blue line) results in an increase of the DODs from 0.05 to 0.08. Slightly higher DODs are found based on the CALIOP-POLDER-3 synergy (green line). These minor DOD deviations found between the MIDAS-based and the POLDER-based LRs can be interpreted by the fact that for MIDAS the DOD is used instead of the AOD utilized in the CALIOP-POLDER-3 synergy. The derivation of dust LR based on the seasonally collocated CALIOP-MIDAS sample (brown cyanline) leads to higher DODs, compared to the default CALIPSO values (Fig. 11 a ii), similarly to what has been shown for the other two combinations. Nevertheless, the increments vary with time and are maximum during the dry period of the year, reaching up to 0.13, while they are suppressed during winter (up to 0.05).

In the Middle East (bottom panel in Fig. 11), the consideration of the adjusted dust LRs leads in a slight reduction of the default regional CALIOP DODs, throughout the study period (Fig. 11 b i). In terms of magnitude, the regional DODs based on the default CALIPSO aerosol scheme varies from 0.05 to 0.45 whereas the maximum values are significantly reduced in 2019, 2020 and 2021. The systematic negative DOD offset is better evident in the intra-annual variation plot (Fig. 11 b ii), which also shows that the three curves (orangered, green and blue) covariate within the course of the year. On an annual basis, DODs are minimized in December whereas the maximum levels are recorded in June (Fig. 11 b ii). The intra-annual DOD pattern slightly changes when the seasonal dust lidar ratios derived from the CALIOP-MIDAS synergy are applied (brown cyancurve in Fig. 11 b ii). More specifically, the DOD peak shifts from June to May and decreases from 0.35 to 0.33, whereas the minimum DODs are observed in November instead of December. Furthermore, the updated DODs are slightly higher/lower than the default levels in May/March and identical in April. The DOD peaks recorded in either May or June have also been reported by Gkikas et al. (2022) and in Song et al. (2021). Nevertheless, the differences found between the findings of the current work and those reported in the aforementioned studies, apart from the different study periods, are due to the different regions considered. In this study, the regional DODs have been calculated considering the entire Middle East region instead of its specific parts, as has been presented in Gkikas et al. (2022) and Song et al. (2021).

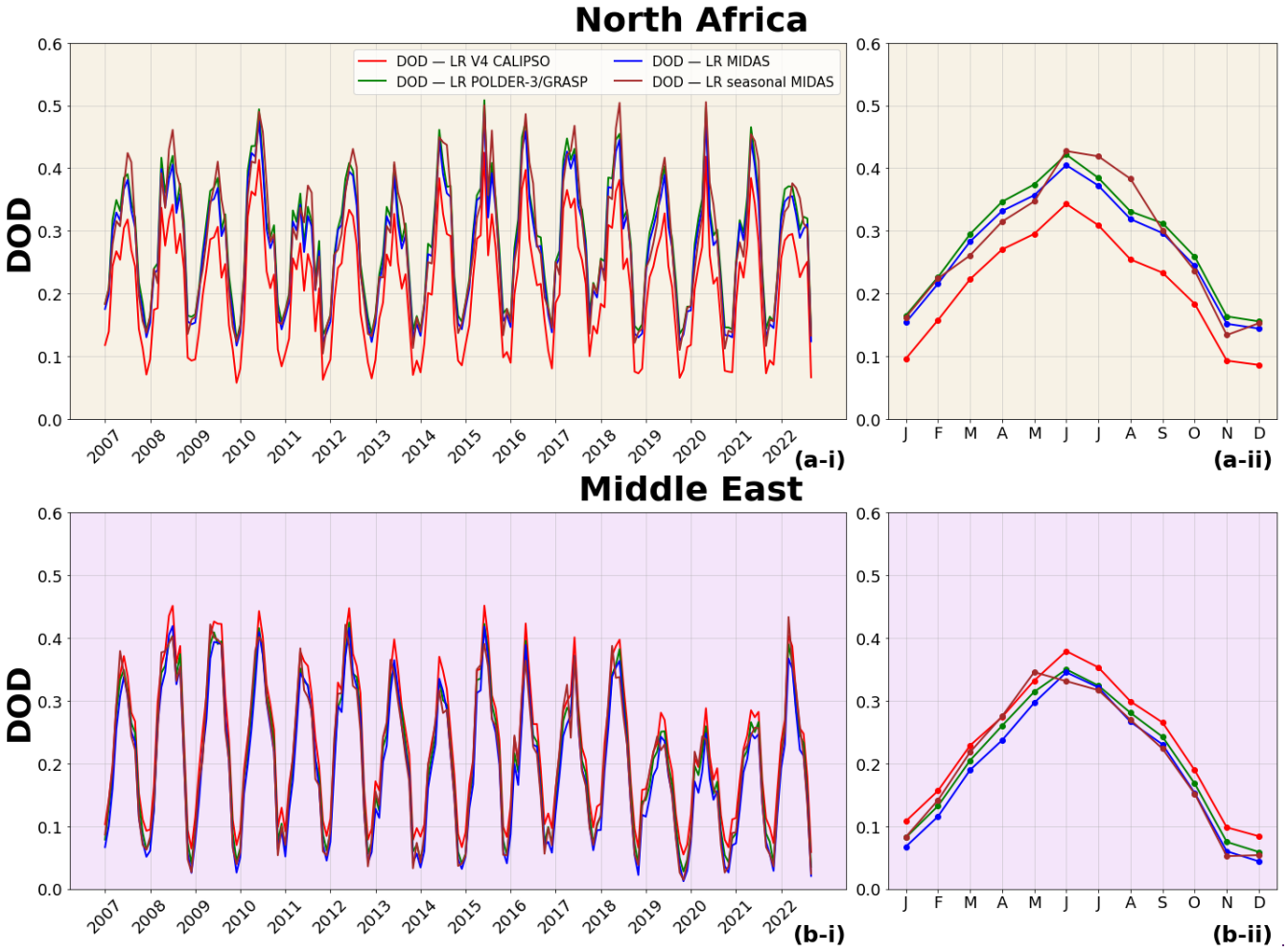
North Africa
DOD — LR V4 CALIPSO
DOD — LR POLDER-3/GRASP
DOD — LR MIDAS
DOD — LR seasonal MIDAS
DOD
0.0
0.1
0.2
0.3
0.4
0.5
0.6
2007
2008
2009
2010
2011
2012
2013
2014
2015
2016
2017
2018
2019
2020
2021
2022
(a-i)
J
F
M
A
M
J
J
A
S
O
N
D
(a-ii)
Middle East
DOD
(b-i)
(b-ii)

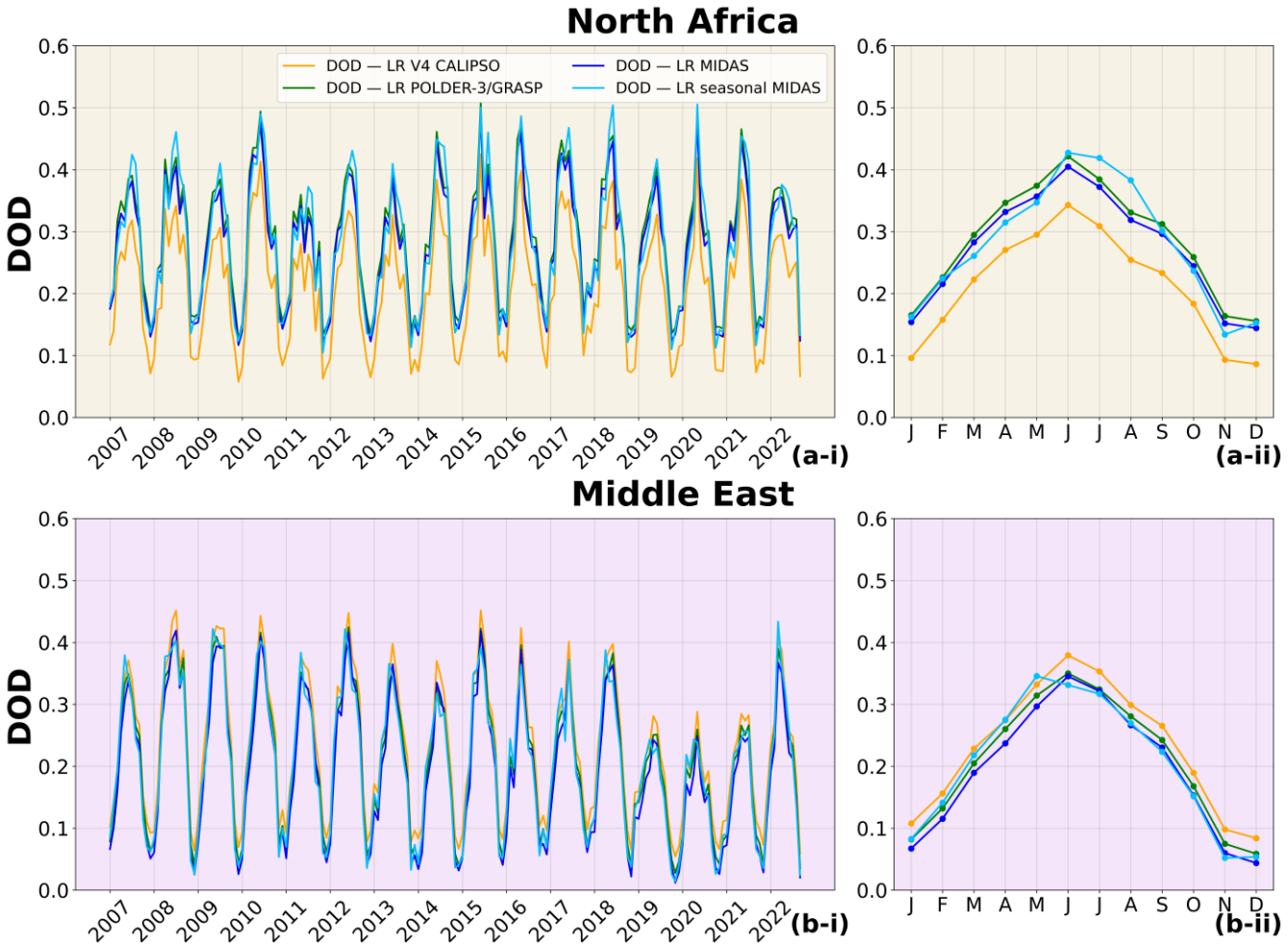

~~**Figure 11: Interannual (i) and interseasonal (ii) variability of Dust Optical Depth (DOD) at 532 nm, representative for the period 2007–2022, regionally averaged over (a) North Africa and (b) Middle East. The orangered color represents the DOD computed with the CALIPSO default LR, while green, blue and brown cyancolors are used for the implementation of the updated LR values based on CALIOP-POLDER-3/GRASP and CALIOP-MIDAS annual and seasonal synergies, respectively.**~~

5 Summary and conclusions

The CALIPSO satellite mission has provided unprecedented state-of-the-art aerosol and cloud observations over a 17-year period (2006-2023), significantly improving our knowledge of various aerosol-related processes relevant to a wide range of environmental applications. The CALIOP lidar, mounted on the CALIPSO satellite, has delivered aerosol and cloud vertical profiles, up to the lower stratosphere, probing areas characterized by diverse atmospheric constituents. One of the key advantages of the CALIOP lidar is the deployment of a depolarization channel enabling the detection of non-spherical particles (e.g., dust, volcanic ash, ice crystals). Previous studies have documented that the CALIPSO aerosol retrieval algorithm

outperforms when mineral dust particles are probed in the atmosphere. In elastic lidars (such as CALIOP), for the derivation of the aerosol extinction and -backscatter coefficients it is required a factor known as the lidar ratio.~~In elastic lidars (such as CALIOP), for the derivation of the aerosol extinction coefficient from the backscatter coefficient, it is required a factor known as lidar ratio.~~ For dust aerosols, the lidar ratio is set to 44 sr in the CALIPSO aerosol retrieval algorithm and is constant worldwide. However, ground-based lidar measurements acquired at different places of the world have shown that the dust LR varies in space and time.

Driven by this fact, in the present study we focus on the estimation of the dust LRs over North Africa and Middle East, encompassing the most active dust sources of the planet. Our analysis relies on a synergistic approach by combining CALIPSO vertical dust profiles (a set of strict criteria has been implemented to ensure the presence of only mineral dust) with quality-assured columnar passive aerosol retrievals derived from the MIDAS dataset (MODIS-based) and the POLDER-3/GRASP satellite observations. All spaceborne instruments are/were part of the A-Train constellation thus enabling coincident observations. The study period covers a 12-year period of CALIPSO overpasses, spanning from June 2006 to December 2017. We have calculated the updated (revised) dust LRs within the study domain by collocating: (i) CALIOP-POLDER-3/GRASP during the period 2006-2009, (ii) CALIOP-MIDAS during the period 2007-2017 and (iii) CALIOP-MIDAS, on a seasonal basis, over the period 2007-2017.

The dust LR maps produced display a significant spatial variability over both North Africa and in the Middle East. According to our findings, the highest dust LRs are recorded over and near the Bodélé Depression in the northern Chad basin (values up to 5~~3~~6.2~~3.4~~ sr), over the Libyan desert (~48–5~~2~~6 sr) and over dust-affected areas eastwards of the Caspian Sea (47–5~~5~~6 sr). Across the Arabian Peninsula, the adjusted dust LR values exhibit pronounced spatial variability, with lower values (~38–45 sr) over the central and southern regions and locally higher values (~46–54 sr) toward the northern Arabian Peninsula and Mesopotamia; overall, most of these values remain at or below the default CALIPSO dust LR of 44 sr. For clarity, a spatially smoothed representation of the dust LR map from CALIOP-MIDAS synergy is shown in Fig. 9, highlighting the dominant regional patterns discussed above. ~~Over the Arabian Peninsula, the adjusted dust LRs range from 40 to 44 sr and are mostly lower than the default (standard) value (44 sr). This outcome is consistent with the findings reported in other studies. The major difference between the CALIOP-POLDER and CALIOP-MIDAS synergies is that the latter highlights higher LR values over central Asia, particularly over the Karakum and Kyzylkum deserts, which are less pronounced in the CALIOP-POLDER results.~~ Based on the CALIOP-MIDAS synergy on a seasonal basis, it is found that the highest dust LRs are obtained in ~~summer~~JJA, while the lowest ones are recorded in ~~winter~~DJF, indicating that the proposed adjustments follow the dust optical depth seasonal cycle. In addition to the dust LR maps, the associated uncertainty fields further reinforce the robustness of the retrieved regional patterns. Over the Central Sahara and Central Asian domains, the total LR uncertainties remain relatively low (typically ~2–5 sr), reflecting both limited retrieval variability in the daily LR estimates and the sufficiently large number of dust cases contributing to the grid-cell averages. In contrast, higher uncertainties—locally reaching ~8–11 sr—emerge primarily over parts of the Central Asia (e.g. Iran). These enhanced uncertainties arise from the combined effect of larger

retrieval uncertainties in these regions and the reduced number of cases, which amplifies the standard-error component of the total uncertainty, particularly in locations where only 2–3 dust cases are available. ~~The latter amplifies the standard-error component of the total uncertainty, particularly in locations where only 2–3 dust cases are available.~~ Moreover, the elevated uncertainties over selected Middle Eastern and Central Asian regions likely reflect the convergence of dust plumes from different source regions and the resulting mixing of ~~mineralogically~~mineralogical distinct dust types, as well as potential aerosol-type misclassification in CALIPSO retrievals. Similar effects may also arise over Sahel, where occasional misclassified smoke layers transported from Central African biomass-burning areas can introduce additional variability in the retrieved LR values. Taken together, the uncertainty patterns indicate that, while elevated uncertainties may influence the LR estimates in some regions, the broader spatial differences identified in the dust LR maps are not primarily artifacts of retrieval noise or sampling limitations, but instead reflect physically meaningful variability in dust optical properties across North Africa, the Middle East, and Central Asia. ~~In order to evaluate our methodology, we have identified 135 cases where pure dust loads are probed by CALIOP in the surrounding area (<100 km) of 9 AERONET stations. The updated dust LR yielded better evaluation metrics against AERONET stations in comparison with the CALIPSO~~CALIPSO ~~default LR, in terms of the mean bias error (MBE) and the root mean square error (RMSE). In particular, the best improvements were recorded over Karachi, Masdar Institute and Mezaira, with each synergy (combination) performing better or worse over the different stations, while the deviations from the DOD based on the CALIPSO default LR were more significant over stations where the LR showed a notable decrease or increase from the default value of 44 sr.~~

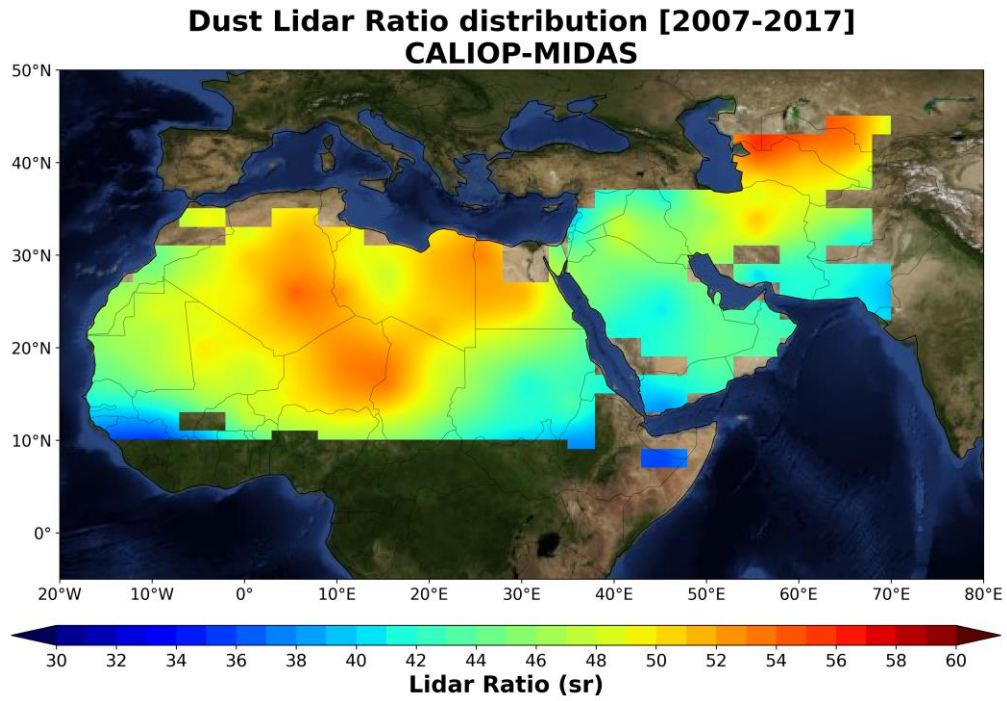

Figure 9: Geographical distribution of the mean dust lidar ratio (LR) derived from the CALIOP–MIDAS synergy for the period 2007–2017. The underlying LR values are computed at each 2° × 5° predefined grid cell, while a spatially smoothed representation is shown to emphasize large-scale regional patterns. Only grid cells with more than one dust case contribute to the displayed field. Map source: NASA Earth Observatory.

~~**Figure 8: Summary of regional dust lidar ratio (LR) statistics at 532 nm derived from the two CALIOP-based synergies used in this study. The table (top) reports the mean dust LR and its total uncertainty (LR ± σ) for the 10 desert sub-regions defined in Fig. 1, separately for the CALIOP–MIDAS synergy (2007–2017) and the CALIOP–POLDER-3/GRASP synergy (2006–2009). The map (bottom) illustrates the spatial extent of the 10 sub-regions: Central Sahara (CS), Western Outflow Zone (WOZ), Northwestern Sahara (NWS), Northeastern Sahara (NES), Western Sahara (WS), Eastern Sahara (ES), Central Asia (CA), Northern Arabian Peninsula (NAP), Central Arabian Peninsula (CAP), and Southern Arabian Peninsula (SAP). Map source: NASA Earth Observatory.**~~

~~At the final stage of the analysis, it has been assessed the effect of the upgraded dust LRs on the climatological DODs. By implementing the calculated dust LRs, the spatiotemporal DOD patterns are significantly modified compared to those produced by considering the default LR. According to the standard CALIPSO aerosol scheme, DODs are maximized (up to 0.5) over the western Sahara and in Saudi Arabia, while similar levels are recorded along the coasts of Iran and in the southern Pakistan. Based on the revised dust LRs, in North Africa, a distinct zone of elevated DODs reaching values of up to 0.6, extends from Mauritania to Chad, spanning the latitudinal range of 10° N to 25° N. This zone is consistently observed across all synergies between active (CALIPSO) and passive (POLDER-3/MODIS) spaceborne instruments. Within this region, two prominent hotspots of maximum DODs are identified, one located in the Mali-Mauritania area and the other in the Niger-Chad region. In~~

~~Saudi Arabia, the implementation of the adjusted dust LRs results in more heterogeneous DOD fields in comparison to the default CALIPSO retrieval algorithm. In summary, our findings suggest that the revised dust LRs lead to an increase in the intensity of dust loads across North Africa (maximized over/nearby the major dust sources) while declining DOD tendencies are found in the Arabian Peninsula. Furthermore, a narrow transition zone of neutral DOD declinations (using the default CALIPSO DODs as reference) between North Africa and the Arabian Peninsula is obtained from the CALIOP–MIDAS synergy. Finally, the revised dust LRs increase the DOD over regions east of the Caspian Sea, contrary to what has been found in Iran, Afghanistan and Pakistan.~~

The summary table of regional dust LR values (Table 2), estimated following Eq. (13), provides a compact overview of the spatial differences identified by the two CALIOP-based synergies across ten sub-regions defined within the broader desert domains (Fig. 10) over the most active and representative dust-producing areas. ~~The summary table of regional dust LR values (Fig. 8) provides a compact overview of the spatial differences identified by the two CALIOP-based synergies.~~ Over North Africa regions, the CALIOP–MIDAS and CALIOP–POLDER-3/GRASP synergies yield nearly identical regional LR values (typically 45–53 sr), underscoring the strong consistency between the two datasets across the major Saharan source regions. Across the broader Middle East domain, the regional dust LR values are relatively consistent, clustering around ~45 sr. Pronounced differences ~~between the two synergies~~between the two synergies arise across the Arabian Peninsula. The CALIOP–POLDER-3/GRASP synergy lead to LR values greater than 44 sr across all Arabian sub-regions, whereas the CALIOP–MIDAS synergy yields somewhat lower values over the central and southern Peninsula. This discrepancy may partly reflect the much more limited temporal sampling of the CALIOP-POLDER-3/GRASP synergy (2006–2009), but also differences in sensor characteristics and retrieval assumptions. Importantly, the uncertainties associated with the CALIOP-POLDER-3/GRASP LR estimates are substantially larger—~~up to~~up to ~50% relative to CALIOP-MIDAS—such that the two synergies exhibit considerable overlap within their uncertainty ranges. This suggests that, despite the apparent regional differences, the two datasets remain broadly consistent once retrieval uncertainty is taken into account.

Table 2: Summary of regional dust lidar ratio (LR) statistics at 532 nm derived from the two CALIOP-based synergies used in this study. The table reports the mean dust LR and its total uncertainty (LR ± σ) for 10 desert subregions (defined in Fig. 10), separately for the CALIOP–MIDAS synergy (2007–2017) and the CALIOP–POLDER-3/GRASP synergy (2006–2009).

Regions	Geographical boundaries	Dust LR ± σ (sr)	
		CALIOP-MIDAS	CALIOP-POLDER-3/GRASP
North Africa		49.3 ± 2.7	50.3 ± 4.3
Central Sahara (CS)	13°–21° N, 8°–18° E	53.5 ± 1.9	52.2 ± 3.7
Northwestern Sahara (NWS)	27°–33° N, 2° W–13° E	50.8 ± 3.3	51.2 ± 5.4
Northeastern Sahara (NES)	25°–31° N, 18°–28° E	52.0 ± 2.4	52.4 ± 3.7
Western Sahara (WS)	15°–25° N, 7° W–3° E	49 ± 2.0	49.7 ± 3.5
Eastern Sahara (ES)	17°–23° N, 28°–38° E	45.6 ± 2.5	48.6 ± 3.6
Western Outflow Zone (WOZ)	13°–25° N, 17° W–12° W	45.5 ± 2.6	45.7 ± 3.5

Middle East		45.6 ± 3.6	45.4 ± 5.1
Northern Arabian Peninsula (NAP)	27.2°–35° N, 38°–48° E	47.8 ± 3.1	46.3 ± 3.6
Central Arabian Peninsula (CAP)	23.2°–26.6° N, 38°–53° E	43.3 ± 4.3	48.1 ± 5.5
Southern Arabian Peninsula (SAP)	17°–22.8° N, 43°–58° E	44.2 ± 2.6	46.6 ± 3.8
Central Asia (CA)	37°–43° N, 58°–68° E	50.2 ± 3.3	48.1 ± 5.3

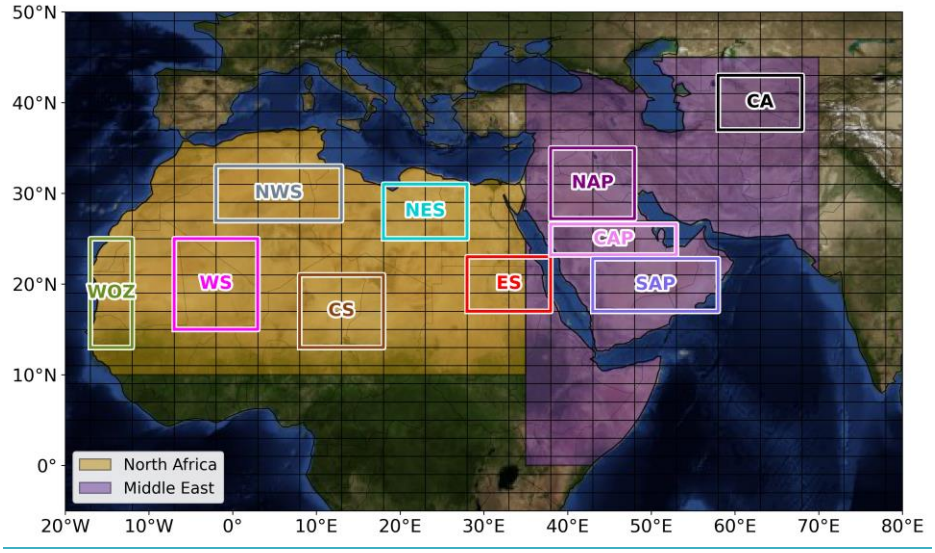

Figure 10: The spatial extent of the 10 sub-regions used in Table 2: Central Sahara (CS), Western Outflow Zone (WOZ), Northwestern Sahara (NWS), Northeastern Sahara (NES), Western Sahara (WS), Eastern Sahara (ES), Central Asia (CA), Northern Arabian Peninsula (NAP), Central Arabian Peninsula (CAP), and Southern Arabian Peninsula (SAP). Map source: NASA Earth Observatory.

~~This study focuses on a dynamic (in terms of space and time) estimation of the dust lidar ratio over the most active deserts globally, via a synergistic approach involving active (CALIPSO-CALIOP) and passive (MIDAS and POLDER-3) spaceborne retrievals. Our approach involves an adjustment of dust LRs to optimize the agreement between the CALIOP and the columnar DODs derived by passive sensors. However, it is important to note that in elastic lidars (e.g., CALIOP), the assumption of lidar ratio is already embedded in the retrieval of the backscatter coefficient is retrieved (Klett, 1981; Fernald, 1984). This aspect has not been considered in the current study. Based on our theoretical simulations, it has been found that under intense dust loads (DOD = 1.0), this limitation can introduce an error of up to 10% in the backscatter coefficient in the lower atmosphere (<1 km). Although this level of error does not affect substantially the robustness of our approach, further refinement of our methodology is planned for future studies. Moreover, ….~~[AG11]

Our research aims to enhance the efficacy of CALIPSO dust retrievals, thereby increasing their utility in a broad range of scientific studies. The analysis performed here can be extended to other major desert regions in the Northern Hemisphere (e.g., the Taklamakan Desert), as well as to the geographically more limited and less active dust source areas in the Southern Hemisphere. Moreover, the proposed methodology is not restricted to dust: it can be readily applied to all CALIPSO aerosol

subtypes, such as marine aerosols, provided the analysis is focused on regions where different aerosol species dominate (e.g., clean marine over oceanic regions, polluted continental/smoke or elevated smoke over Central Africa, etc.). This flexibility highlights the broader applicability of our approach for refining CALIPSO aerosol optical retrievals across diverse environments. ~~Our research aims to enhance the efficacy of CALIPSO dust retrievals, thereby increasing their utility in a broad range of scientific studies. The analyses performed can be extended to other large deserts in the northern hemisphere (e.g. Taklamakan), as well as to the geographically limited and less active dust sources in the southern hemisphere.~~ In a follow-up study, we will investigate the dust-induced direct radiative effects based on radiative transfer model (RTM) simulations. This will involve the use of updated CALIPSO dust profiles, the intensive spectral optical properties (including single scattering albedo, asymmetry parameter, and refractive index) obtained by the GRASP/POLDER-3 retrieval algorithm for the identified dust cases, along with the spectral surface albedos sourced from the HAMSTER dataset (Roccetti et al., 2024). Given the strong dependence of dust LRs on the composition of the mineral particles (Ansmann and Müller, 2005), the incorporation of the mineralogical maps derived by the EMIT instrument (Connelly et al., 2021; Coleman et al., 2024) will strengthen the interpretation of the outcomes obtained in the current study. ~~One of the challenging tasks encountered in our analysis was the assessment of the proposed adjustments to the default CALIPSO dust lidar ratio. Due to the scarcity of ground-based measurements within the study region, the evaluation was limited to the vicinity of a few AERONET stations.~~ A future assessment and validation of our findings will be possible through comparison with the vertically resolved lidar ratio observations to be provided by the ATLID lidar onboard the EarthCARE satellite (Illingworth et al., 2015; Wandinger et al., 2023; Wehr et al., 2023). Finally, one of the key updates in the forthcoming CALIPSO Version 5 retrieval algorithm involves the adoption of new aerosol models for lidar ratio estimation, further highlighting the need for an improved and regionally representative characterization of this critical parameter.~~A better justification and refinement of our calculations will be achieved via the incorporation of the vertically resolved lidar ratio observations acquired by the ATLID lidar, onboard the EarthCARE satellite (Illingworth et al., 2015; Wehr et al., 2023). Finally, among the major improvements to be implemented in the upcoming CALIPSO retrieval algorithm (Version 5), one is related to the use of new aerosol models for the estimation of the lidar ratio, underscoring the necessity for a more accurate representation of this critical parameter.~~

Data availability. The LIVAS dust products are available upon request from Vassilis Amiridis (vamoir@noa.gr), Emmanouil Proestakis (proestakis@noa.gr), and/or Eleni Marinou (elmarinou@noa.gr). The MIDAS dataset has been developed in the framework of the DUST-GLASS project (grant no. 749461; European Union's Horizon 2020 research and innovation program under the Marie Skłodowska-Curie Actions) and is available at https://doi.org/10.5281/zenodo.4244106 (Gkikas et al., 2020). The POLDER-3/GRASP Components products are publicly available at the GRASP-OPEN website (https://www.grasp-open.com/products/polder-data-release/). The Aerosol Robotic Network (AERONET) data are publicly available and can be accessed through the official website at: https://aeronet.gsfc.nasa.gov/. The annual and seasonal gridded dust Lidar Ratio (LR)

dataset resulted via the different synergies (CALIOP-POLDER-3/GRASP and CALIOP-MIDAS) over North Africa and the Middle East is available at https://doi.org/10.5281/zenodo.18016524 (Moustaka et al., 2025).

Author contributions. Conceptualization, A.M., N.S., ~~and~~ A.G.; methodology, A.M., N.S., A.G., S.K., V.A.; software, A.M., N.S.; ~~validation, A.M., N.S., E.P. and A.G.;~~ writing—original draft preparation, A.M; writing—review and editing, A.M., A.G., N.S., K.A.V., E.P., A.L., S.K., O.D., K.T., C.Z., V.A.; funding acquisition, A.G., S.K. All authors have read and agreed to the published version of the manuscript.

Financial support. This work was supported both from COST Action CA21119 Harmonia: International network for harmonisation of atmospheric aerosol retrievals from ground based photometers, supported by COST (European Cooperation in Science and Technology) and the Hellenic Foundation for Research and Innovation (H.F.R.I.) under the "2nd Call for H.F.R.I. Research Projects to support Post-Doctoral Researchers" (Project Number: 544)

Acknowledgment. We want to ~~are grateful to AERONET for providing high-quality sun-photometer observations, calibrations, and products. Special thanks to the Principal Investigators and Co-Investigators of the AERONET stations used in this study: Philippe Goloub (Agoufou), Didier Tanré, Jean-Louis Rajot (Banizoumbou), Gilles Bergametti (Medenine-IRA), Jean-Louis Rajot, Mahammadou M. Zakari (Zinder Airport), Pawan Gupta, Elena Lind, Muhammad Ateeq Quershi (Karachi), Matteo Chiesa (Masdar Institute), Pawan Gupta, Elena Lind (Mezaira & Solar Village), and Alaa Ismail (Shagaya Park).~~ acknowledge the use of POLDER data "POLDER/PARASOL Level-1 data originally provided by CNES (http://www.icare.univ-lille1.fr/) and AERIS/ICARE Data and Services Center, processed by Cloudflight Austria GmbH with GRASP software (https://www.grasp-open.com) developed by Dubovik et al. (2011, 2014, 2021) and Li et al. (2019). This study benefited from contributions made within the AIRSENSE (Aerosol and aerosol cloud Interaction from Remote SENSing Enhancement) project, funded by the European Space Agency under Contract No. 4000142902/23/I-NS. This project also received funding from the European Union's Horizon 2020 research and innovation programme under grant agreement No. 871115. ACTRIS-D is funded by the German Federal Ministry for Education and Research (BMBF) under grant agreements 01LK2001A-K and 01LK2002A-G. Stelios Kazadzis, would like to acknowledge the ACTRIS Switzerland 2025–2028 grant (Swiss contribution to the ACTRIS ERIC) funded by the Swiss State Secretariat for Education and Research and Innovation (SERI).~~We are grateful to AERONET for providing high-quality sun-photometer observations, calibrations, and products. Special thanks to the Principal Investigators and Co-Investigators of the AERONET stations used in this study: Philippe Goloub (Agoufou), Didier Tanré, Jean-Louis Rajot (Banizoumbou), Gilles Bergametti (Medenine-IRA), Jean-Louis Rajot, Mahammadou M. Zakari (Zinder Airport), Pawan Gupta, Elena Lind, Muhammad Ateeq Quershi (Karachi), Matteo Chiesa (Masdar Institute), Pawan Gupta, Elena Lind (Mezaira & Solar Village), and Alaa Ismail (Shagaya Park).~~We are grateful to AERONET for providing high-quality sun-photometer observations, calibrations, and products.~~

We would like also to acknowledge the use of POLDER data "POLDER/PARASOL Level-1 data originally provided by CNES (http://www.icare.univ-lille1.fr/) and AERIS/ICARE Data and Services Center, processed by Cloudflight

Austria GmbH with GRASP software (https://www.grasp-open.com) developed by Dubovik et al. (2011, 2014, 2021) and Li et al. (2019).

This study also benefited from contributions made in the framework of the AIRSENSE (Aerosol and aerosol cloud Interaction from Remote SENSing Enhancement) project, funded by the European Space Agency under Contract No. 4000142902/23/I-NS.
This project receives funding from the European Union's Horizon 2020 research and innovation programme under grant agreements No 871115. ACTRIS-D is funded by the German Federal Ministry for Education and Research (BMBF) under grant agreements 01LK2001A-K & 01LK2002A-G.

Competing interests. Some authors are members of the editorial board of AMT. V. Amiridis is in the editorial board of AMT and coordinating the special issue that the paper is submitted.

Disclaimer.

Special issue statement.

References

Ahmady-Birgani, H., Engelbrecht, J. P., and Bazgir, M.: How different source regions across the Middle East change aerosol and dust particle characteristics, Desert, 24, 61-73, doi:10.22059/jdesert.2019.72441, 2019.

Al-Hemoud, A., Al-Dashti, H., Al-Saleh, A., Petrov, P., Malek, M., Elhamoud, E., Karam, R., Al-Khatib, L., Alyahya, M., Al-Azemi, H., Al-Mutairi, N., Moulton, J., and Middleton, N.: Dust storm 'hot spots' and transport pathways affecting the Arabian Peninsula. Journal of Atmospheric and Solar-Terrestrial Physics, 238, 105932, doi:10.1016/j.jastp.2022.105932, 2022.

Althausen, D., Abdullaev, S., and Hofer, J.: Scientists share results of dust belt research, EOS, Science News by AGU, 100, doi:10.1029/2019EO131683, 2019.

Amiridis, V., Wandinger, U., Marinou, E., Giannakaki, E., Tsekeri, A., Basart, S., Kazadzis, S., Gkikas, A., Taylor, M., Baldasano, J., and Ansmann, A.: Optimizing CALIPSO Saharan dust retrievals, Atmos. Chem. Phys., 13, 12089–12106, doi:10.5194/acp-13-12089-2013, 2013.

Amiridis, V., Marinou, E., Tsekeri, A., Wandinger, U., Schwarz, A., Giannakaki, E., Mamouri, R., Kokkalis, P., Binietoglou, I., Solomos, S., Herekakis, T., Kazadzis, S., Gerasopoulos, E., Proestakis, E., Kottas, M., Balis, D., Papayannis, A., Kontoes, C., Kourtidis, K., Papagiannopoulos, N., Mona, L., Pappalardo, G., Le Rille, O., and Ansmann, A.: LIVAS: a 3-D multi-wavelength aerosol/cloud database based on CALIPSO and EARLINET, Atmos. Chem. Phys., 15, 7127–7153, doi:10.5194/acp-15-7127-2015, 2015.

Anderson, T. L., Wu, Y., Chu, D. A., Schmid, B., Redemann, J., and Dubovik, O.: Testing the MODIS satellite retrieval of aerosol fine-mode fraction, J. Geophys. Res., 110, D18204, doi:10.1029/2005JD005978, 2005.

ÅAngström, A.: On the atmospheric transmission of Sun radiation and on dust in the air, Geogr. Ann., 11, 156–166, doi:10.2307/519399, 1929.

Ansmann, A. and Müller, D.: Lidar and atmospheric aerosol particles, in: Lidar– Range-Resolved Optical Remote Sensing of the Atmosphere, vol. 102 of Springer Series in Optical Sciences, edited by: Weitkamp, C., Springer, Berlin, Heidelberg, 105–141, 2005.

Ansmann, A., Petzold, A., Kandler, K., Tegen, I., Wendisch, M., Müller, D., Weinzierl, B., Müller, T., and Heintzenberg, J.: Saharan Mineral Dust Experiments SAMUM–1 and SAMUM–2: what have we learned?, Tellus B, 63, 403–429, doi:10.1111/j.1600 0889.2011.00555.x, 2011.

Baars, H., Kanitz, T., Engelmann, R., Althausen, D., Heese, B., Komppula, M., Preissler, J., Tesche, M., Ansmann, A., Wandinger, U., Lim, J. H., Ahn, J. Y., Stachlewska, I. S., Amiridis, V., Marinou, E., Seifert, P., 97 Hofer, J., Skupin, A., Schneider, F., Bohlmann, S., Foth, A., Bley, S., Pfuller, A., Giannakaki, E., Lihavainen, H., Viisanen, Y., Hooda, R. K., Pereira, S. N., Bortoli, D., Wagner, F., Mattis, I., Janicka, L., Markowicz, K. M., Achtert, P., Artaxo, P., Pauliquevis, T., Souza, R. A. F., Sharma, V. P., van Zyl, P. G., Beukes, J. P., Sun, J. Y., Rohwer, E. G., Deng, R. R., Mamouri, R. E., and Zamorano, F.: An overview of the first decade of Polly(NET): an emerging network of automated Raman-polarization lidars for continuous aerosol profiling, Atmos. Chem. Phys., 16, 5111–5137, doi:10.5194/acp--16-5111-2016, 2016.

Banks, J. R., Heinold, B., and Schepanski, K.: Impacts of the desiccation of the Aral Sea on the Central Asian dust life-cycle. J. Geophys. Res.: Atmos., 127, doi:10.1029/2022JD036618, 2022.

Benkhalifa, J., Leon, J. F., and Chaabane, M.: Aerosol optical properties of Western Mediterranean basin from multi-year AERONET data, J. Atmos. Sol.-Terr. Phy., 164, 222–228, doi:-10.1016/j.jastp.2017.08.029, 2017.

Bhattarai, S. and Talchabhadel, R.: Comparative Analysis of Satellite-Based Precipitation Data across the CONUS and Hawaii: Identifying Optimal Satellite Performance. Remote Sens., 16, 3058, doi: 10.3390/rs16163058, 2024.

Bohlmann, S., Baars, H., Radenz, M., Engelmann, R., and Macke, A.: Ship-borne aerosol profiling with lidar over the Atlantic Ocean: from pure marine conditions to complex dust–smoke mixtures, Atmos. Chem. Phys., 18, 9661–9679, doi:10.5194/acp-18-9661-2018, 2018.

Burton, S. P., Ferrare, R. A., Hostetler, C. A., Hair, J. W., Rogers, R. R., Obland, M. D., Butler, C. F., Cook, A. L., Harper, D. B., and Froyd, K. D.: Aerosol classification using airborne High Spectral Resolution Lidar measurements – methodology and examples, Atmos. Meas. Tech., 5, 73–98, doi:10.5194/amt-5-73-2012, 2012.

Burton, S. P., Ferrare, R. A., Vaughan, M. A., Omar, A. H., Rogers, R. R., Hostetler, C. A., and Hair, J. W.: Aerosol classification from airborne HSRL and comparisons with the CALIPSO vertical feature mask, Atmos. Meas. Tech., 6, 1397–1412, doi:10.5194/amt-6-1397-2013, 2013.

Caquineau, S., Gaudichet, A., Gomes, L., and Legrand, M.: Mineralogy of Saharan dust transported over northwestern tropical Atlantic Ocean in relation to source regions, J. Geophys. Res., 107, 4251, doi:10.1029/2000jd000247, 2002.

Castellanos, P., Colarco, P., Espinosa, W. R., Guzewich, S. D., Levy, R. C., Miller, R. L., Chin, M., Kahn, R. A., Kemppinen, O., Moosmüller, H., Nowottnick, E. P., Rocha-Lima, A., Smith, M. D., Yorks, J. E., and Yu, H.: Mineral dust optical properties for remote sensing andglobal modeling: A review, Remote Sens.Environ., 303, 113982, doi:10.1016/j.rse.2023.113982, 2024.

Chen, C., Dubovik, O., Fuertes, D., Litvinov, P., Lapyonok, T., Lopatin, A., Ducos, F., Derimian, Y., Herman, M., Tanré, D., Remer, L. A., Lyapustin, A., Sayer, A. M., Levy, R. C., Hsu, N. C., Descloitres, J., Li, L., Torres, B., Karol, Y., Herrera, M., Herreras, M., Aspetsberger, M., Wanzenboeck, M., Bindreiter, L., Marth, D., Hangler, A., and Federspiel, C.: Validation of GRASP algorithm product from POLDER/PARASOL data and assessment of multi-angular polarimetry potential for aerosol monitoring, Earth Syst. Sci. Data, 12, 3573–3620, doi:10.5194/essd-12-3573-2020, 2020.

Chen, S., Jiang, N., Huang, J., Xu, X., Zhang, H., Zang, Z., Huang, K., Xu, X., Wei, Y., Guan, X., Zhang, X., Luo, Y., Hu, Z., and Feng, T.: Quantifying contributions of natural and anthropogenic dust emission from different climatic regions, Atmos. Environ., 191, 94–104, doi:10.1016/j.atmosenv.2018.07.043, 2018.

Cole, J. N. S., Barker, H. W., Qu, Z., Villefranque, N., and Shephard, M. W.: Broadband radiative quantities for the EarthCARE mission: the ACM-COM and ACM-RT products, Atmos. Meas. Tech., 16, 4271–4288, doi:10.5194/amt-16-4271-2023, 2023.

Coleman, R. W., Thompson, D. R., Brodrick, P. G., Dor, E. B., Cox, E., García-Pando, C. P., Hoefen, T., Kokaly, R. F., Meyer, J. M., Ochoa, F., Okin, G. S., Pearlshtien, D. H., Swayze, G., and Green, R. O.: An accuracy assessment of the surface reflectance product from the EMIT imaging spectrometer. Remote Sens. Environ., 315, 114450, doi: 10.1016/j.rse.2024.114450, 2024.

Connelly, D. S., Thompson, D. R., Mahowald, N. M., Li, L., Carmon, N., Okin, G. S., and Green, R. O.: The EMIT mission information yield for mineral dust radiative forcing. Remote Sens. Environ., 258, 112380, doi:-10.1016/j.rse.2021.112380, 2021.

Deshler, T., Johnson, B. J., and Rozier, W. R.: Balloonborne measurements of Pinatubo aerosol during 1991 and 1992 at 41◦ N: vertical profiles, size distribution, and volatility, Geophys. Res. Lett., 20, 1435–1438, doi:10.1029/93GL01337, 1993.

Dubovik, O. and King, M. D.: A flexible inversion algorithm for retrieval of aerosol optical properties from Sun and sky radiance measurements, J. Geophys. Res.-Atmos., 105, 20673–20696, doi:10.1029/2000JD900282, 2000.

Dubovik, O., Sinyuk, A., Lapyonok, T., Holben, B. N., Mishchenko, M., Yang, P., Eck, T. F., Volten, H., Muñoz, O., Veihelmann, B., van der Zande, W. J., Leon, J. F., Sorokin, M., and Slutsker, I.: Application of spheroid models to account for aerosol particle nonsphericity in remote sensing of desert dust, J. Geophys. Res.-Atmos., 111, 1–34, doi:10.1029/2005JD006619, 2006.

Dubovik, O., Herman, M., Holdak, A., Lapyonok, T., Tanré, D., Deuzé, J. L., Ducos, F., Sinyuk, A., and Lopatin, A.: Statistically optimized inversion algorithm for enhanced retrieval of aerosol properties from spectral multi-angle polarimetric satellite observations, Atmos. Meas. Tech., 4, 975–1018, doi:10.5194/amt-4-975-2011, 2011.

Dubovik, O., Schuster, G. L., Xu, F., Hu, Y., Bösch, H., Landgraf, J., and Li, Z.: Grand Challenges in Satellite Remote Sensing, Front. Remote Sens., 2, 1–10, doi:10.3389/frsen.2021.619818, 2021.

Elguindi, N., Solmon, F., and Turuncoglu, U.: Quantifying some of the impacts of dust and other aerosol on the Caspian Sea region using a regional climate model, Clim. Dynam, 46, 41–55, 2016.

Engelstaedter, S., Tegen, I., and Washington, R.: North African dust emissions and transport, Earth-Sci. Rev., 79, 73–100, doi:10.1016/j.earscirev.2006.06.004, 2007.

Eom,S., Kim, J.; Lee, S., Holben, B.N., Eck, T.F., Park, S.B., and Park, S.S.: Long-term variation of aerosol optical properties associated with aerosol types over East Asia using AERONET and satellite (VIIRS, OMI) data (2012–2019). Atmos. Res., 280, 106457, doi:10.1016/j.atmosres.2022.106457, 2022.

Filioglou, M., Giannakaki, E., Backman, J., Kesti, J., Hirsikko, A., Engelmann, R., O'Connor, E., Leskinen, J. T. T., Shang, X., Korhonen, H., Lihavainen, H., Romakkaniemi, S., and Komppula, M.: Optical and geometrical aerosol particle properties over the United Arab Emirates, Atmos. Chem. Phys., 20, 8909–8922, doi:10.5194/acp-20-8909-2020, 2020.

Floutsi, A. A., Baars, H., Engelmann, R., Althausen, D., Ansmann, A., Bohlmann, S., Heese, B., Hofer, J., Kanitz, T., Haarig, M., Ohneiser, K., Radenz, M., Seifert, P., Skupin, A., Yin, Z., Abdullaev, S. F., Komppula, M., Filioglou, M., Giannakaki, E., Stachlewska, I. S., Janicka, L., Bortoli, D., Marinou, E., Amiridis, V., Gialitaki, A., Mamouri, R.-E., Barja, B., and Wandinger, U.: DeLiAn – a growing collection of depolarization ratio, lidar ratio and Ångström exponent for different aerosol types and mixtures from ground-based lidar observations, Atmos. Meas. Tech., 16, 2353–2379, doi:10.5194/amt-16-2353-2023, 2023.

Fountoulakis, I., Kosmopoulos, P., Papachristopoulou, K., Raptis, I.-P., Mamouri, R.-E., Nisantzi, A., Gkikas, A., Witthuhn, J., Bley, S., Moustaka, A., Buehl, J., Seifert, P., Hadjimitsis, D., Kontoes, C., and Kazadzis, S.: Effects of Aerosols and Clouds on the Levels of Surface Solar Radiation and Solar Energy in Cyprus, Remote Sens., 13, 2319, doi:10.3390/rs13122319, 2021.

Fountoulakis, I., Papachristopoulou, K., Proestakis, E., Amiridis, V., Kontoes, C., and Kazadzis, S.: Effect of Aerosol Vertical Distribution on the Modeling of Solar Radiation, Remote Sensing, 14, 1143, doi:10.3390/rs14051143, 2022.

Freudenthaler, V., Esselborn, M., Wiegner, M., Heese, B., Tesche, M., Ansmann, A., Müller, D., Althausen, D., Wirth, M., Fix, A., Ehret, G., Knippertz, P., Toledano, C., Gasteiger, J., Garhammer, M., and Seefeldner, M.: Depolarization ratio prof iling at several wavelengths in pure Saharan dust during SAMUM 2006, Tellus B, 61, 165–179, doi:10.1111/j.16000889.2008.00396.x, 2009.

Ge, J. M., Huang, J. P., Xu, C. P., Qi, Y. L., and Liu, H. Y.: Charac teristics of Taklimakan dust emission and distribution: a satellite and reanalysis field perspective, J. Geophys. Res.-Atmos., 119, 11772–11783, doi:10.1002/2014JD022280, 2014.

Gelaro, R., McCarty, W., Suárez, M. J., Todling, R., Molod, A., Takacs, L., Randles, C. A., Darmenov, A., Bosilovich, M. G., Reichle, R., Wargan, K., Coy, L., Cullather, R., Draper, C., Akella, S., Buchard, V., Conaty, A., da Silva, A. M., Gu, W., Kim, G.-K., Koster, R., Lucchesi, R., Merkova, D., Nielsen, J. E., Partyka, G., Pawson, S., Putman, W., Rienecker, M., Schubert, S. D., Sienkiewicz, M., and Zhao, B.: The modern-era retrospective analysis for research and applications, version 2 (MERRA-2), Journal of Climate, 30(14), 5419–5454, doi:10.1175/JCLI-D-16-0758.1, 2017.

Giles, D. M., Sinyuk, A., Sorokin, M. G., Schafer, J. S., Smirnov, A., Slutsker, I., Eck, T. F., Holben, B. N., Lewis, J. R., Campbell, J. R., Welton, E. J., Korkin, S. V., and Lyapustin, A. I.: Advancements in the Aerosol Robotic

Network (AERONET) Version 3 database – automated near-real-time quality control algorithm with improved cloud screening for Sun photometer aerosol optical depth (AOD) measurements, Atmos. Meas. Tech., 12, 169–209, doi:10.5194/amt-12-169-2019, 2019.

Ginoux, P., Prospero, J. M., Gill, T. E., Hsu, N. C., and Zhao, M.: Global-scale attribution of anthropogenic and nat ural dust sources and their emission rates based on MODIS Deep Blue aerosol products, Rev. Geophys., 50, RG3005, doi:10.1029/2012RG000388, 2012.

Gkikas, A., Proestakis, E., Amiridis, V., Kazadzis, S., Di Tomaso, E., Tsekeri, A., Marinou, E., Hatzianastassiou, N., and Pérez García-Pando, C.: ModIs Dust AeroSol (MIDAS): A global fine resolution dust optical depth dataset, Zenodo, doi:10.5281/zenodo.4244106, 2020.

Gkikas, A., Proestakis, E., Amiridis, V., Kazadzis, S., Di Tomaso, E., Tsekeri, A., Marinou, E., Hatzianastassiou, N., and Pérez García-Pando, C.: ModIs Dust AeroSol (MIDAS): a global fine-resolution dust optical depth data set, Atmos. Meas. Tech., 14, 309–334, doi:10.5194/amt-14-309-2021, 2021.

Gkikas, A., Proestakis, E., Amiridis, V., Kazadzis, S., Di Tomaso, E., Marinou, E., Hatzianastassiou, N., Kok, J. F., and García-Pando, C. P.: Quantification of the dust optical depth across spatiotemporal scales with the MIDAS global dataset (2003–2017), Atmos. Chem. Phys., 22, 3553–3578, doi:10.5194/acp-22-3553-2022, 2022.

González-Romero, A., González-Flórez, C., Panta, A., Yus-Díez, J., Reche, C., Córdoba, P., Moreno, N., Alastuey, A., Kandler, K., Klose, M., Baldo, C., Clark, R. N., Shi, Z., Querol, X., and Pérez García-Pando, C.: Variability in sediment particle size, mineralogy, and Fe mode of occurrence across dust-source inland drainage basins: the case of the lower Drâa Valley, Morocco, Atmos. Chem. Phys., 23, 15815–15834, doi:10.5194/acp-23-15815-2023, 2023.

Groß, S., Tesche, M., Freudenthaler, V., Toledano, C., Wiegner, M., Ansmann, A., Althausen, D., and Seefeldner, M.: Characterization of Saharan dust, marine aerosols and mixtures of biomass-burning aerosols and dust by means of multi-wavelength depolarization and Raman lidar measurements during SAMUM–2, Tellus B, 63, 706–724, doi:10.1111/j.1600-0889.2011.00556.x, 2011.

Groß, S., Freudenthaler, V., Schepanski, K., Toledano, C., Schäfler, A., Ansmann, A., and Weinzierl, B.: Optical properties of long-range transported Saharan dust over Barbados as measured by dual-wavelength depolarization Raman lidar measurements, Atmospheric Chemistry and Physics, 15(19), 11067–11080, doi:10.5194/acp-15-11067-2015, 2015.

Gui, L., Tao, M., Wang, Y., Wang, L., Chen, L., Lin, C., Tao, J., Wang, J., and Yu, C.: Climatology of aerosol types and their vertical distribution over East Asia based on CALIPSO lidar measurements. Int. J. Climatol., 42, 6042–6054, doi:10.1002/joc.7599, 2022.

Gupta, P., Remer, L.A., Patadia, F., Levy, R.C., and Christopher, S.A.: High-resolution gridded level 3 aerosol optical depth data from MODIS. Remote Sens., 12, 2847, doi:10.3390/rs12172847, 2020.

Haarig, M., Ansmann, A., Althausen, D., Klepel, A., Groß, S., Freudenthaler, V., Toledano, C., Mamouri, R.-E., Farrell, D. A., Prescod, D. A., Marinou, E., Burton, S. P., Gasteiger, J., Engelmann, R., and Baars, H.: Triple-wavelength depolarization-

ratio profiling of Saharan dust over Barbados during SALTRACE in 2013 and 2014, Atmos. Chem. Phys., 17, 10767–10794, doi:10.5194/acp-17-10767-2017, 2017a.

Haarig, M., Ansmann, A., Gasteiger, J., Kandler, K., Althausen, D., Baars, H., Radenz, M., and Farrell, D. A.: Dry versus wet marine particle optical properties: RH dependence of depolarization ratio, backscatter, and extinction from multiwavelength lidar measurements during SALTRACE, Atmos. Chem. Phys., 17, 14199–14217, doi:10.5194/acp-17-14199-2017, 2017b.

Haarig, M., Ansmann, A., Baars, H., Jimenez, C., Veselovskii, I., Engelmann, R., and Althausen, D.: Depolarization and lidar ratios at 355, 532, and 1064 nm and microphysical properties of aged tropospheric and stratospheric Canadian wildfire smoke, Atmos. Chem. Phys., 18, 11847–11861, doi:10.5194/acp-18-11847-2018, 2018.

Haarig, M., Ansmann, A., Engelmann, R., Baars, H., Toledano, C., Torres, B., Althausen, D., Radenz, M., and Wandinger, U.: First triple wavelength lidar observations of depolarization and extinction-to-backscatter ratios of Saharan dust, Atmos. Chem. Phys., 22, 355–369, doi:10.5194/acp-22-355-2022, 2022.

~~Haarig, M., Ansmann, A., Gasteiger, J., Kandler, K., Althausen, D., Baars, H., Radenz, M., and Farrell, D. A.: Dry versus wet marine particle optical properties: RH dependence of depolarization ratio, backscatter, and extinction from multiwavelength lidar measurements during SALTRACE, Atmos. Chem. Phys., 17, 14199–14217, doi:10.5194/acp-17-14199-2017, 2017b.~~

Hamidi, M., Kavianpour, M. R., and Shao, Y.: Synoptic analysis of dust storms in the Middle East, Asia-Pacific, J. Atmos. Sci., 49, 279–286, doi:10.1007/s13143-013-0027-9, 2013.

Hansen, J., Rossow, W., Carlson, B., Lacis, A., Travis, L., Del Genio, A., Fung, I., Cairns, B., Mishchenko, M., and Sato, M.: Low-cost long-term monitoring of global cli mate forcings and feedbacks, Climatic Change, 31, 247–271, ~~doi:10.1007/BF01095149~~doi:10.1007/BF01095149, 1995.

Hofer, J., Ansmann, A., Althausen, D., Engelmann, R., Baars, H., Fomba, K. W., Wandinger, U., Abdullaev, S. F., and Makhmudov, A. N.: Optical properties of Central Asian aerosol relevant for spaceborne lidar applications and aerosol typing at 355 and 532 nm, Atmospheric Chemistry and Physics, 20(15), 9265–9280, doi:10.5194/acp-20-9265-2020, 2020.

Holben, B. N., Eck, T. F., Slutsker, I., Tanré, D., Buis, J. P., Setzer, A., Vermote, E., Reagan, J. A., Kaufman, Y., Nakajima, T., Lavenu, F., Jankowiak, I., and Smirnov, A.: AERONET– A federated instrument network and data archive for aerosol characterization, Remote Sens. Environ., 66, 1–16, doi:10.1016/S0034-4257(98)00031-5, 1998.

Holben, B. N., Tanre, D., Smirnov, A., Eck, T. F., Slutsker, I., Abuhassan, N., Newcomb, W. W., Schafer, J., Chatenet, B., Lavenue, F., Kaufman, Y., Vande Castle, J., Setzer, A., Markham, B., Clark, D., Frouin, R., Halthore, R., Karnieli, A., O'Neill, N. T., Pietras, C., Pinker, R. T., Voss, K., and Zibordi, G.: An emerging ground-based aerosol climatology: Aerosol optical depth from AERONET, J. Geophys. Res., 106, 12067–12097, doi:10.1029/2001JD900014, 2001.

Hu, Y., Winker, D., Vaughan, M., Lin, B., Omar, A., Trepte, C., Flittner, D., Yang, P., Sun, W., Liu, Z., Wang, Z., Young, S., Stamnes, K., Huang, J., Kuehn, R., Baum, B., and Holz, R.: CALIPSO/CALIOP Cloud Phase Discrimination Algorithm, J. Atmos. Ocean. Tech., 26, 2293–2309, doi:10.1175/2009JTECHA1280.1, 2009.

Hu, Z., Huang, J., Zhao, C., Bi, J., Jin, Q., Qian, Y., Leung, L. R., Feng, T., Chen, S., and Ma, J.: Modeling the contributions of Northern Hemisphere dust sources to dust outflow from East Asia, Atmos. Environ., 202, 234–243, doi:10.1016/j.atmosenv.2019.01.022, 2019.

Hu, Z., Huang, J., Zhao, C., Jin, Q., Ma, Y., and Yang, B.: Modeling dust sources, transport, and radiative effects at different altitudes over the Tibetan Plateau, Atmos. Chem. Phys., 20, 1507–1529, doi:10.5194/acp-20-1507-2020, 2020.

Huang, J. P., Wang, T. H., Wang, W. C., Li, Z. Q., and Yan, H. R.: Climate effects of dust aerosols over East Asian arid and semiarid regions, J. Geophys. Res.-Atmos., 119, 11398–11416, doi:-10.1002/2014JD021796, 2014.

Hyer, E. J., Reid, J. S., and Zhang, J.: An over-land aerosol opti cal depth data set for data assimilation by filtering, correction, and aggregation of MODIS Collection 5 optical depth retrievals, Atmos. Meas. Tech., 4, 379–408, doi:10.5194/amt-4 379-2011, 2011.

Illingworth, A. J., Barker, H. W., Beljaars, A., Ceccaldi, M., Chepfer, H., Cierbaux, N., Cole, J., Delanoë, J., Domenech, C., Donovan, D. P., Fukuda, S., Hirakata, M., Hogan, R. J., Huenerbein, A., Kolias, P., Kubota, T., Nakajima, T. Y., Nishizawa, T., Ohno, Y., Okamoto, H., Oki, R., Sato, K., Satoh, M., Shepherd, M. W., Velazques-Blazquez, A., Wandinger, U., Wehr, T., and van Zadelhoff, G.-J.: The EarthCARE satellite: The next step forward in global measurements of clouds, aerosols, precipitation, and radiation, B. Am. Meteorol. Soc., 96, 1311–1332,–, doi:10.1175/BAMS-D-12-00227.1, 2015.

Jish Prakash, P., Stenchikov, G., Kalenderski, S., Osipov, S., and Bangalath, H.: The impact of dust storms on the Arabian Peninsula and the Red Sea, Atmos. Chem. Phys., 15, 199–222, doi:10.5194/acp-15-199-2015, 2015.

Kaduk, C.: Characterization of the optical properties of complex aerosol mixtures observed with a multiwavelength–Raman polarization lidar during the 6-weeks BACCHUS campaign in Cyprus in spring 2015, MSc thesis, Leipzig University, https://www.tropos.de/fileadmin/user_upload/Institut/–Abteilungen/Fernerkundung/Daten_PDF/MA_Clara_Kaduk.pdf –(last access: 12 December 2024), 2017.

Kang,E., Park, S., Kim, M., Yoo, C., Im, J., Song, C.K.: Direct aerosol optical depth retrievals using MODIS reflectance data and machine learning over East Asia. Atmos. Environ., 309, 119951, doi:10.1016/j.atmosenv.2023.119951, 2023.

Kanitz, T., Ansmann, A., Engelmann, R., and Althausen, D.: North-south cross sections of the vertical aerosol distribution over the At lantic Ocean from multiwavelength Raman/polarization lidar during Polarstern cruises, J. Geophys. Res.-Atmos., 118, 2643–2655, doi:10.1002/jgrd.50273, 2013.

Kim, M.-H., Kim, S.-W., and Omar, A. H.: Dust Lidar Ratios Retrieved from the CALIOP Measurements Using the MODIS AOD as a Constraint, Remote Sens., 12, 251, doi:10.3390/rs12020251, 2020.

Kim, M.-H., Omar, A. H., Tackett, J. L., Vaughan, M. A., Winker, D. M., Trepte, C. R., Hu, Y., Liu, Z., Poole, L. R., Pitts, M. C., Kar, J., and Magill, B. E.: The CALIPSO version 4 automated aerosol classification and lidar ratio selection algorithm, Atmos. Meas. Tech., 11, 6107–6135, doi:10.5194/amt-11-6107-2018, 2018.

Kiriakidis, P., Gkikas, A., Papangelis, G., Christoudias, T., Kushta, J., Proestakis, E., Kampouri, A., Marinou, E., Drakaki, E., Benedetti, A., Rennie, M., Retscher, C., Straume, A. G., Dandocsi, A., Sciare, J., and Amiridis, V.: The impact of using assimilated Aeolus wind data on regional WRF-Chem dust simulations, Atmos. Chem. Phys., 23, 4391–4417, doi:10.5194/acp-23-4391-2023, 2023.

Kok, J. F., Ridley, D. A., Zhou, Q., Miller, R. L., Zhao, C., Heald, C. L., Ward, D. S., Albani, S., and Haustein, K.: Smaller desert dust cooling effect estimated from analysis of dust size and abundance, Nat. Geosci., 10, 274–278, doi:10.1038/ngeo2912, 2017.

Kok, J. F., Adebiyi, A. A., Albani, S., Balkanski, Y., Checa-Garcia, R., Chin, M., Colarco, P. R., Hamilton, D. S., Huang, Y., Ito, A., Klose, M., Li, L., Mahowald, N. M., Miller, R. L., Obiso, V., Pérez García-Pando, C., Rocha-Lima, A., and Wan, J. S.: Contribution of the world's main dust source regions to the global cycle of desert dust, Atmos. Chem. Phys., 21, 8169–8193, doi:10.5194/acp-21-8169-2021, 2021.

Kok, J. F., Storelvmo, T., Karydis, V. A., Adebiyi, A. A., Mahowald, N. M., Evan, A. T., He, C., and Leung, D. M.: Mineral dust aerosol impacts on global climate and climate change, Nat. Rev. Earth Environ., 4, 71–86, doi:10.1038/s43017022-00379-5, 2023.

Konsta, D., Binietoglou, I., Gkikas, A., Solomos, S., Marinou, E., Proestakis, E., Basart, S., Pérez García-Pando, C., El-Askary, H., and Amiridis, V.: Evaluation of the BSC-DREAM8b regional dust model using the 3D LIVAS-CALIPSO product, Atmos. Environ., 195, 46–62, doi:10.1016/j.atmosenv.2018.09.047, 2018.

Li, L. and Sokolik, I.: Analysis of Dust Aerosol Retrievals Using Satellite Data in Central Asia, Atmosphere, 9, 288, doi:10.3390/atmos9080288, 2018.

Li, L., Dubovik, O., Derimian, Y., Schuster, G. L., Lapyonok, T., Litvinov, P., Ducos, F., Fuertes, D., Chen, C., Li, Z., Lopatin, A., Torres, B., and Che, H.: Retrieval of aerosol components directly from satellite and ground-based measurements, Atmos. Chem. Phys., 19, 13409–13443, doi:10.5194/acp-19-13409-2019, 2019.

~~Li, Z., Painemal, D., Schuster, G., Clayton, M., Ferrare, R., Vaughan, M., Trepte, C., & Liu, Z.: Assessment of tropospheric CALIPSO Version 4.2 aerosol types over the ocean using independent CALIPSO SODA lidar ratios. *Atmospheric Measurement Techniques Discussions*, 2021, 1–38, doi:10.5194/amt-2021-163, 2021.~~

~~Li, Z., Painemal, D., Schuster, G., Clayton, M., Ferrare, R., Vaughan, M., Josset, D., Kar, J., and Trepte, C.: Assessment of tropospheric CALIPSO Version 4.2 aerosol types over the ocean using independent CALIPSO SODA lidar ratios, Atmos. Meas. Tech., 15, 2745–2766, doi:10.5194/amt-15-2745-2022, 2022.~~

Logothetis, S.-A., Salamalikis, V., Gkikas, A., Kazadzis, S., Amiridis, V., and Kazantzidis, A.: 15-year variability of desert dust optical depth on global and regional scales, Atmos. Chem. Phys., 21, 16499–16529, doi:10.5194/acp-21-16499-2021, 2021.

Luo, Y., Zheng, X., and Chen, J.: A climatology of aerosol optical depth over China from recent 10 years of MODIS remote sensing data, Int. J. Climatol., 34, 863–870, doi:10.1002/joc.3728, 2014.

Ma, X., Bartlett, K., Harmon, K., and Yu, F.: Comparison of AOD between CALIPSO and MODIS: significant differences over major dust and biomass burning regions, Atmos. Meas. Tech., 6, 2391–2401, doi:10.5194/amt-6-2391-2013, 2013.

Mahowald, N., Albani, S., Kok, J. F., Engelstaeder, S., Scanza, R., Ward, D. S., and Flanner, M. G.: The size distribution of desert dust aerosols and its impact on the Earth system, Aeolian Res., 15, 53–71, doi:-10.1016/j.aeolia.2013.09.002, 2014.

~~Mamouri, R. E. and Ansmann, A.: Fine and coarse dust separation with polarization lidar, Atmos. Meas. Tech., 7, 3717–3735, doi:10.5194/amt-7-3717-2014, 2014.~~

~~Mamouri, R. E. and Ansmann, A.: Potential of polarization/Raman lidar to separate fine dust, coarse dust, maritime, and anthropogenic aerosol profiles, Atmos. Meas. Tech., 10, 3403–3427, doi:10.5194/amt-10-3403-2017, 2017.~~

Mao, K. B., Ma, Y., Xia, L., Chen, W. Y., Shen, X. Y., He, T. J., and Xu, T. R.: Global aerosol change in the last decade: An analysis based on MODIS data, Atmos. Environ., 94, 680–686, doi:10.1016/j.atmosenv.2014.04.053, 2014.

Marinou, E., Amiridis, V., Binietoglou, I., Tsikerdekis, A., Solomos, S., Proestakis, E., Konsta, D., Papagiannopoulos, N., Tsekeri, A., Vlastou, G., Zanis, P., Balis, D., Wandinger, U., and Ansmann, A.: Three-dimensional evolution of Saharan dust transport towards Europe based on a 9-year EARLINET-optimized CALIPSO dataset, Atmos. Chem. Phys., 17, 5893–5919, doi:10.5194/acp-17-5893-2017, 2017.

Mashat, A. W. S., Alamoudi, A. O., Awad, A. M., and Assiri, M. E.: Seasonal variability and synoptic characteristics of dust cases over southwestern Saudi Arabia. Int. J. Climatol., 38, 105-124, doi:10.1002/joc.5164, 2018.

Masoom, A., Kosmopoulos, P., Bansal, A., Gkikas, A., Proestakis, E., Kazadzis, S., and Amiridis, V.: Forecasting dust impact on solar energy using remote sensing and modeling techniques, Sol. Energy, 228, 317–332, doi:10.1016/j.solener.2021.09.033, 2021.

Mbourou, G. N., Bertrand, J. J., and Nicholson, S. E.: The diurnal and seasonal cycles of wind-borne dust over Africa north of the Equator, J. Appl. Meteorol., 36, 868–882, doi:10.1175/1520-0450(1997)036<0868:TDASCO>2.0.CO;2, 1997.

McGill, M., Vaughan, M., Trepte, C., Hart, W., Hlavka, D., Winker, D., and Kuehn, R.: Airborne validation of spatial properties measured by the CALIPSO lidar, J. Geophys. Res., 112, D20201, doi:10.1029/2007JD008768, 2007.

Mishchenko, M. I. and Travis, L. D.: Satellite retrieval of aerosol properties over the ocean using polarization as well as intensity of reflected sunlight, J. Geophys. Res., 102(D14), 16989–17013, doi:10.1029/96JD02425, 1997a.

Mishchenko, M. I. and Travis, L. D.: Satellite retrieval of aerosol properties over the ocean using measurements of reflected sun light: Effect of instrumental errors and aerosol absorption, J. Geophys. Res., 102, 13543–13553, doi:10.1029/97JD01124, 1997b.

Moustaka, A., Korras-Carraca, M. B., Papachristopoulou, K., Stamatis, M., Fountoulakis, I., Kazadzis, S., Proestakis., E., Amiridis, V., Tourpali, K., Georgiou, T., Solomos, S., Spyrou, C., Zerefos, C., and Gkikas, A.: Assessing Lidar Ratio Impact

on CALIPSO Retrievals Utilized for the Estimation of Aerosol SW Radiative Effects across North Africa, the Middle East, and Europe. Remote Sens., 16, 1689, doi: 10.3390/rs16101689, 2024.

Moustaka, A., Korras-Carraca, M.B., Papachristopoulou, K., Fountoulakis, I., Kazadzis, S., Proestakis, E., Amiridis, V., Tourpali, K., Gkikas, A. Assessment of Cloud-Aerosol Lidar with Orthogonal Polarization–Cloud-Aerosol Lidar and Infrared Pathfinder Satellite Observations Retrievals towards Estimating the Aerosol Direct Impact on the Shortwave Radiation Budgets in North Africa, Europe, and the Middle East. Environ. Sci. Proc., 26, 139, doi: 10.3390/environsciproc2023026139, 2023.

Moustaka, A., ~~Siomos, N.,~~Siomos, N., Kazadzis, S., Proestakis, E., Voudouri, K. A., Lopatin, A., Dubovik, O., Tourpali, K., Zerefos, C., Amiridis, V., and Gkikas, A. (2025): Enhancing dust aerosols monitoring capabilities across North Africa and the Middle East using the A-Train satellite constellation [Data set], Zenodo, doi:10.5281/zenodo.18016524~~doi:10.5281/zenodo.18016524~~, 2025[AM2].

Müller, D., Ansmann, A., Mattis, I., Tesche, M., Wandinger, U., Althausen, D., and Pisani, G.: Aerosol-type-dependent lidar ratios observed with Raman lidar, J. Geophys. Res., 112, D16202, doi:10.1029/2006JD008292, 2007.

NASA Langley Research Center: CALIPSO quality statements: lidar level 1B profile products, Version 2.01, NASA, Hampton, VA, USA, 2007.

Ningombam, S., Larson, E. J. L., Dumka, U. C., Estellés, V., Campanelli, M., and Colwell, S.: Long-term (1995–2018) aerosol optical depth derived using ground based AERONET_and_SKYNET measurements from aerosol aged-background sites, Atmos. Pollut. Res., 10, 608–620, doi:10.1016/j.apr.2018.10.008, 2019.

~~Nisantzi, A., Mamouri, R. E., Ansmann, A., and Hadjimitsis, D.: Injection of mineral dust into the free troposphere during fire events observed with polarization lidar at Limassol, Cyprus, Atmos. Chem. Phys., 14, 12155–12165, doi:10.5194/acp-14-12155-2014, 2014.~~

Omar, A. H., Won, J.-G., Winker, D. M., Yoon, S.-C., Dubovik, O., and McCormick, M. P.: Development of global aerosol models using cluster analysis of Aerosol Robotic Network (AERONET) measurements, J. Geophys. Res., 110, D10S14, doi:10.1029/2004JD004874, 2005.

Omar, A. H., Winker, D. M., Vaughan, M. A., Hu, Y., Trepte, C. R., Ferrare, R. A., Lee, K. P., Hostetler, C. A., Kittaka, C., Rogers, R. R., and Kuehn, R. E.: The CALIPSO Automated Aerosol Classification and Lidar Ratio Selection Algorithm, J. Atmos. Ocean. Tech., 26, 1994–2014, doi:10.1175/2009JTECHA1231.1, 2009.

Omar, A. H., Winker, D. M., Tackett, J. L., Giles, D. M., Kar, J., Liu, Z., Vaughan, M. A., Powell, K. A., and Trepte, C. R.: CALIOP and AERONET aerosol optical depth comparisons: One size fits none, Journal of Geophysical Research: Atmospheres, 118(10), 4748–4766, doi:10.1002/jgrd.50330, 2013.

U.S. Committee on Extension to the Standard Atmosphere (COESA): *U.S. Standard Atmosphere, 1976*, U.S. Government Printing Office, Washington, D.C., 1976.

~~Panahifar, H., Bayat, F., and Hussein, T.: Simultaneous Use of Ground Based and Satellite Observation to Evaluate Atmospheric Air Pollution over Amman, Jordan. Atmosphere, 14, 274, doi: 10.3390/atmos14020274, 2023.~~

Papachristopoulou, K., Fountoulakis, I., Gkikas, A., Kosmopoulos, P. G., Nastos, P. T., Hatzaki, M., and Kazadzis, S.: 15-Year Analysis of Direct Effects of Total and Dust Aerosols in Solar Radiation/Energy over the Mediterranean Basin, Remote Sens.-Basel, 14, 1535, doi:10.3390/rs14071535, 2022.

Pease, P. P., Tchakerian, V. P., and Tindale, N. W.: Aerosols over the Arabian Sea: geochemistry and source areas for Aeolian desert dust, J. Arid Environ., 39, 477–496, doi:10.1006/jare.1997.0368, 1998.

~~Jish Prakash, P., Stenchikov, G., Kalenderski, S., Osipov, S., and Bangalath, H.: The impact of dust storms on the Arabian Peninsula and the Red Sea, Atmos. Chem. Phys., 15, 199–222, doi:10.5194/acp-15-199-2015, 2015.~~

Preißler, J., Wagner, F., Pereira, S. N., and Guerrero-Rascado, J. L.: Multi-instrumental observation of an exceptionally strong Saharan dust outbreak over Portugal, J. Geophys. Res.-Atmos., 116, D24204, doi:10.1029/2011JD016527, 2011.

Proestakis, E., Amiridis, V., Marinou, E., Georgoulias, A. K., Solomos, S., Kazadzis, S., Chimot, J., Che, H., Alexandri, G., Binietoglou, I., Daskalopoulou, V., Kourtidis, K. A., de Leeuw, G., and van der A, R. J.: Nine-year spatial and temporal evolution of desert dust aerosols over South and East Asia as revealed by CALIOP, Atmos. Chem. Phys., 18, 1337–1362, doi:10.5194/acp-18-1337-2018, 2018.

Prospero, J. M. and Mayol-Bracero, O. L.: Understanding the transport and impact of African dust on the Caribbean basin, B. Am. Meteorol. Soc., 94, 1329–1337, doi:10.1175/BAMS-D-12-00142.1, 2013.

~~Pu, B. and Ginoux, P.: How reliable are CMIP5 models in simulating dust optical depth?, Atmos. Chem. Phys., 18, 12491–12510, doi:10.5194/acp-18-12491-2018, 2018.~~

Raptis, I.-P., Kazadzis, S., Amiridis, V., Gkikas, A., Gerasopoulos, E., and Mihalopoulos, N.: A Decade of Aerosol Optical Properties Measurements over Athens, Greece, Atmosphere, 11, 154, doi:10.3390/atmos11020154, 2020.

Rezazadeh, M., Irannejad, P., and Shao, Y. J. A. R.: Climatology of the Middle East dust events. Aeolian Research, 10, 103–109, doi:10.1016/j.aeolia.2013.09.004, 2013.

Rittmeister, F., Ansmann, A., Engelmann, R., Skupin, A., Baars, H., Kanitz, T., and Kinne, S.: Profiling of Saharan dust from the Caribbean to western Africa – Part 1: Layering structures and optical properties from shipborne polarization/Raman lidar observations, Atmos. Chem. Phys., 17, 12963–12983, doi:10.5194/acp-17-12963-2017, 2017.

Roccetti, G., Bugliaro, L., Gödde, F., Emde, C., Hamann, U., Manev, M., Sterzik, M. F., and Wehrum, C.: HAMSTER: Hyperspectral Albedo Maps dataset with high Spatial and TEmporal Resolution, Atmos. Meas. Tech., 17, 6025–6046, doi:10.5194/amt-17-6025-2024, 2024.

Sayer, A. M., Hsu, N. C., Bettenhausen, C., and Jeong, M.-J.: Validation and uncertainty estimates for MODIS Collection 6 "Deep Blue" aerosol data, J. Geophys. Res. Atmos., 118, 7864–7872, doi:10.1002/jgrd.50600, 2013.

Sayer, A. M., Smirnov, A., Hsu, N. C., and Holben, B. N.: A pure marine aerosol model, for use in remote sensing applications, J. Geophys. Res., 117, D05213, doi:10.1029/2011JD016689, 2012.

Schepanski, K.: Transport of Mineral Dust and Its Impact on Climate, Geosciences, 8, 151, doi:10.3390/geosciences8050151, 2018.

Scheuvens, D., Schütz, L., Kandler, K., Ebert, M., and Weinbruch, S.: Bulk composition of northern African dust and its source sediments– A compilation, Earth-Sci. Rev., 116, 170194, doi:10.1016/j.earscirev.2012.08.005, 2013.

Schuster, G. L., Vaughan, M., MacDonnell, D., Su, W., Winker, D., Dubovik, O., Lapyonok, T., and Trepte, C.: Comparison of CALIPSO aerosol optical depth retrievals to AERONET measurements, and a climatology for the lidar ratio of dust, Atmos. Chem. Phys., 12, 7431–7452, doi:10.5194/acp-12-7431-2012, 2012.

Schuster, G. L., Dubovik, O., and Arola, A.: Remote sensing of soot carbon – Part 1: Distinguishing different absorbing aerosol species, Atmos. Chem. Phys., 16, 1565–1585, doi:10.5194/acp-16-1565-2016, 2016.

~~Shen, H., Abuduwaili, J., Samat, A., and Ma, L.: A review on the research of modern aeolian dust in Central Asia, Arab J. Geosci., 9, 625, doi:10.1007/s12517-016-2646-9, 2016.~~

Shi, Y., Zhang, J., Reid, J. S., Holben, B., Hyer, E. J., and Curtis, C.: An analysis of the collection 5 MODIS over-ocean aerosol optical depth product for its implication in aerosol assimilation, Atmos. Chem. Phys., 11, 557–565, doi:10.5194/acp-11-557-2011, 2011.

Sinyuk, A., Holben, B. N., Eck, T. F., Giles, D. M., Slutsker, I., Korkin, S., Schafer, J. S., Smirnov, A., Sorokin, M., and Lyapustin, A.: The AERONET Version 3 aerosol retrieval algorithm, associated uncertainties and comparisons to Version 2, Atmos. Meas. Tech., 13, 3375–3411, doi:10.5194/amt-13-3375-2020, 2020.

Solmon, F., Nair, V. S., and Mallet, M.: Increasing Arabian dust activity and the Indian summer monsoon, Atmos. Chem. Phys., 15, 8051–8064, doi:10.5194/acp-15-8051-2015, 2015.

~~Song, Q., Zhang, Z., Yu, H., Ginoux, P., and Shen, J.: Global dust optical depth climatology derived from CALIOP and MODIS aerosol retrievals on decadal timescales: regional and interannual variability, Atmos. Chem. Phys., 21, 13369–13395, doi:10.5194/acp-21-13369-2021, 2021.~~

Steinmetz, F., Ramon, D., Deschamps, P. Y., and Nicolas, J. M.: Analysis of the first ocean color products from POLDER 3 onboard PARASOL. In Remote Sensing of the Ocean, Sea Ice, and Large Water Regions 2005, 5977, 209-217, doi:10.1117/12.629878, 2005.

Szczepanik, D. M., Stachlewska, I. S., Tetoni, E., and Althausen, D.: Properties of Saharan Dust Versus Local Urban Dust—A Case Study, Earth and Space Sc., 8, e2021EA001816, doi:10.1029/2021EA001816, 2021.

Tackett, J. L., Winker, D. M., Getzewich, B. J., Vaughan, M. A., Young, S. A., and Kar, J.: CALIPSO lidar level 3 aerosol profile product: version 3 algorithm design, Atmos. Meas. Tech., 11, 4129–4152, doi:10.5194/amt-11-4129-2018, 2018.

Tackett, J. L., Kar, J., Vaughan, M. A., Getzewich, B. J., Kim, M.-H., Vernier, J.-P., Omar, A. H., Magill, B. E., Pitts, M. C., and Winker, D. M.: The CALIPSO version 4.5 stratospheric aerosol subtyping algorithm, Atmos. Meas. Tech., 16, 745–768, doi:10.5194/amt-16-745-2023, 2023.

Tesche, M., Ansmann, A., Müller, D., Althausen, D., Mattis, I., Heese, B., Freudenthaler, V., Wiegner, M., Esselborn, M., Pisani, G., and Knippertz, P.: Vertical profiling of Saharan dust with Raman lidars and airborne HSRL in southern Morocco during SAMUM, Tellus B, 61, 144–164, doi:10.1111/j.16000889.2008.00390.x, 2009~~a~~.

Tesche, M., Ansmann, A., Müller, D., Althausen, D., Engelmann, R., Freudenthaler, V., and Groß, S.: Vertically resolved separation of dust and smoke over Cape Verde using multiwavelength Raman and polarization lidars during Saharan Mineral Dust Experiment 2008, J. Geophys. Res., 114, D13202, doi:10.1029/2009JD011862, 2009b.

Tesche, M., Groß, S., Ansmann, A., Müller, D., Althausen, D., Freudenthaler, V., and Esselborn, M.: Profiling of Saharan dust and biomass-burning smoke with multiwavelength polarization Raman lidar at Cape Verde, Tellus B, 63, 16360, doi:10.3402/tellusb.v63i4.16360, 2011.

Textor, C., Schulz, M., Guibert, S., Kinne, S., Balkanski, Y., Bauer, S., Berntsen, T., Berglen, T., Boucher, O., Chin, M., Dentener, F., Diehl, T., Easter, R., Feichter, H., Fillmore, D., Ghan, S., Ginoux, P., Gong, S., Grini, A., Hendricks, J., Horowitz, L., Huang, P., Isaksen, I., Iversen, I., Kloster, S., Koch, D., Kirkevåg, A., Krist jansson, J. E., Krol, M., Lauer, A., Lamarque, J. F., Liu, X., Mon tanaro, V., Myhre, G., Penner, J., Pitari, G., Reddy, S., Seland, Ø., Stier, P., Takemura, T., and Tie, X.: Analysis and quantification of the diversities of aerosol life cycles within AeroCom, Atmos. Chem. Phys., 6, 1777–1813, doi:10.5194/acp-6-1777--2006, 2006.

Tindan, J. Z., Jin, Q., and Pu, B.: Understanding day–night differences in dust aerosols over the dust belt of North Africa, the Middle East, and Asia, Atmos. Chem. Phys., 23, 5435–5466, doi:10.5194/acp-23-5435-2023, 2023.

Urbanneck, C.: Retrieval of aerosol optical and microphysical properties in Cyprus during A-LIFE and CyCARE by lidar and closure studies with airborne insitu measurements– Towards aerosol-cloud interaction investigations, MSc thesis, Leipzig University, https://www.tropos.de/fileadmin/user_upload/Institut/Abteilungen/Fernerkundung/Daten_PDF/MA_claudia_urbanneck.pdf, (last access: 25 November 2024), 2018.

Wackerly, D. D., Mendenhall, W., and Scheaffer, R. L.: Mathematical statistics with applications (Vol. 7). Belmont, Thomson Brooks/Cole, Cengage, Belmont, CA, Australia, 2008.

Wagner, F. and Silva, A. M.: Some considerations about Ångström exponent distributions, Atmos. Chem. Phys., 8, 481–489, doi:10.5194/acp-8-481-2008, 2008.

Wandinger, U., Ansmann, A., Reichardt, J., and Deshler, T.: Determination of stratospheric aerosol microphysical properties from independent extinction and backscattering measurements with a Raman lidar, Appl. Optics, 34, 8315, doi:10.1364/AO.34.008315, 1995.

Wandinger, U., Floutsi, A. A., Baars, H., Haarig, M., Ansmann, A., Hünerbein, A., Docter, N., Donovan, D., van Zadelhoff, G.-J., Mason, S., and Cole, J.: HETEAC – the Hybrid End-To-End Aerosol Classification model for EarthCARE, Atmos. Meas. Tech., 16, 2485–2510, doi:10.5194/amt-16-2485-2023, 2023.

Wandinger U., Hiebsch, A., Mattis, I., Pappalardo, G., Mona, L., and Madonna, F.: Aerosols and Clouds: Long-term Database from Spaceborne Lidar Measurements, Executive Summary, available at: http://esamultimedia.esa.int/docs/gsp/C21487ExS.pdf (last access: 10 November 2024), ESTEC Contract 21487/08/NL/HE, 2011.

Wang, S. S., Yu, Y., Zhang, X. X., Lu, H. Y., Zhang, X. Y., and Xu, Z. W.: Weakened dust activity over China and Mongolia from 2001 to 2020 associated with climate change and land use management, Environ. Res. Lett., 16, 12, doi:10.1088/1748-9326/ac3b79, 2021.

Warren, A., Chappell, A., Todd, M. C., Bristow, C., Drake, N., Engelstaedter, S., Martins, V., M'Bainayel, S., and Washington, R.: Dust-raising in the dustiest place on earth, Geomorphology, 92, 25–37, doi:-10.1016/j.geomorph.2007.02.007, 2007.

Washington, R., Bouet, C., Cautenet, G., Mackenzie, E., Ashpole, I., Engelstaedter, S., Lizcano, G., Henderson, G. M., Schepanski, K., and Tegen, I.: Dust as a tipping element: The Bodele Depression, Chad, P. Natl. Acad. Sci. USA, 106, 20564–20571, doi:10.1073/pnas.0711850106, 2009.

Wehr, T., Kubota, T., Tzeremes, G., Wallace, K., Nakatsuka, H., Ohno, Y., Koopman, R., Rusli, S., Kikuchi, M., Eisinger, M., Tanaka, T., Taga, M., Deghaye, P., Tomita, E., and Bernaerts, D.: The EarthCARE mission – science and system overview, Atmos. Meas. Tech., 16, 3581–3608, doi:10.5194/amt-16-3581-2023, 2023.

Weinan, C., Fryrear, D. W., and Zuotao, Y.: Dust fall in the Takla Makan desert of China. Phys. Geogr., 20, 189-224, 1999.

Weinzierl, B., Ansmann, A., Prospero, J., Althausen, D., Benker, N., Chouza, F., Dollner, M., Farrell, D., Fomba, W., Freudenthaler, V., Gasteiger, J., Groß, S., Haarig, M., Heinold, B., Kandler, K., Kristensen, T., Mayol-Bracero, O., Müller, T., Reitebuch, O., Sauer, D., Schäfler, A., Schepanski, K., Spanu, A., Tegen, I., Toledano, C., and Walser, A.: The Saharan Aerosol Long-range Transport and Aerosol-Cloud Interaction Experiment (SALTRACE): overview and selected highlights, B. Am. Meteorol. Soc., 98, 1427–1451, doi:-10.1175/BAMS-D-15-00142.1, 2017.

Winker, D. M., Vaughan, M. A., Omar, A., Hu, Y., Powell, K. A., Liu, Z., Hunt, W. H., and Young, S. A.: Overview of the CALIPSO mission and CALIOP data processing algorithms, J. Atmos. Ocean. Tech., 26, 2310–2323, doi:10.1175/2009JTECHA1281.1, 2009.

Winker, D. M., Pelon, J., Coakley Jr, J. A., Ackerman, S. A., Charlson, R. J., Colarco, P. R., Flamant, P., Fu, Q., Hoff, R. M., Kittaka, C., Kubar, T. L., Le Treut, H., McCormick, M. P., Mégie, G., Poole, L., Powell, K., Trepte, C., Vaughan, M. A., and Wielicki, B. A.: The CALIPSO mission: A global 3D view of aerosols and clouds, Bull. Amer. Meteor. Soc., 91, 1211–1229, doi:10.1175/2010BAMS3009.1, 2010.

Winker, D. M., Tackett, J. L., Getzewich, B. J., Liu, Z., Vaughan, M. A., and Rogers, R. R.: The global 3-D distribution of tropospheric aerosols as characterized by CALIOP, Atmospheric Chemistry and Physics, 13(6), 3345–3361, doi:10.5194/acp-13-3345-2013, 2013.

Wang, Z., Shi, C., Zhang, H., Chen, Y., Chi, X., Xia, C., Wang, S., Zhu, Y., Zhang, K., Chen, X., Xing, C., and Liu, C.: Measurement report: Dust and anthropogenic aerosols' vertical distributions over northern China dense aerosols gathered at the top of the mixing layer, Atmos. Chem. Phys., 23, 14271–14292, doi:10.5194/acp-23-14271-2023, 2023.

Xiao, D., Wang, N., Chen, S., Wu, L., Müller, D., Veselovskii, I., Li, C., Landulfo, E., Sivakumar, V., Li, J., and Fix, A.: Simultaneous profiling of dust aerosol mass concentration and optical properties with polarized high-spectral-resolution lidar. Science of The Total Environment, 872, 162091, doi:10.1016/j.scitotenv.2023.162091, 2023.

Xiong, J., Zhao, T., Bai, Y., Liu, Y., Han, Y., and Guo, C.: Climate characteristics of dust aerosol and its transport in major global dust source regions. Journal of Atmospheric and Solar-Terrestrial Physics, 209, 105415, doi: 10.1016/j.jastp.2020.105415, 2020.

Yu, Y., Notaro, M., Liu, Z., Kalashnikova, O., Alkolibi, F., Fadda, E., and Bakhrjy, F.: Assessing temporal and spatial variations in atmospheric dust over Saudi Arabia through satellite, radiometric, and station data, J. Geophys. Res.-Atmos., 118, 13-253~~1325313264~~, doi:10.1002/2013JD020677, 2013.

Yu, Y., Notaro, M., Liu, Z., Wang, F., Alkolibi, F., Fadda, E., and Bakhrjy, F.: Climatic controls on the interannual to decadal variability in Saudi Arabian dust activity: toward the development of a seasonal dust prediction model, J. Geophys. Res.-Atmos., 120, 1739–1758, doi:10.1002/2014JD022611, 2015.

Yu, X., Nichol, J., Lee, K.H., Li, J., and Wong, M.S.: Analysis of long-term aerosol optical properties combining AERONET sunphotometer and satellite-based observations in Hong Kong. Remote Sens., 14, 5220, doi:10.3390/rs14205220, 2022.

Zender, C. S., Miller, R. L. R. L., and Tegen, I.: Quantifying mineral dust mass budgets: Terminology, constraints, and current estimates, Eos, Trans. Am. Geophys. Union, 85(48), 509–512, doi:10.1029/2004EO480002, 2004.

~~Zender, C. S., Miller, R. L., and Tegen, I.: Quantifying mineral dust mass budgets: Systematic terminology, constraints, and current estimates, in EOS, 509–512, 2004.~~

Zhang, J. and Reid, J. S.: MODIS aerosol product analysis for data assimilation: Assessment of over-ocean level 2 aerosol optical thickness retrievals, J. Geophys. Res.-Atmos., 111, D22207, doi:10.1029/2005JD006898, 2006.

Zhang, T., Zheng, M., Sun, X., Chen, H., Wang, Y., Fan, X., Pan, Y., Quan, J., Liu, J., Wang, Y., Lyu, D., Chen, S., Zhu, T., and Chai, F.: Environmental impacts of three Asian dust events in the northern China and the northwestern Pacific in spring 2021, Sci. Total Environ., 859, 160230, doi:10.1016/j.scitotenv.2022.160230, 2023.

Zhang, X., Li, L., Chen, C., Chen, X., Dubovik, O., Derimian, Y., Gui, K., Zheng, Y., Zhao, H., Zhang, L., Guo, B., Wang, Y., Holben, B., Che, H., and Zhang, X.: Validation of the aerosol optical property products derived by the GRASP/Component approach from multi-angular polarimetric observations, Atmos. Res., 263, 105802, doi:10.1016/j.atmosres.2021.105802, 2021.

Zhang, X., Li, L., Chen, C., Zheng, Y., Dubovik, O., Derimian, Y., Lopatin, A., Gui, K., Wang, Y., Zhao, H., Liang, Y., Holben, B., Che, H., and Zhang, X.: Extensive characterization of aerosol optical properties and chemical component concentrations: Application of the GRASP/Component approach to long-term AERONET measurements, Sci. Total Environ., 812, 152553, doi:10.1016/j.scitotenv.2021.152553, 2022.

~~Zhang, Y. and Cheng, J.: Spatio-temporal analysis of urban heat island using multisource remote sensing data: A case study in Hangzhou, China. IEEE J. Sel. Top. Appl. Earth Obs. Remote, 12, 3317-3326, doi: https://doi.org/10.1109/JSTARS.2019.2926417 , 2019.~~